A New Instrument and Method for Nitrogen-loss Studies in Oxygen Deficient Zones

Andrew Reed

A dissertation

submitted in partial fulfillment of the

requirements for the degree of

Doctor of Philosophy

University of Washington

2018

Reading Committee:

Craig McNeil, Chair

Eric D'Asaro

Mark Altabet

Program Authorized to Offer Degree:

School of Oceanography

University of Washington

Abstract

A New Instrument and Method for Nitrogen-loss Studies in Oxygen Deficient Zones

Andrew Reed

Chair of the Supervisory Committee:
Dr. Craig McNeil
Air-Sea Interaction and Remote Sensing, Applied Physics Lab & School of Oceanography

The ocean's biogeochemical cycles are coming under increasing stress due to global climate change and anthropogenic emissions of carbon dioxide. Three different factors are stressing the oceans: rising temperatures, acidification, and deoxygenation [Gruber 2011]. Rising temperatures are predicted to increase stratification and slow-down global ocean circulation. We examine the change in the rates of formation and characteristics of Antarctic Bottom Water (AABW) in the Australia-Antarctic Basin from repeat hydrographic sections. Using changes in CFC-11 and CFC-12 concentrations, we find that AABW formation rates corrected for seasonality decrease by approximately 20%, from 0.38 ± 0.04 m^2 s^{-1} in 1991 to 0.30 ± 0.02 m^2 s^{-1} in 2008. Additionally, we find the sampled AABW warmed and increased in salinity, likely due to the increasing influence of bottom water formed in the Ross Sea over fresh, cold waters formed offshore of Adelie Land. Oceanic deoxygenation has the potential to significantly alter the global nitrogen cycle due to potential expansion of Oxygen Deficient Zones (ODZs), which are regions of the pelagic ocean where oxygen concentrations are nearly or functionally zero. In ODZs, microbes utilize biologically-available fixed nitrogen to either respire organic matter (denitrification) or fix new

organic matter (anammox), converting the fixed nitrogen into N_2-gas. An alternative method to the traditional method of measuring dissolved N_2-gas by N_2:Ar mass spectrometry is using in-situ measurements of total dissolved gas pressure (gas tension) using a gas tension device (GTD). We designed and characterized a new GTD which uses a custom designed small diameter (4 cm) thin (130 µm) incompressible composite Teflon-AF 2400 membrane. The new GTD eliminates issues of hydrostatic pressure-generated transients, changes to response times, and reverse osmosis, which plagued existing versions of GTDs using a compressible polydimethylsiloxane (PDMS) membrane. We demonstrate that two of the new GTDs, attached to different gas-sensing floats, measure the in-situ gas tension of the Eastern Tropical North Pacific (ETNP) ODZ with accuracies of 0.6% and 0.4% compared to gas-tension calculated from independent measurements of N_2:Ar by mass spectrometry and O_2 by Winkler titration. Next, we present a new method for calculating the biogenic-N_2 from gas tension. N_2 is derived by subtracting the O_2, Ar, climatological CO_2, and water vapor pressure from the gas tension. Argon is estimated by developing a linear-mixing-model based on T-S analysis to interpolate an independent argon concentration data set in the ODZ to our observations. This model is also applied to estimate the abiotic-N_2 concentrations to account for supersaturations due to mixing and warming. Peak biogenic-N_2 concentrations are 11.33 ± 1.75 µM/kg (F77) and 6.40 ± 2.07 µM/kg (F78), along with an independent estimate of 6.55 ± 2.05 µM/kg N_2 calculated from concurrently-sampled N_2:Ar ratios and 5.26 ± 1.22 µM/kg from nutrients along the σ_θ = 26.2 kg/m^{-3} isopycnal, which corresponds with the core volume of the ODZ. Lastly, we present a high-precision determination of the hydrostatic-pressure effect on the partial pressures of nitrogen, oxygen, and argon dissolved in freshwater by direct measurement with a GTD and an oxygen optode. Thermodynamics predict that partial pressure increases of 14% 1000 dbar^{-1} for N_2 and O_2 with molar volumes of 31 ± 2 mL/mol N_2 and 32 ± 2 mL/mol. Hydrostatic pressures ranged from 0 to 550 dbar, pressures typical in the intermediate to upper ocean. Our experiment directly measures the change in partial pressures for a commensurate change in hydrostatic pressure. We found a change of 12.99 ± 0.14% 1000 dbar^{-1} for O_2 and 15.53 ± 0.12% 1000 dbar^{-1} for N_2 with calculated molar volumes of 29.87 ± 0.35 mL/mol for O_2 and 35.12 ± 0.27 mL/mol for N_2. The results of our work is a new instrument and method which can be used for long-term autonomous biogeochemical monitoring of changes in the temporal and spatial variability of nitrogen-loss in ODZs.

TABLE OF CONTENTS

LIST OF FIGURES

LIST OF TABLES

ACKNOWLEDGEMENTS

I would like to acknowledge my mother Jan, brother Tim, and sister-in-law Ashlie, for all the love and support they have provided me during my graduate studies. I would also like to thank my two advisors, Mark Warner (Masters) and Craig McNeil (Ph.D.) for their patience and guidance.

DEDICATION

For my dad, Harry.

Chapter 1. DECREASING ANTARCTIC BOTTOM WATER PRODUCTION IN THE AUSTRALIA-ANTARCTIC BASIN

Andrew Reed[1], Mark Warner[1], Rolf Sonnerup[2], John Bullister[3]

[1]School of Oceanography, University of Washington, Seattle, Washington, USA.
[2]Joint Institute for the Study of Atmospheres and Oceans, University of Washington, Seattle, Washington, USA.
[3]Pacific Marine Environmental Laboratory, NOAA, Seattle, Washington, USA.

1.1. INTRODUCTION

The Southern Ocean is a dominant source of abyssal waters to the world ocean. Abyssal waters are produced in a few locations on the Antarctic margins where buoyancy loss, driven by cooling from the atmosphere, ocean-ice shelf interactions, and brine rejection during sea-ice formation, is sufficient to generate dense shelf waters. The dense shelf waters flows off of the shelf through bathymetric troughs and channels in the Antarctic shelf break and down the continental slope, entraining warmer, saltier Circumpolar Deep Water in the process to produce Antarctic Bottom Water (AABW) [e.g. *Orsi et al.*, 1999].

The formation of AABW occurs in three principal locations around Antarctica, the Weddell Sea, the Ross Sea, and off the coast of Adèlie/George V Land (ALGV) [*Jacobs et al.*, 1970; *Gill*, 1973]. Each of these produce bottom waters with distinct properties. The bottom waters of the Australia-Antarctic Basin (AAB), located offshore of ALGV between 90°E and 150°E, are ventilated by a combination of bottom waters from the Ross Sea and AGVL [*Bindoff et al.*, 2000; *Whitworth*, 2002]. A portion of the comparatively salty and warm Ross Sea Bottom Water (RSBW) flows westward from the Ross Sea. Colder and fresher Adèlie Land Bottom Water (ALBW) flows downslope from its source in the Adèlie and Mertz Depressions, entering the AAB between 142°E and 145°E [*Williams and Bindoff* , 2003; *Williams et al.*, 2008]. The input of ALBW into the AAB is seasonal, with the strongest downslope flows observed during the months

of August through November, when the density of the shelf waters exceeds a neutral density (γ^n) threshold of 28.35 kg m^{-3} necessary for the shelf waters to reach the bottom of the basin without completely mixing away [*Fukamachi et al.*, 2000; *Williams et al.*, 2010].

Recent observations of the Southern Ocean heat budget from 1993 to 2008 indicate a heat uptake of 0.10 W m^{-2} for AABW, with statistically significant warming apparent in all basins that are directly ventilated by AABW [*Purkey and Johnson*, 2010]. This warming corresponds to a loss of 8.2 (±2.6) Sv of water below the 0°C isotherm [*Purkey and Johnson*, 2012]. The contraction could be due to changes in the type of bottom water produced in the Southern Ocean, the rate of formation, or increased AABW loss to mixing. Also, significant freshening (0.003 yr^{-1}) has been observed in RSBW present at 150°E since the 1950s [*Jacobs et al.*, 2002; *Jacobs*, 2006]. A freshening signal of 0.03 at neutral densities greater than 28.35 kg m^{-3} was also observed in the AAB at 140°E between 1994 and 2003 [*Aoki et al.*, 2005] . The freshening and warming in the AAB has been attributed both to changes in the ALBW and a reduction in the input and change in properties of the RSBW component [*Aoki et al.*, 2005; *Rivaro et al.*, 2010; *Shimada et al.*, 2012].

Chlorofluorocarbons (CFCs) are anthropogenic compounds with a well-resolved, time-dependent atmospheric source that are widely used as tracers to infer rates of deep water production in the global ocean [e.g. *Orsi et al.*, 1999; *Smethie Jr. and Fine*, 2001]. Waters at the surface acquire CFCs from the atmosphere, which are then conveyed conservatively into the ocean interior. The resultant accumulation of CFCs, or CFC inventory, observed in deep and interior water masses can be related to their formation and subsequent transport from the surface [e.g. *Fine*, 2011]. CFC inventories in the deep and bottom waters of the Southern Ocean derived from early to mid-1990s WOCE hydrographic sections indicated a multi-decadal average AABW production rate of 8-12 Sv [*Orsi et al.*, 1999, 2002]. Approximately 60% of this AABW originates in the Weddell Sea, with the remainder formed within the Indo-Pacific, which includes ALBW and RSBW.

In this study, we focus on formation rates of AABW in the AAB using CFC measurements along four occupations of the SR3 hydrographic section between Tasmania and Antarctica in the AAB from the early 1990s through late 2000s. The changes in CFC inventories are used to estimate the AABW formation rate changes. Biases due to seasonality are accounted for using Θ-S observations. Additional possible biases due to mixing loss of AABW are evaluated using a 2-D advection-diffusion model. We find a change of 20% in the formation rate of AABW in the AAB

between 1991 and 2008 along with a concurrent change in the Θ-S properties. The changes are likely related to the warming observed by *Purkey and Johnson* [2012].

1.2. METHODS

1.2.1. Data

CFC-11 and CFC-12 concentrations (pmol kg^{-1}) and hydrographic data were collected along the SR3 WOCE/CLIVAR hydrographic section in the Southern Ocean on four occasions in 1991, 1995, 2001, and 2008 (Table 1.1). SR3 extends meridionally from Tasmania (44°S) to the Antarctic Shelf (66°S), and between 139°E and 146°E (Figure 1.1). We also used the S4P Antarctic slope section at 170°W and the meridional sections at 140°E and 150°E occupied as part of the Marginex and A0803 cruises. Finally, we also analyze the I09 meridional section along 115°E. The hydrographic data is publicly available online from the CLIVAR and Carbon Hydrographic Data Office (CCHDO). The available data is filtered by its WOCE and CLIVAR designated quality flags to retain only the highest-quality observations.

Table 1.1. Cruise information for the CFC and hydrographic data, available from the CLIVAR and Carbon Hydrographic Data Office (CCHDO).

Cruise	Ship	Year	Month	CFC PI
SR3	*Aurora Australis*	1991	Oct.	Bullister
SR3	*Aurora Australis*	1993	Mar.	
SR3	*Aurora Australis*	1994	Jan. – Mar.	
SR3	*Aurora Australis*	1995	Jan. – Feb.	Bullister
SR3	*Aurora Australis*	1996	Aug. – Sept.	
SR3	*Aurora Australis*	2001	Oct. – Dec.	Warner/Bullister
SR3	*Aurora Australis*	2008	Mar. – Apr.	Warner/Bullister
S4P	*Akademik Ioffe*	1992	Feb. – Apr.	Bullister/Warner
S4P	*Nathaniel B. Palmer*	2011	Feb. – Apr.	Smethie
Marginex	*Aurora Australis*	1996	Feb. – Mar.	Warner
A0803	*Aurora Australis*	2008	Dec. – Jan.	Warner/Bullister

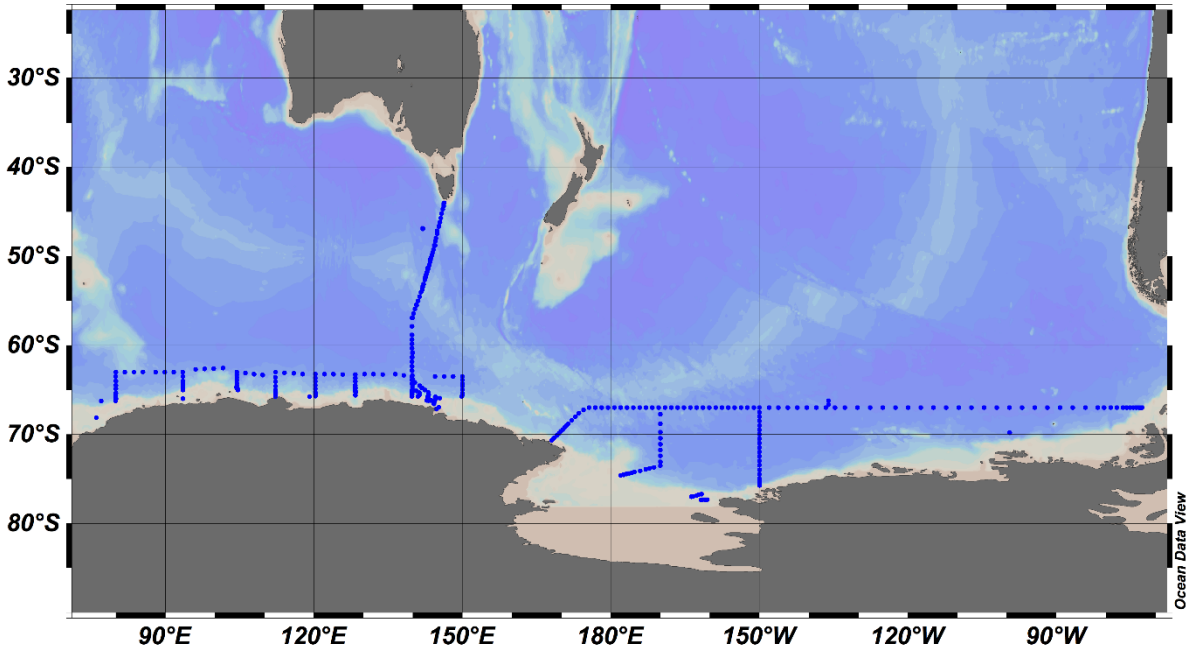

Figure 1.1. Map with the location of all hydrographic cruises with hydrographic or CFC data analyzed.

1.2.2. AABW CFC Inventories

The CFC concentrations (pmol kg^{-1}) and neutral densities from the bottle measurements were objectively interpolated to an uniform 1/10° latitude by 20 dbar depth grid following *Roemmich* [1983]. The bathymetry is taken from the 1'etopo bathymetric dataset [*Amante and Eakins*, 2009]. Total AABW CFC inventories for the AABW are calculated from the gridded CFC concentration fields (e.g. Figure 1.2). The definition of AABW is taken from *Orsi et al.* [1999] as waters exported below the 2500 m isobaths with a neutral density greater than 28.27 kg m^{-3}. Total CFC inventories (pmol m^{-1}) are calculated in two dimensions (latitude vs. depth).

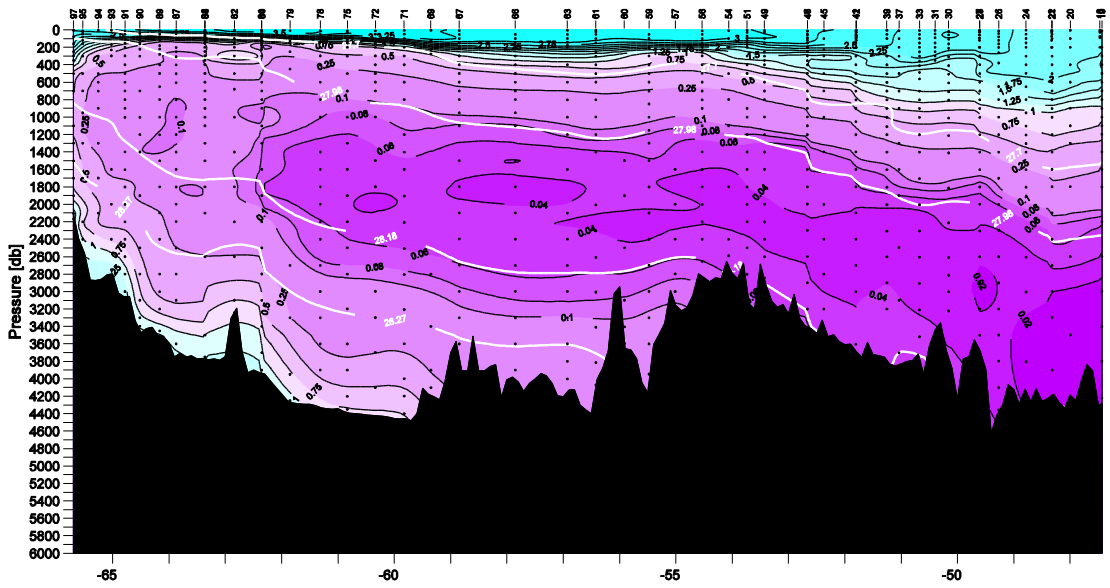

Figure 1.2. Example figure showing the SR3 2001 objectively interpolated CFC-12 concentrations and neutral densities (white lines). Similar maps of CFC-11 and CFC-12 concentrations are produced for each SR3 occupation along with the Marginex (1996)/A0803 (2008) meridional sections at 150°E and 140°E. The interpolated CFC concentrations are used to calculate the AABW CFC inventories.

1.2.3. Formation Rates

The AABW formation rate is calculated from the AABW CFC inventory for each SR3 occupation with the following equation:

$$I = R * Sat * F_{sol} * \rho_{sw} * \int CFC_{atmos}\,\mathrm{d}t - L \qquad (1.1)$$

where I is the AABW CFC inventory, R is the water mass formation rate ($m^2\ s^{-1}$), Sat is the saturation of the bottom waters with respect to the atmospheric CFCs, ρ_{sw} is the density of seawater, F_{sol} is the solubility, $CFC_{atmos}dt$ is the time integral of the CFC atmospheric source function, and L is loss of CFC from AABW [e.g. *Orsi et al.*, 1999]. The formation rate R is assumed to be constant and represents the long-term average since the beginning of the CFC time history, and is thus weighted by the higher CFC atmospheric concentrations since the 1970s. It is usually assumed there is no loss of CFCs from the AABW (L = 0). The validity of this assumption is tested with a 2-D advection-diffusion model below. The atmospheric CFC source function is integrated in

monthly time steps from the start of the record to the cruise date [*Bullister*, 2011]. The CFC-11 (CFC-12) saturations are 34.5% ± 4.1% in the coldest, densest AABW waters. The CFC saturation of AABW is set at 35% for consistency with and comparison to *Orsi et al.* [1999]. This low value results from entrainment of nearly-CFC free LCDW with sinking shelf waters. The saturation state is assumed to be constant. CFC concentrations of newly formed AABW are computed from the atmospheric CFC concentration history and the CFC solubilities [*Bullister*, 2011; *Warner and Weiss*, 1985]. We calculate R in two dimensions (latitude and depth) with resulting units of $m^2 s^{-1}$.

1.3. SR3 AABW OBSERVATIONS

1.3.1. AABW CFC Inventories

From 1991 to 1995, there is a small (4.2% CFC-11; 4.7% CFC-12) increase in the AABW CFC inventories (Figure 1.3) associated with a small decrease (3.8%) in the total cross-sectional area (Figure 1.4). The 2001 occupation shows significant increases in CFC inventories (76% CFC-11; 84.5% CFC-12) and cross-sectional area (9.3%) relative to 1995, followed by a decrease in the CFC inventories (12.5% CFC-11; 11.6% CFC-12) from 2001 to 2008. The CFC inventory loss is accompanied by a comparable 15.5% loss of AABW cross-sectional area.

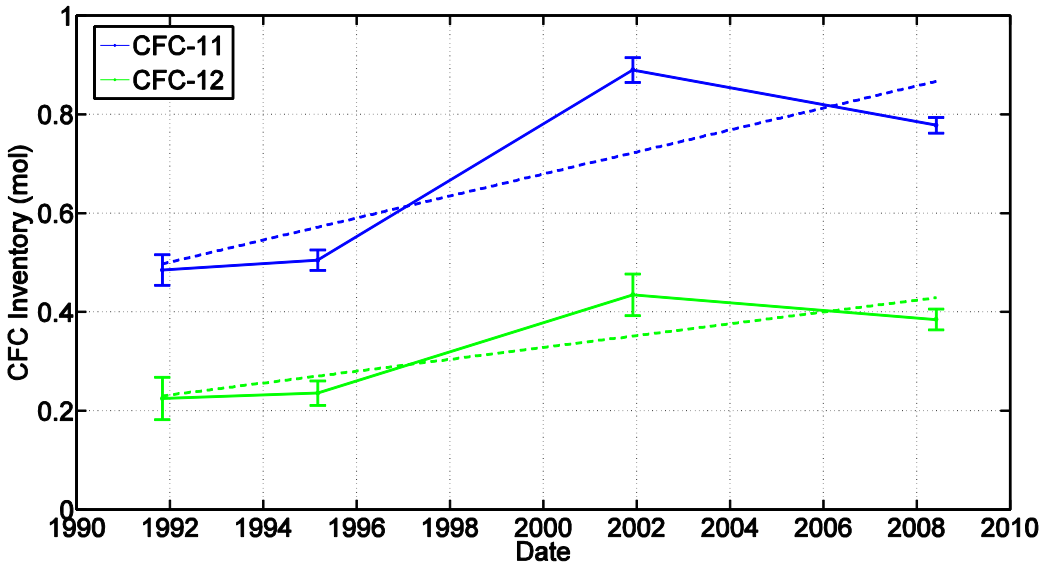

Figure 1.3. AABW total CFC-11 (blue) and CFC-12 (green) inventories (mol) along SR3 for each occupation, with associated error. Following Orsi et al. (1999), AABW is defined as those water below both the 28.27 kg m^{-3} neutral density isopycnal and the 2500 m isobath.

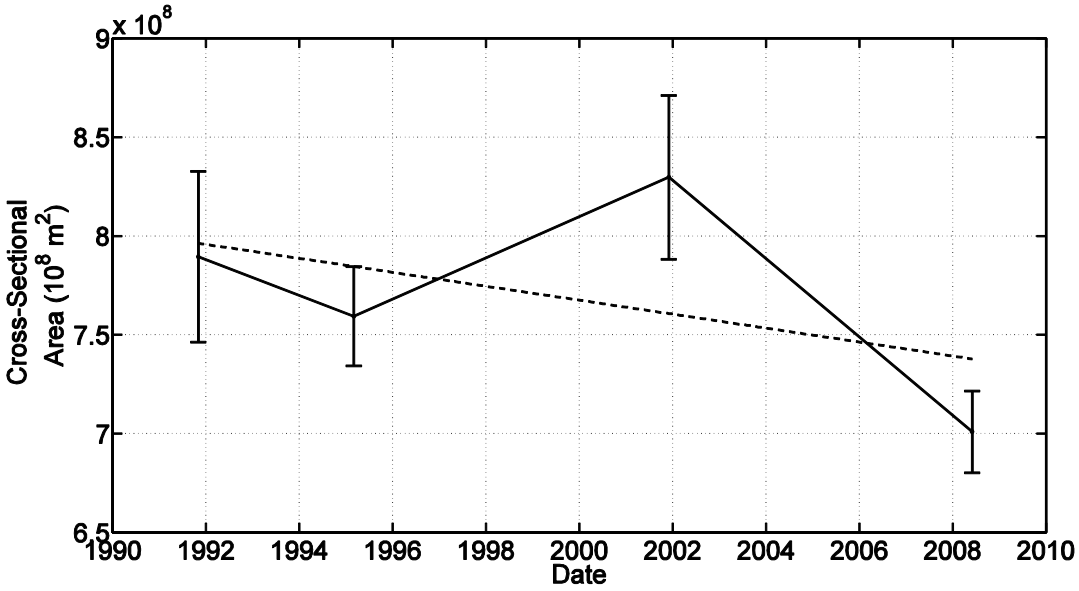

Figure 1.4. Total cross-sectional area (m^2) of AABW for each SR3 occupation, with associated error. Following Orsi et al. (1999), AABW is defined as those waters below the 28.27 kg m^{-3} neutral density isopycnal and 2500 m isobath.

1.3.2. Hydrographic Observations

Along isopycnals, Θ and S are cooler and fresher through time, especially between 1995 and 2001 (Figure 1.5). In 2001, the densest waters have Θ as cold as -0.8°C and S near 34.62 (γ^n > 28.36 kg m^{-3}). Waters with similar Θ and γ^n, but higher S, are observed in 1991. The densest bottom waters in 1995 and 2008 are warmer and less dense, reaching only -0.65°C and -0.60°C (γ^n = 28.355 kg m^{-3}). Similar to the 1991 and 2001 values, the densest bottom water in 1995 is more saline (S = 34.655) than the densest bottom water in 2008 (S = 34.645).

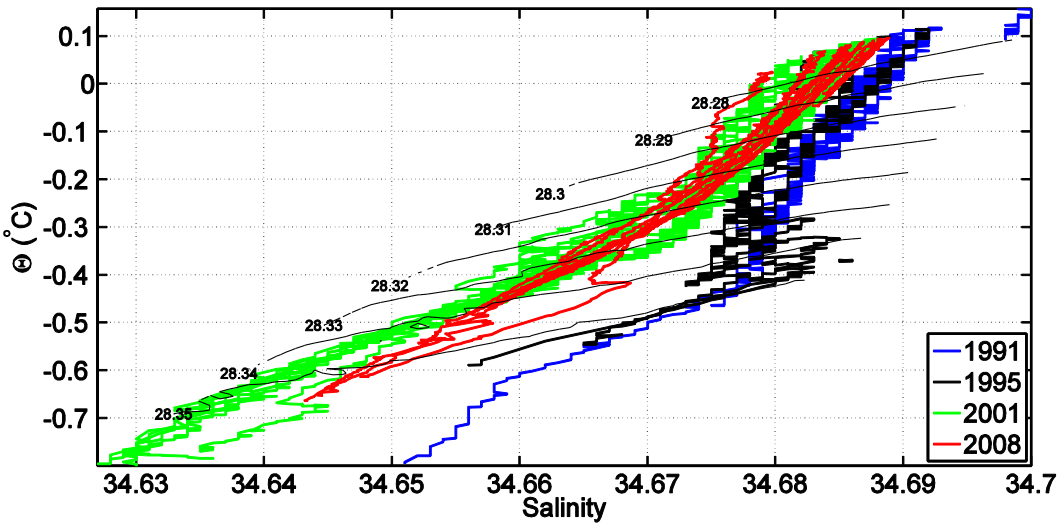

Figure 1.5. AABW θ-S from the SR3 occupations with associated CFC data. Labeled black lines are neutral density isopycnals (kg m^{-3}). The calculation of neutral densities are path dependent instead of smooth functions of θ-S, so that several possible γ^n values may exist for a particular θ-S combination.

1.4. SEASONAL BOTTOM WATER PRODUCTION FROM AGVL

1.4.1. Seasonal dense shelf overflows

The fresh, cold ALBW ventilating the abyssal AAB originates with dense shelf overflows from the Adèlie and Mertz Glacial Depressions. Mooring and hydrographic observations along the Antarctic shelf and slope show that salinity, density, and Θ anomalies associated with shelf water overflows and ALBW formation are largest in the spring (August through November) [*Fukamachi et al.*, 2000; *Williams et al.*, 2010]. These anomalies correspond to overflow properties of $\sigma_\theta >$ 27.88 kg m^{-3} ($\gamma^n \geq$ 28.35 kg m^{-3}), $\theta <$ -0.6°C, and salinities between 34.63 and 34.65.

1.4.2. Seasonal Variability in SR3 AABW Hydrographic Properties

The CTD data from the SR3 hydrographic section (Table 1.1) are grouped together by season: spring (August - November) in 1991, 1996, and 2001, summer (December - February) in 1994 and 1995, and fall (March - April) in 1993 and 2008. Bottom waters are freshest, coldest, and densest during the spring (Figure 1.6). The densest bottom waters in 1991 and 2001 have Θ of -0.8°C and S of 34.63 and 34.65, respectively, and are colder and fresher (Θ = -1.0°C, S = 34.62)

in 1996. In comparison, the densest bottom waters in summer are only as cold as -0.6°C, with S = 34.65 (1994) and S = 34.64 (1995) (Figure 1.7). The densest bottom waters in fall are cooler than those measured during the summer, with Θ = -0.65°C and S = 34.65 (Figure 1.8). The fall observations are sparser, with poor data quality at depth for the 1993 data. The coldest common observation among seasons is located along the -0.6°C isotherm at salinities between 34.64 and 34.65. The large variability in the cold, fresh densest bottom water apparently reflects the seasonality of the dense shelf overflows forming ALBW.

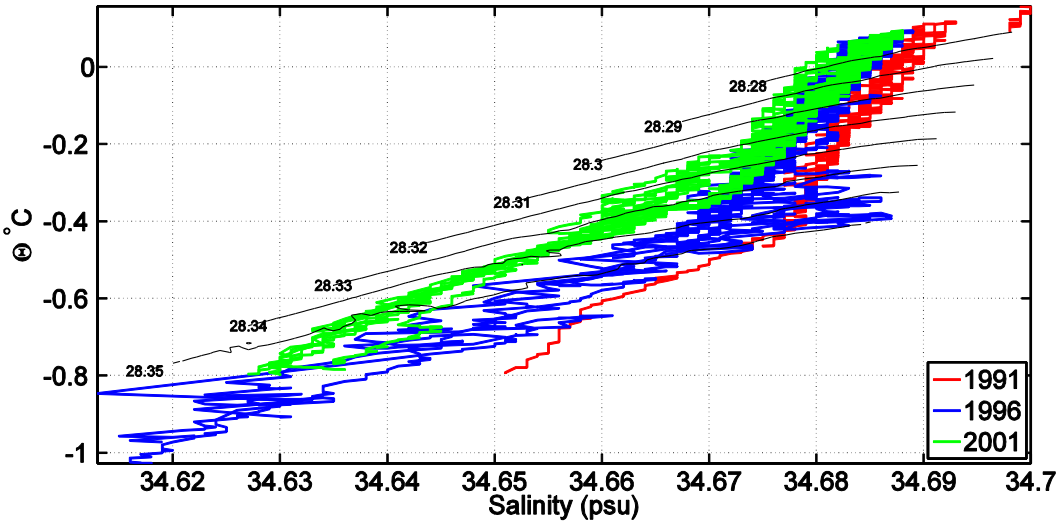

Figure 1.6. SR3 AABW θ-S is separated into seasons based on time of occupation to examine the effect of seasonal bottom water production. The spring (August – November) bottom waters are the coldest, freshest, and densest. Labelled black lines are neutral densities (kg m^{-3}).

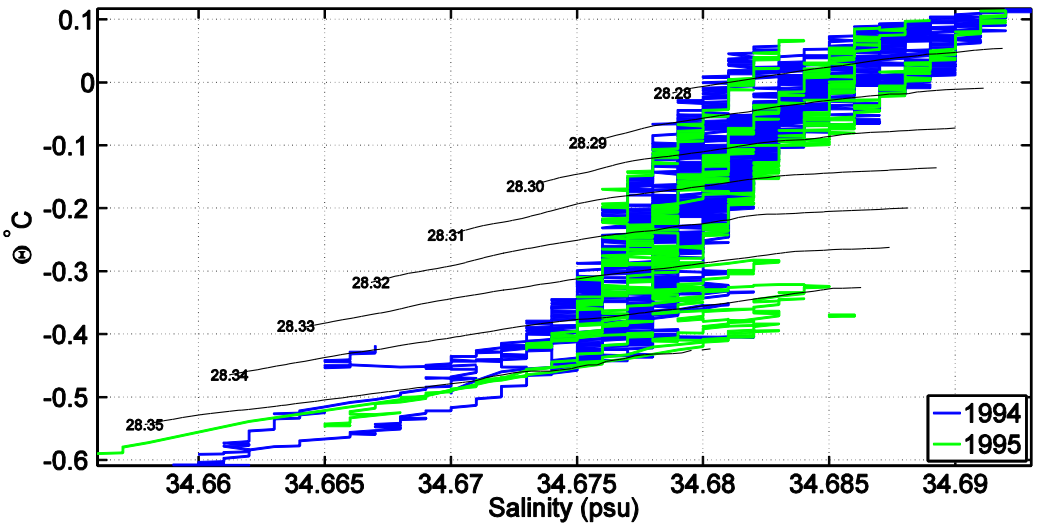

Figure 1.7. The SR3 AABW θ-S from the summer occupations show warmer, saltier, and less dense water properties than the spring occupations. Labelled black lines are neutral densities (kg m^{-3}).

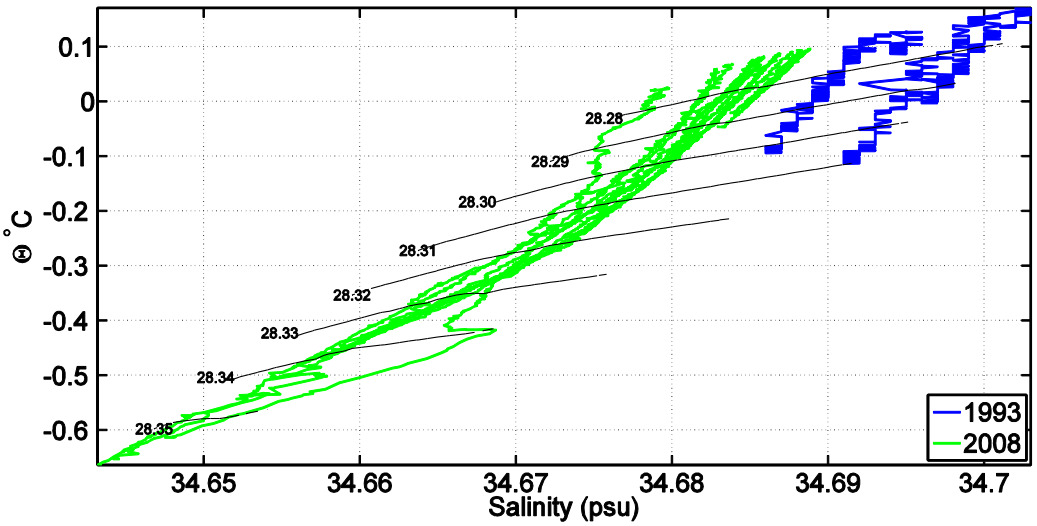

Figure 1.8. SR3 AABW θ-S from the fall occupations are slightly colder and fresher than summer values but warmer, saltier, and less dense than spring values. Labelled black lines are neutral densities (kg m^{-3}).

1.4.3. Seasonal CFC Bias

The cross-sectional areas and CFC inventories of AABW below the -0.6°C isotherms are calculated for each occupation of SR3. The -0.6°C isotherm is selected since it is the coldest common observation. Bottom waters with Θ < -0.6°C adjacent to the formation region likely reflect recently formed bottom waters and are not characteristic of the entire AAB. CFC inventories below the -0.6°C isotherm are subtracted from the total CFC inventories to correct or the inferred seasonal contribution.

The seasonal bottom water consists of the most recently ventilated bottom waters with high CFC concentrations. The seasonal bottom water contributes 2% to 14% of the total CFC inventories, with only 1% to 4% of the total AABW cross-sectional area (Table 1.2). When the seasonal signal is removed, the "seasonally-corrected" CFC inventories do not decrease between 2001 and 2008 (Figures 1.9 & 1.10).

Table 1.2. Cross-sectional area, CFC-11, and CFC-12 inventories for the seasonal component of the AABW along SR3.

Season	Year	Area (10^8 m^2)	CFC-11 (pmol m^{-1}) (% Total Inv.)	CFC-12 (pmol m^{-1}) (% Total Inv.)
Spring	1991	0.120±0.190	$3.30*10^{10}$±$3.59*10^{10}$ (7%)	$1.50*10^{10}$±$1.60*10^{10}$ (7%)
Spring	1996	0.440±0.440	-	-
Spring	2001	0.300±0.500	$12.00*10^{10}$±$5.79*10^{10}$ (14%)	$6.00*10^{10}$±$2.90*10^{10}$ (14%)
Summer	1994	0.004±0.010	-	-
Summer	1995	0.002±0.008	0	0
Fall	1993	-	-	-
Fall	2008	0.064±0.077	$1.49*10^{10}$±$0.95*10^{10}$ (2%)	$0.80*10^{10}$±$0.80*10^{10}$ (2%)

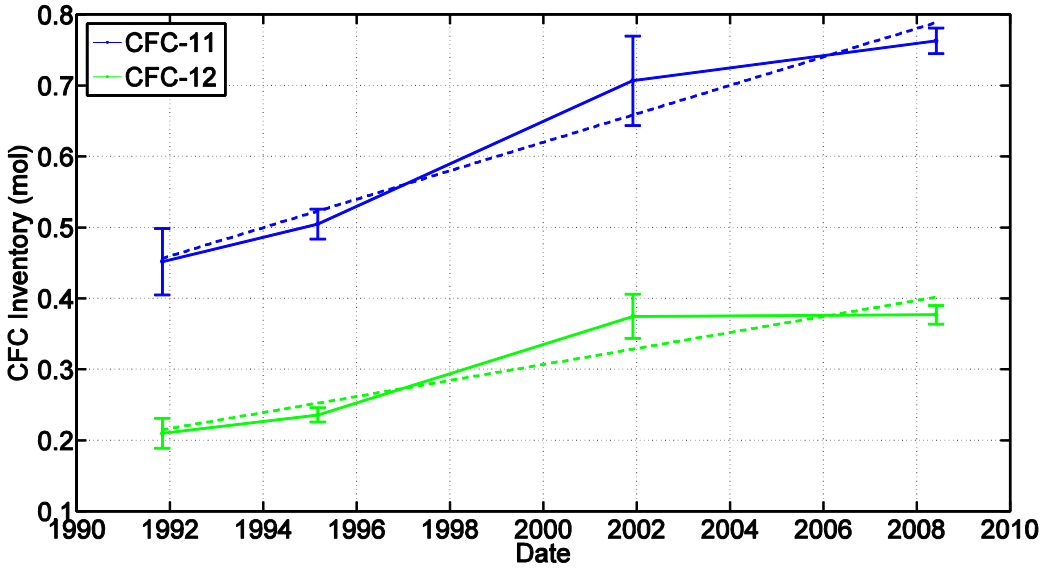

Figure 1.9. Seasonally-corrected CFC-11 (blue) and CFC-12 (green) SR3AABW total inventories (mol) with associated error.

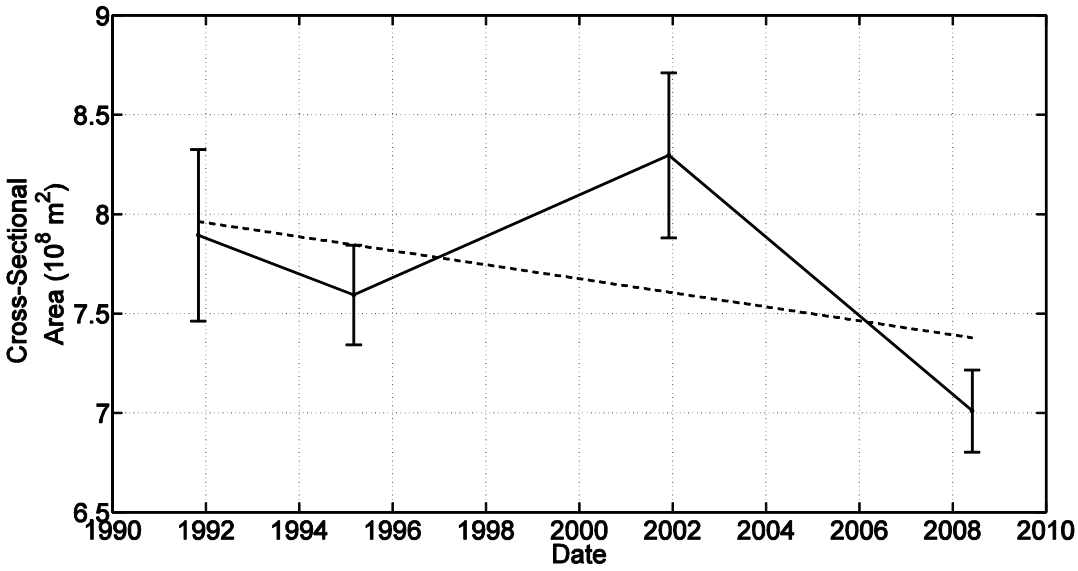

Figure 1.10. Seasonally-corrected SR3 AABW cross-sectional area (10^8 m^2).

1.5. AABW FORMATION RATES

The "seasonally-corrected" CFC inventories are used to calculate AABW formation rates following Equation 1.1. Removing the transient seasonal component reveals a multi-decadal trend suggesting decreasing bottom water production. The seasonally-corrected formation rates (Table 1.3) indicate long-term decreases of 0.012 $m^2\ s^{-1}\ yr^{-1}$ (R^2 = 0.70, CFC-12) to 0.022 $m^2\ s^{-1}\ yr^{-1}$ (R^2 = 0.66, CFC-11) (Figure 1.11). The formation rate for each occupation represents an average over a few decades, weighted towards more recent formation rates (after the 1970s) by the CFC atmospheric history, which also smooths variability. We can estimate a basin-wide input using an AAB length of $2.54*10^6$ km from *Shimada et al.* [2012] and calculate a 1 to 1.26 Sv range of AABW formation.

Table 1.3. The seasonally-corrected CFC-11 ($R_{CFC\text{-}11}$) and CFC-12 ($R_{CFC\text{-}12}$) derived formation rates ($m^2\ s^{-1}$) of AABW from the occupations of the SR3 hydrographic section in the AAB.

Year	$R_{CFC\text{-}11}$	$R_{CFC\text{-}12}$
1991	0.382±0.042	0.374±0.041
1995	0.346±0.021	0.341±0.020
2001	0.350±0.035	0.387±0.036
2008	0.301±0.015	0.304±0.017

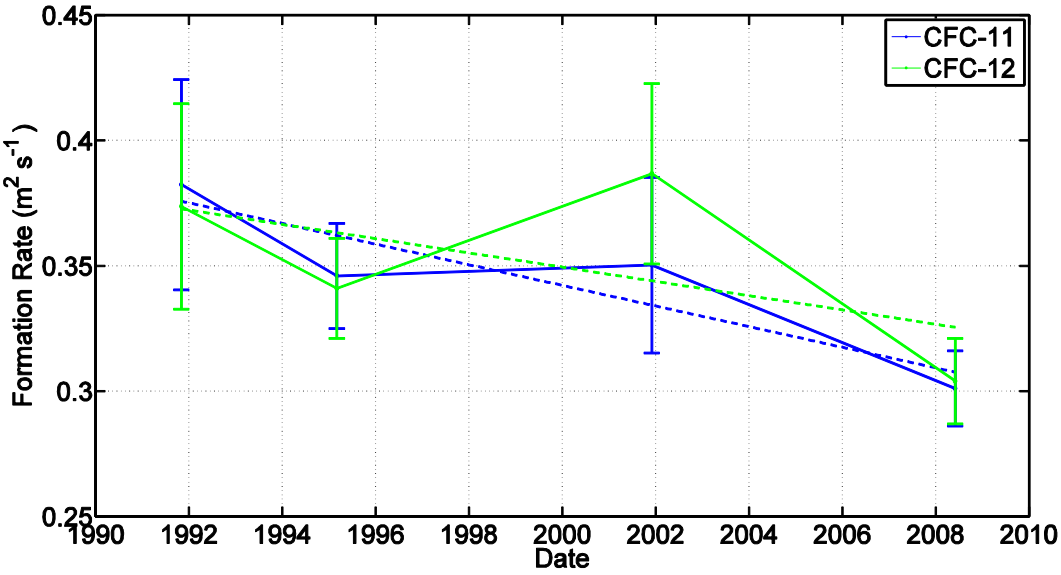

Figure 1.11. The SR3 AABW formation rates (solid lines) and associated linear regressions (dashed line) derived from the seasonally corrected CFC-11 (blue; R^2=0.66) and CFC-12 (green; R^2=0.70) inventories.

1.6. QUANTIFYING CFC LOSS

1.6.1. Advection-Diffusion Model

Our water mass formation rates (Table 1.3 & Figure 1.11) consider the loss term *L* to be 0. A meridional two-dimensional view of AABW formation from *Morris et al.* [2001] is applied to estimate *L* and determine its effect on the AABW formation rates. In this model, bottom waters enter the AAB through the SR3 hydrographic section, and are solely removed from the basin via upwelling through the 28.27 kg m^{-3} isopycnal where it lies below the 2500 m isobath and via diffuse mixing across the 28.27 kg m^{-3} isopycnal. It is assumed that there is no loss of bottom water or CFCs via lateral transport and that the SR3 section is representative of the basin as a whole. The stead-state tracer balance is calculated as:

$$\int_V \nabla \cdot (u\xi)\mathrm{d}V = (\kappa \xi_{\gamma^n})_{\gamma^n}\mathrm{d}V \qquad (1.2)$$

where *V* is the volume of the AABW, and Θ, salinity (S), and CFC concentration ([CFC]) can be substituted for ξ. Rewritten and simplified in two dimensions (latitude and depth) we derive:

$$T_{in} * \xi_{in} - T_{out} * \xi_{out} = [\kappa \xi_{\gamma^n} A]_{28.27} \quad (1.3)$$

where T_{in} and T_{out} are the mass transports into and out of the AABW, ξ_{in} and ξ_{out} are the spatially-weighted average tracer values, and ξ_{γ^n} is the spatially-weighted average tracer gradient. The term $[\kappa \xi_{\gamma^n} A]_{28.27}$ is the loss of the tracer to mixing across 28.27 kg m^{-3} isopycnal. For simplicity we assume that Θ-S is in steady-state following *Morris et al.*[2001] despite the warming in the bottom waters of the AAB, and assume that there is no loss of tracer via mass transport ($T_{out} * \xi_{out} = 0$). The diffusivity coefficient we calculate as $\kappa = 3.0 \pm 1.5$ cm^2 s^{-1}.

Now, applying the model to CFCs, an instantaneous CFC-inventory term ${}^{R}{}_{V}[CFC]_t \mathrm{d}V$ is included, where the rate of change of the CFC inventory within the volume of the AABW results from the input of newly formed AABW and loss of CFCs via advective upwelling and mixing through the 28.27 kg m^{-3} isopycnal. Integrating with respect to time yields:

$$\int_V [CFC]\mathrm{d}V = T_{in} \int_{t_1}^{t_2} [CFC]_{in}\mathrm{d}t - T_{out} \int_{t_1}^{t_2} [CFC]_{out}\mathrm{d}t - [\kappa A]_{28.27} \int_{t_1}^{t_2} [CFC]_{\gamma^n}\mathrm{d}t \quad (1.4)$$

where t_1 and t_2 are the times of reoccupation, ${}^{R}{}_{V}[CFC]\mathrm{d}V$ is the seasonally-corrected CFC inventory between occupations, $\int_{t_1}^{t_2} [CFC]_{in}\mathrm{d}t$ is the time-integrated atmospheric source function, and T_{in} is analogous to the formation rate R in (1). We assume that T_{in}, T_{out}, and $[\kappa A]_{28.27}$ are constant between t_1 and t_2, and all new CFC inventory results from input by newly formed AABW. We also assume that $[CFC]_{out}$ and $[CFC]_{\gamma^n}$ increase linearly between each cruise occupation. The calculated AABW formation rates from Equation 1.4 (T_{in}) represent the rate between two occupations. This contrasts the formation rate R from (1), which represents the long-term average formation rate from the start of the CFC-history to the time of the section occupation.

1.6.2. CFC Loss Results

The model-estimated losses of CFCs during the time intervals are less than 1% the size of the total CFC input. Inclusion of the losses in Equation 1.1 increases the 1995, 2001, and 2008 formation rates by 1%, 2%, and 2.5%, respectively. There is no information on what the loss term for the 1991 calculation may be. The AABW formation rates (T_{in}) are calculated with Equation 1.4 for each interval between CFC occupations (Table 1.4), indicating some short-term variability in the calculated formation rates, with the 1995 to 2001 formation rate nearly double those calculated form 1991 - 1995 and 2001 - 2008. This variability likely contributes to the higher

formation rates in 2001 (Figure 1.11). We do not use the CFC losses when using Equation 1.1 because inclusion in only 1995, 2001, and 2008 would bias trends relative to 1991.

Table 1.4. Calculated formation rates between occupations using equation (4), considering only the loss of CFCs from the AABW across the 28.27 kg m^{-3} γ^n isopycnal via mixing.

Year	T_{in}: CFC-11 (m^2 s^{-1})	T_{in}: CFC-12 (m^2 s^{-1})
1991→1995	0.21±0.23	0.22±0.23
1995→2001	0.39±0.23	0.53±0.29
2001→2008	0.15±0.19	0.04±0.07

1.7. ERRORS

Errors in the calculated water mass formation rates result from errors in calculating the CFC inventories and errors in calculating the formation rate. Errors in the CFC inventories result from measurement, interpolation, and mapping errors. Measurement errors for CFCs are less than 2% (0.003 - 0.005 pmol kg^{-1}), while errors from interpolation and mapping are significantly larger. A Monte-Carlo method indicates that interpolation errors range from 6.4% in 1991 to 2.1% in 2008. Errors in the atmospheric history are 2%. The sensitivity of Equation 1.1 to variability in temperature and salinity is assessed by comparing the densest bottom water Θ and S values from the bottle data with the characteristic Θ (-0.8°C) and S (34.64) of dense shelf overflows from ALGV, resulting in errors of 4.0% (4.5%) for the CFC-11 (CFC-12) solubility. Errors in the calculated formation rates are found by propagating saturation state errors of ±4% for CFC-11 (±4.5% for CFC-12), an atmospheric history error of ±2%, and the inventory errors (above) using Equation 1.1. Uncertainty in the formation rates is dominated by the CFC inventory errors, and on the order of ±7.8% in 1991 and decreasing to ±4.9% in 2008.

1.8. ALBW AND RSBW INPUTS

The potential impact of changes in RSBW on the changes along the SR3 section are examined using the S4P slope section at 170°E, which crosses the flow path of westward advected RSBW, and the Marginex [*Bindoff et al.*, 2000] and A0803 slope sections at 150°E and 140°E.

We assume that the Antarctic slope section at 150°E represents RSBW advected westward along the Antarctic Slope out of the Ross Sea that will ventilate the AAB, and that the section along 140°E represents some mixture of ALBW and RSBW from 150°E [*Bindoff et al.*, 2000; *Whitworth*, 2002].

1.8.1. S4P Observations

The Θ, S, and γ^n characteristics of RSBW along the Antarctic slope at 170°E change considerably between 1992 and 2011 (Figure 1.12) [*Swift and Orsi*, 2012]. The bottom water in 2011 is fresher and warmer (S = 34.660, Θ = -0.40°C) than in 1994 (S = 34.730, Θ = -0.75°C). The associated densities decrease from 28.47 kg m^{-3} in 1994 to 28.36 kg m^{-3} in 2011. The 28.36 kg m^{-3} isopycnal is fresher by 0.04 (34.70 → 34.66) and cooler by 0.2°C (-0.2°C → -0.4°C) during this time. The shape of the Θ-S curve changes between 1992 and 2011(Figure 1.12). Changes in the Θ and S properties of RSBW along S4P indicate changes in the Ross Sea contribution to the bottom waters on the AAB.

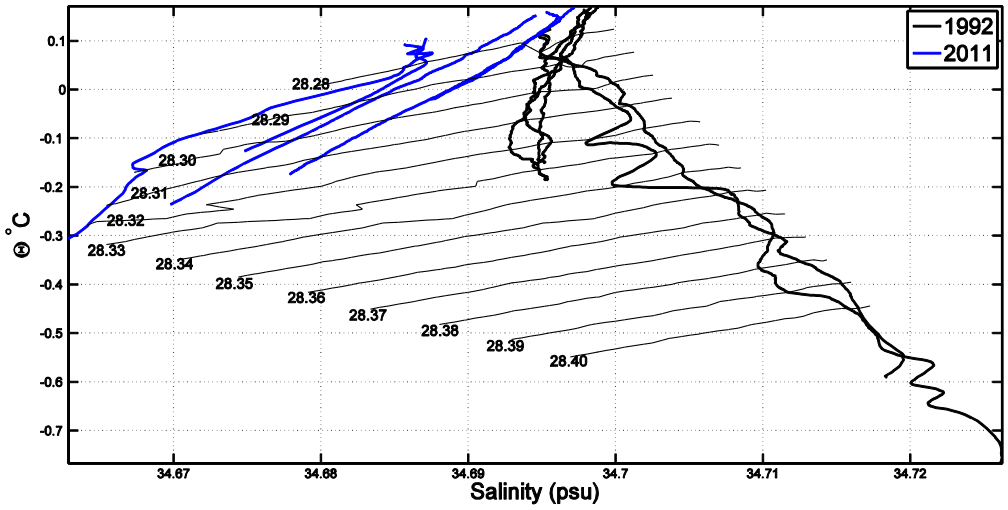

Figure 1.12. AABW θ-S from 1992 (black) and 2011 (blue) occupations of the S4P meridional section at 170°E.

1.8.2. Marginex & A0803 Observations

In 1996 there is significant modification of waters denser than 28.34 kg m^{-3} between 150°E and 140°E (Figure 1.13). Waters cooler than -0.35°C appear between the 150°E and 140°E

sections. The 28.36 kg m^{-3} isopycnal is fresher by 0.045 (34.705 → 34.660) and cooler by 0.25°C (-0.35°C → -0.60°C). The modification of the Θ-S properties below 28.34 kg m^{-3} indicates that a cold, fresh, dense water mass is introduced between 150°E and 140°E. ALBW flows downslope into the basin near East Antarctic between 142°E and 145°E. Using characteristic ALBW properties of -0.8°C and 34.64 from *Williams et al.* [2010] and assuming that mixing between ALBW and RSBW occurs along isopycnals, it appears that the RSBW contributes $1/6^{th}$ to $1/3^{rd}$ of the bottom water in the AAB. The 2008 waters are significantly different from 1996. The salty RSBW along the 150°E section in 1996 is replaced in 2008 with a cooler, fresher, and significantly lighter (28.345 kg m^{-3}) bottom water. Unlike along 150°E, the density of the bottom water along 140°E does not change between 1996 and 2008. However, the bottom water at 140°E freshens by 0.02 (34.66 → 34.64) and cools by 0.05°C (-0.6°C → -0.65°C). This freshening and cooling may reflect the changes in RSBW bottom water from upstream (at 150°E). The 2008 waters at 140°E are more representative of unmodified ALBW likely because in 2008 it is no longer influenced by the saltier and warmer waters originating in the Ross Sea.

The saltier and warmer RSBW may be related to a 17% reduction in cross-sectional area between 1996 and 2008 which corresponds to the disappearance of water denser than 28.34 kg m^{-3}. The CFC inventories calculated between the 28.27 and 28.34 kg m^{-3} isopycnals along 150°E increase by 59% and 69%, respectively, suggesting continued CFC input with bottom waters of a new, lighter density class.

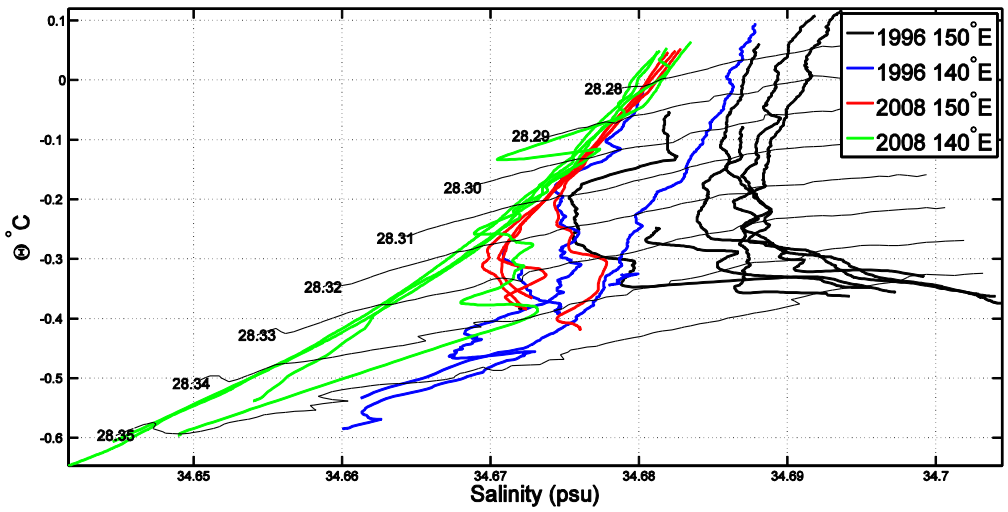

Figure 1.13. The AABW θ-S from the 1996 Marginex and 2011 A0803 meridional sections. Sections at 150°E (1996 – black, 2008 – red) are assumed to be solely RSBW. The sections at 140°E (1996 – blue; 2008 – green) consist of a mixture of RSBW advected westward from 150°E and ALBW added between 142-145°E. Labeled black lines are neutral densities (kg m^{-3}).

1.8.3. I09 Observations

Between 1995 and 2004, the bottom waters along the I09 cool (-0.5°C → -0.6°C) and freshens (34.67 → 34.65). Density remains constant, with the cooling compensating for the freshening. CFC-11 and CFC-12 Inventories increase by 51% and 49%, respectively. This closely traces the atmospheric increases of 51% (CFC-11) and 54% (CFC-12) over the same period. Volume is constant between the two occupations. The freshening and cooling of the bottom waters along IO9 is similar to the changes observed for the sections to the east.

1.9. DISCUSSION

Fukamachi et al. [2000], from a 14 month mooring record at 143°E in 1995/1996, found the average bottom water temperature and current speed (at 2632 m) from August to December to be a significant 0.27°C cooler and 5.7 cm s^{-1} faster than the average from January to July and not correlated with shallower observations (at 1778 and 1075 m). Furthermore, the densest bottom waters in spring (-1.0°C < θ < -0.8°C; 34.62 < S < 34.65; γ^n > 28.34 kg m^{-3}) correspond to the

critical properties (θ < -0.6°C; S < 34.65; $\gamma^n \geq 28.35$ kg m^{-3}) identified by *Williams et al.* [2010] necessary to initiate export of dense shelf water and formation of new ALBW. This seasonal input in ALBW formation was evident in our sections from 1991 and 2001. Since the seasonal input is associated with the highest CFC concentrations, formation rates calculated without correcting for the seasonality are likely biased. Interpretation of the CFC inventories is further complicated by uncertainty by the loss term L in (1). Using an average Southern Ocean upwelling of $2.5*10^{-7}$ m s^{-1} *Orsi et al.* [1999] estimated the loss as 17% of the total Southern Ocean CFC inventory. The 2-D advection-diffusion model we use addresses mixing across the 28.27 kg m^{-3} isopycnal, and suggests that CFC losses across the isopycnal are fairly-well quantified if it accurately reflects basin wide averages. Inclusion of the CFC losses does not significantly impact the formation rates we computed with Equation 1.1, which indicates that an increase in the rate at which AABW is mixed away is likely not responsible for the bottom water contraction in the AAB.

Variability in the formation rates between occupations likely reflects natural variability in the ocean-ice-atmopsheric interactions that produce dense bottom water originating from Adèlie Land. The doubling we inferred from 1995 to 2001 coincides with both a peak in Mertz glacial polynya area in the winter of 2001 and a trend of increasing ice production from 1992 to 2001 [*Kern*, 2009; *Tamura et al.*, 2008]. Both polynya area and ice production are critical in the on-shelf genesis of shelf-waters that form ALBW as they sink along the Antarctic slope. The longer observational record of polynya area shows no temporal trend from 1992 to 2008 [*Tamura et al.*, 2008]. With records from 1992 to 2005, *Williams et al.* [2010] separated ice production estimates between the polynyas in the Adèlie and the Mertz Glacial Depressions. Average production in the Adèlie did not change, while production in the Mertz polynya declined by 38% between 1998 and 2005. However, bottom waters originating from the Mertz Depression are intermittent and less voluminous than those from the Adèlie Depression, so variability in ALBW production likely does not contribute significantly to the decreasing AABW formation rates in the AAB.

Cooler and fresher waters on isopycnals at 140°E on SR3 through time, particularly at densities greater than 28.34 kg m^{-3}, suggest an increasing influence of ALBW likely in response to changes upstream in RSBW. The RSBW component appears to change in properties and in supply to the AAB. Freshening of the RSBW (0.03 - 0.04) between 1996 and 2008 at 150°E is consistent with the larger scale long-term freshening of the Ross Sea of -0.003 yr^{-1} [*Jacobs et al.*, 2002]. This freshening has likely resulted in a new, less dense RSBW type that replaces the older

saltier and denser RSBW, and CFC inventories at 150°E indicate that this new RSBW is less voluminous. A small change in RSBW supply may have a significant impact downstream: *Shimada et al.* [2012] suggest that a 6.7% reduction in RSBW supply may explain 84 ± 10% of the freshening and 51 ± 6% of the warming in the AAB.

A box-model suggest the RSBW slowdown of 6.7% between 1995 and 2005 may explain the CFC inventories. The box-model underestimates the 2001 and 2008 CFC-11 (CFC-12) inventories by 9.4% (19.2%) and 2.2% (4.5%). The calculated formation rate reduction of 0.8 m^2 s^{-1} out of 0.38 m^2 s^{-1} over approximately 17 years (1.2% $year^{-1}$) was also applied. This scenario overestimates the CFC-11 (CFC-12) inventories in 1995 by 5.1% (4.2%) and underestimates 2001and 2008 by 7.6% (18.2%) and 4.9% (8.2%). Both box-models assume a constant formation rate decrease and instantaneous mixing in the basin. The CFC inventories in the AABW of the AAB may be plausibly explained by the suggested 6.7% change from 1995 to 2005 in RSBW ventilating the AAB. However, the instantaneous mixing in the model likely overestimates the CFC concentrations in the water removed from the AAB box.

We approach bottom water formation as an advective process and do not explicitly characterize a diffusive component when calculating formation rates using CFC inventories. *Hall et al.* [2007] show that the advective-diffusive transport into an interior water mass cannot be accurately described as a single flux, even at steady-state. The inventory approach thus introduces tracer-based biases due to the unresolved diffusion. Rather, they propose that the flux of water may be described using a cumulative ventilation rate distribution $\Phi(\tau)$, which is a function that captures the ventilation of the water mass over a range of residence times (τ). Integrating over a large enough range of residence times should result in similar values from both the inventory and the rate distribution method. We consider the application of inventories in this study to be valid for these reasons: bottom water formation in the Southern Ocean is a principally advective process with minimal diapycnal mixing and the residence time of AABW in the AAB is equal to the tracer history, so we practically integrate over the entire transit-time distribution of the AABW.

Purkey and Johnson [2012] calculated a 2.24 (± 1.14) Sv loss of AABW in the AABW from the fall in depth of the 0°C isotherm. This could have resulted from three processes: a decrease in the formation of AABW, a change in the type of bottom water produced, or increased loss of bottom water due to mixing. Using CFC inventories, we found a trend of decreasing AABW formation in the AAB on the order of 20% over the period from 1991 to 2008. The CFC inventory

approach provides an independent measure of changes in the AAB bottom water ventilation and makes use of a different definition of AABW (28.27 kg m^{-3} isopycnal vs. 0°C isotherm). This suggest the contraction in the AABW observed by *Purkey and Johnson* [2012] is at least partly the result of decreasing AABW formation.

In summary, the CFC inventories indicate a reduction in bottom water formation ventilating the AAB that is consistent with the results from *Purkey and Johnson* [2012]. Variability between occupations is likely due to normal variation in polynya area and ice production in the Adèlie and Mertz Glacial Depressions and does not appear to contribute to the long-term decrease in AABW formation. We conclude that significant freshening and volume contraction in the supply of RSBW to the AAB likely contributes to the calculated reduction of AABW formation and we infer it is the reason for the freshening and cooling along isopycnals along SR3. The Θ-S of the bottom waters in the AABW from 1991 to 2008 shift to Θ-S characteristic of unmodified ALBW, reflecting a greater influence of ALBW due to a decreasing contribution of RSBW.

Chapter 2. A GAS TENSION DEVICE FOR THE MESOPELAGIC ZONE

Andrew Reed[a,b,*], Craig McNeil[a,b], Eric D'Asaro[a,b], Mark Altabet[c], Annie Bourbonnais[c], and Bruce Johnson[d]

[a]School of Oceanography, University of Washington, 1503 NE Boat Street, Box 357940, Seattle, WA 98195, USA

[b]Applied Physics Laboratory, University of Washington, 1013 NE 40th Street, Seattle, WA 98105, USA

[c]School for Marine Science and Technology, University of Massachusetts Dartmouth, 706 Rodney French Blvd, New Bedford, MA 02744, USA

[d]Department of Oceanography, Dalhousie University Faculty of Science, 1355 Oxford Street, Halifax, Nova Scotia, Canada B3H 4R2

2.1. INTRODUCTION

Measurements of dissolved gases are widely used in oceanography, limnology, and aquaculture, with dissolved O_2 being the third most frequently measured property of seawater after temperature and salinity. Dissolved gas measurements have been used to study: ocean carbon uptake and acidification [Takahashi et al. 1997]; bubble mediated air-sea gas exchange [Emerson & Bushinsky 2016]; biological production and net community metabolism [McNeil et al. 2006b]; monitor water quality for juvenile hatchery fish downstream of dam spillways [Bragg & Johnston 2016]; denitrification/anammox in anoxic natural and waste waters [Löffler et al. 2011]; and investigate groundwater recharge and trapped gas phases [Manning et al. 2003]. Of particular interest are the four major atmospheric components, namely nitrogen (N_2), oxygen (O_2), argon (Ar), and carbon-dioxide (CO_2). Having the largest dissolved concentrations and partial pressures, these gases are the most easily measured using conventional techniques. Since they are important to numerous biological and chemical processes, and noting the widespread use of these measurements, there is a continued need to improve dissolved gas sensor measurement technology

to overcome current limitations, such as depth dependence, response time, calibration stability, interferences, cost, and power consumption, and improve basic performance characteristics, such as accuracy and resolution.

Of these four gases, dissolved CO_2 and O_2 are the most chemically reactive. Dissolved aqueous CO_2 is normally measured using a nondispersive infrared sensor (NDIR) [Hales et al. 2004]. Dissolved O_2 is measured most accurately using discrete water samples analyzed by the Winkler titration method [Langdon 2010]. Several commercially-available in-situ sensors based on polarographic or fluorescence quenching methods are also used for O_2. Less-reactive dissolved N_2:Ar are measured by mass spectrometry (MS) or gas chromatography [Groffman et al. 2006]. All techniques that require collection, storage, transport, and subsequently analysis of discrete water samples are subject to numerous opportunities for contamination or alteration of the water samples. An in-situ sampling method for measuring dissolved N_2 will help address most of these issues.

A gas tension device (GTD) measures the gas tension which is subsequently used to derive in-situ dissolved N_2 if dissolved O_2 is also measured [McNeil et al. 1995]. The first measurements of in-situ dissolved gas measurements were the tensiometer from D'Aoust et al. [1975] and the Weiss saturometer, with accuracies of 3% [Fickeisen et al. 1975]. Gas tension is the total pressure of dissolved gases in a parcel of water. In a GTD a semipermeable membrane is used to equilibrate a small volume of gas trapped behind the membrane with the gases dissolved in the surrounding water. When the GTD's gas volume is equilibrated with the seawater sample, a barometer in the GTD measures gas tension. Using concurrent measurements of gas tension, dissolved O_2, temperature and salinity, and measured or assumed saturation levels for Ar and pCO_2, dissolved N_2 can also be determined to a final accuracy of ±0.7% [McNeil et al. 1995; McNeil et al. 2005].

A custom GTD was designed and used on profiling floats [McNeil et al. 2006a] to measure the rapid changes in gas tension in the ocean mixed layer during the passage of a hurricane [D'Asaro & McNeil 2007]. That GTD used a tubular polydimethylsiloxane (PDMS) membrane with a large surface area and low-internal volume to achieve a response time of minutes. The compressibility of PDMS resulted in two major complications with this GTD. First, the membrane's permeability decreased with increased hydrostatic pressure which resulted in a significantly slower response at increased depths and a hysteresis in the gas tension profiles. Second, the release (uptake) of gases from the membrane during compression (decompression)

resulted in large transient positive (negative) pressure fluctuations in the raw GTD measurements. Another more severe problem was sporadic clogging of the membrane, likely caused by reverse osmosis of liquid water through the membrane into the barometer. These limitations excluded GTD-equipped floats from deep (below 60 meters) or extended deployment and increased measurement error.

This paper describes a new GTD designed to overcome these limitations. Our motivation is to measure dissolved N_2 on profiling floats deeper in the ocean and specifically in oxygen deficient zones (ODZs) to study the biological production of N_2 via the denitrification and anammox processes. We expect a N_2-excess signal of 10 – 20 mbar out of a background 850 mbar based on the N-excess from Chang et al. 2012. We begin by presenting the design of the new GTD and describing the new materials involved. Next, we lay out the background theory of gas tension measurements, which is used to construct a model which describes the temperature and hydrostatic pressure dependencies. The GTD is then characterized in the laboratory using the developed model, followed by testing in the Puget Sound, and finally deployment in the Eastern Tropical North Pacific (ETNP) ODZ. Then, we present the results of the lab experiments and field testing, with the Puget Sound and ETNP results validated against an independent gas tension estimate calculated with concurrent measurements of dissolved O_2 and N_2:Ar ratios determined by mass spectrometry. Lastly, we discuss how the new GTD-design is an improvement over the previous versions, what needs further development, and future field applications.

2.2. INSTRUMENT DESIGN

Autonomous profiling Gas-floats (Applied Physics Lab, University of Washington), which alter their buoyancy to settle at different isopycnals in the water column, offer a platform for frequent sampling of multiple seawater properties through time and space. An ideal float-mounted gas tension device would measure the gas tension with a rapid (seconds) equilibration (response) time, function independently of temperature and hydrostatic pressure, and function reliably for long-periods of time on autonomous platforms. The previous float-mounted GTD utilized a large (1 m length x 3 cm diameter) tubular PDMS membrane to achieve minute response times [McNeil et al. 2006a]. However, the previously discussed issues of the PDMS-membrane meant the GTD required frequent maintenance and limited possible applications [McNeil et al. 2005; McNeil et al. 2006a].

The new GTD design is shown in Figure 2.1. It has three main components: (1) a pressure housing, (2) a flushed membrane interface, and (3) a seawater pump. The new design is more compact than the previous version, making it easier to mount and protect. The compressible PDMS membrane is replaced with a nearly-incompressible Teflon-AF 2400 membrane (DuPont). This switch of material reduces response times with hydrostatic pressure and the hysteresis, improving performance and accuracy of the instrument.

However, Teflon-AF 2400 is a difficult material to make flat membranes from because it is brittle and thin sheets of it tend to curl. We settled on a 4 cm diameter by 130 μm thick membrane after some experimentation. The membrane is supported on the non-water side by a fine stainless-steel support mesh. The membrane and support mesh are anchored in a membrane-housing manufactured from Delrin. Stainless-steel 1/16" tubing connects the membrane housing to a Paroscientific Digiquartz Pressure transducer (0-30 psia), which has a manufacturer's stated precision of 0.0001% and accuracy of 0.01%. The pressure transducer and associated electronics are protected in a separate pressure-housing. Barometric pressure and internal temperature of the GTD is recorded by the float.

The water-side face of the membrane is covered with a plenum that is connected to a SBE5T seawater pump. Flushing the membrane significantly reduces the equilibration time by shrinking the boundary-layer that forms along the membrane-seawater interface. The plenum is a plastic cap with the water inlet situated over the membrane and several small outlets, with their total area less than the inlet, spaced radially around the side of the plenum. This directs the water onto the membrane and shears radially, and maintaining a slight positive pressure to ensure the membrane is held flat against its support. The pump is controlled by the GTD electronics and operates on three settings: 100% (continuous), 50% (laboratory only), and 10% (pulse) pumping cycles. Pulse mode is preferred to conserve energy and prolong battery life. Continuous mode is activated during surfacing to protect the membrane from possible damage when bubble and temperature-induced supersaturations at the surface may exceed the hydrostatic pressure, causing ballooning and tearing in the membrane. The GTD mounted on the Argo-float is the same as those mounted on the gas-sensing floats, except it is unpumped and the membrane is left uncovered to improve passive flushing.

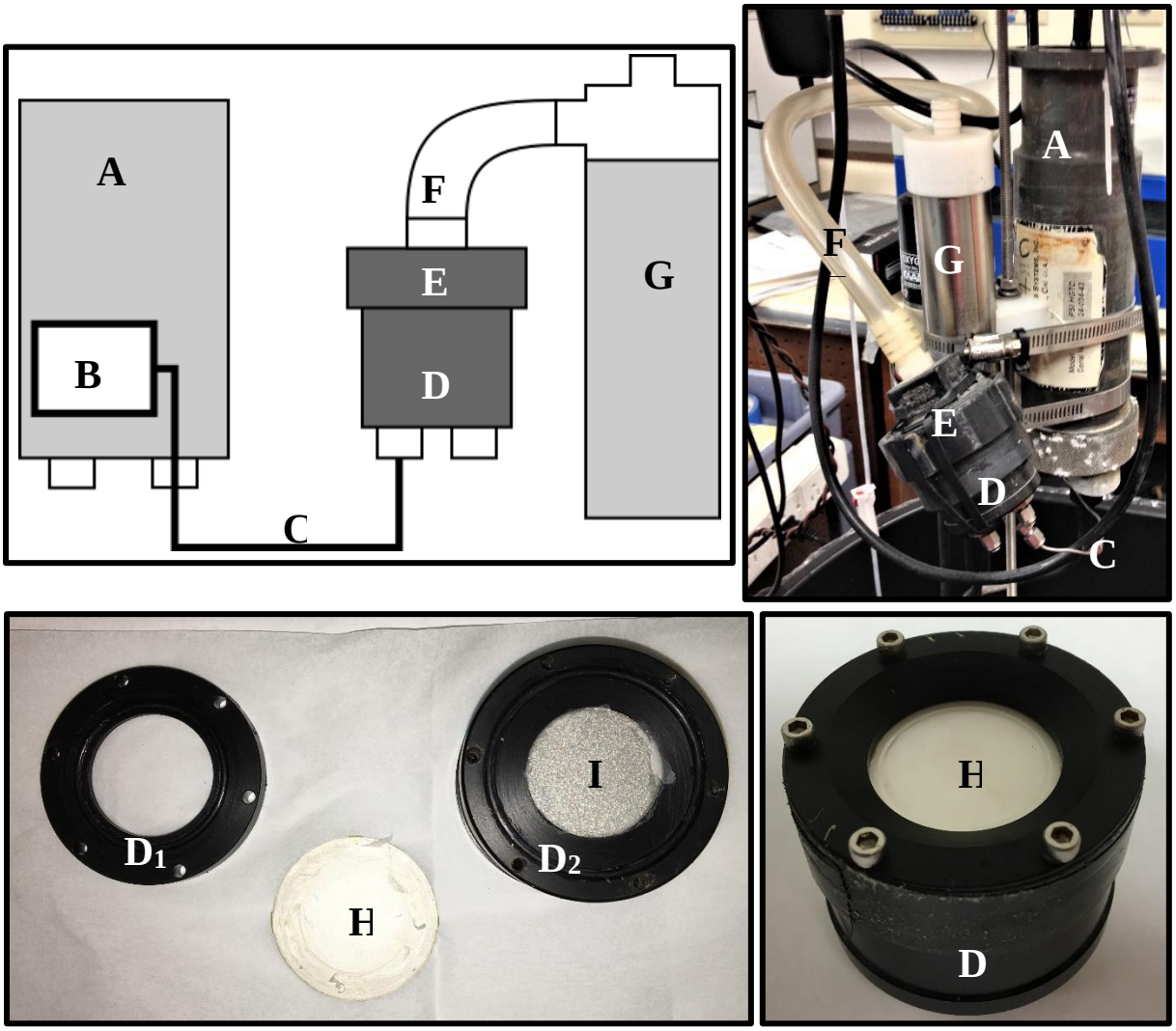

Figure 2.1. Schematic and pictures of the new GTD, showing clockwise from the top left, the assembled GTD with pump, the disassembled membrane housing, and the membrane housing. A: Pressure housing and electronics, B: Paroscientific barometer, C: 1/16” stainless steel tubing, D: assembled membrane housing (D1: membrane collar, D2: main membrane housing), E: plenum, F: plastic tubing, G: Seabird 5T pump, H: Teflon membrane and support, I: Stainless steel mesh support.

2.3. METHODS

2.3.1. Theory & Modeling

2.3.1.1. Gas Tension in Seawater

A measurement of gas tension in seawater needs to be corrected for hydrostatic pressure and temperature [Hamme et al. 2015]. This can be seen with the following derivation for the gas tension changes in a parcel of water. Gas tension (*GT*) of seawater is defined as the sum of all the partial pressures (p_i) of the dissolved gases in seawater:

$$GT = \sum_i p_i = pN_2 + pO_2 + pAr + pH_2O + pCO_2 + pTrace \quad (2.1)$$

In the above equation i denotes contributions due to individual gases [McNeil et al. 1995]. We define the total contribution to gas tension of all traces gases (including neon, krypton, nitrous oxide, methane, et al.) with partial pressures less than pCO_2 by $pTrace$. The relative contribution of each denoted gas to a measurement of gas tension in two different types of seawater are shown in Table 2.1. For the first water type (Table 2.1, Column 1a) we chose representative values of the core of the ODZ in the ETNP off Mexico. Since these waters are anoxic, there is no contribution to gas tension by dissolved oxygen. Dissolved nitrogen contributes more than 97.3% of the gas tension, with another 1.3% from water vapor, 1.1% from argon, 0.16% from carbon dioxide, and less than 0.02% from other trace gases. In anoxic ODZ core waters, a small percentage (typically <4% or <30 mbar) of the measured pN_2 is associated with microbial denitrification and anammox of nitrogen containing nutrients. For the second water type (Table 2.1, Column 2a), we chose surface waters in equilibrium with the atmosphere in the same location. Compared to the ODZ core waters, gas tension in the oxygenated surface water is significantly larger (>15%), and pH_2O increased sharply with increased temperature by approximately a factor of three.

The classical Henry's Law is used to relate the partial pressure, p_i, of a dissolved gas in water to the concentration, $[C_i]$, of the dissolved gas by:

$$p_i = \frac{[C_i]}{Sol_i(T,S)} \quad (2.2)$$

The Henry's Law solubility $Sol_i(T,S)$ for a gas is dependent on water temperature (*T*) and salinity (*S*). However, Klots [1961] identified that hydrostatic pressure also influenced Sol_i, which

depended on the partial molal volume of the gas in solution. The importance of this effect when utilizing a GTD was identified by Hamme et al. [2015].

The GTD makes a measurement of the pressures of all the dissolved gases at equilibrium with the surrounding water. Consequently, we used a modified form of Henry's Law which replaced the gas partial pressures with the gas fugacities, which more accurately represented the effective partial pressures of the gases in chemical equilibrium with the effective (i.e. actual) concentrations. Following Ludwig and MacDonald [2005], the effect of hydrostatic pressure on gas fugacities was expressed as:

$$\left(\frac{\partial \ln(f_i)}{\partial P}\right)_{T,C_i} = \frac{V_i}{RT_K} \tag{2.3}$$

where f is the fugacity (atm), V_i is the molal volume (ml mol^{-1}), R is the universal gas constant (≈82.057 mL atm mol^{-1} K^{-1}), and (T_K) is the absolute temperature (K). Assuming constant molal volumes and concentrations, integrating between hydrostatic pressures and solving for the fugacity yielded [Ludwig & MacDonald 2005]:

$$f_i(P) = f_i(P = 1) \cdot e^{\frac{V_i * \Delta P_H}{RT_K}} \tag{2.4}$$

At ambient (surface) pressure, the fugacity $f_i(P)$ is equal to the surface f_i of the gas. Thus, the in-situ gas fugacity at a particular hydrostatic pressure is equal to the gas fugacity at the sea surface scaled by the change in hydrostatic pressure ΔP_H (atm) and the gas molal volume (V_i). Equation 2.4 predicted an increase in gas tension of approximately 14% per 1000 dbar using partial molal volumes of N_2 ≈ 33.1 ml mol^{-1}, O_2 ≈ 32.0 ml mol^{-1}, and Ar ≈ 32.1 ml mol^{-1} [Hamme et al. 2015]. This agreed with the results from an experiment by Enns et al. [1964].

The physical interpretation of Equation 2.4 is that increased hydrostatic pressure increased the tendency of gas to leave solution, or, equivalently, increased hydrostatic pressure decreased gas solubility (concentrations remain unchanged). We recast Equation 2.2) to relate the in-situ gas fugacity as a function of dissolved gas concentrations and a hydrostatic pressure dependent gas solubility:

$$f_i(P) = \frac{[C_i]}{Sol_i(T,S,P)} \tag{2.5}$$

The effect of rapidly (i.e. adiabatically and with no change in the dissolved gas concentrations [µM/kg]) altering hydrostatic pressure by 400 dbar on seawater gas tension is

shown in Table 2.1 for representative ODZ core waters (Column 1b), and for air-saturated surface waters (Column 2b). For a surface seawater sample that was initially in equilibrium with the atmosphere and then taken rapidly to 400 dbar, the sample's gas tension will increase by approximately 5.2% due to a decrease in the solubility of the gases. Conversely, bringing a seawater sample from the ODZ core to the sea surface, as occurs during a hydrocast, will cause a decrease in gas tension of approximately 5.4% due to an increase in gas solubilities. Note that in both examples, the effects of changes in temperature (< 0.1 °C) due to adiabatic expansion/contraction on gas solubility are small (5.4% vs 5.2%). Not correcting for the hydrostatic pressure effect will lead to systematic overestimation of in-situ gas tension and, consequently, gas concentrations. The effect of the pump's pressure head is negligible if the hydrostatic pressure is relatively large.

Table 2.1. Dissolved gas composition of a seawater parcel varies significantly between the oxic and anoxic ocean. The individual partial pressures of dissolved gases with their approximate absolute levels (in mbar) and best error estimates that comprise the gas tension of seawater for anoxic core ODZ (Column 1a) using our measurements at 400 dbar in the ETNP, and for surface seawater in equilibrium with the atmosphere (Column 2a) using observations at the sea surface at the same location. Calculations based on an assumed adiabatic change in hydrostatic pressure of 400 dbar by either raising a sample of the anoxic core to the sea surface (Column 1b) or lowering a sample from the sea surface to 400 dbar depth (Column 2b). Argon is assumed saturated ±5%, which is a maximum likely deviation from equilibrium [Hamme & Emerson 2004]. Oxygen within the ETNP ODZ core was measured on the order of ≈100 nM [Tiano et al. 2014]. CO_2 is taken from the World Ocean Database [Boyar et al. 2013]. Water vapor is assumed to be 100% saturated and calculated as an explicit function of temperature and adjusted for salinity effects. Gas tension values are taken from lab and/or field measurements. *We assume that at the ocean surface the gas fugacities behave as ideal gases such that the fugacity is equal to the gas partial pressures p_i. This means that there is no hydrostatic pressure effect at 0 dbar.

	Anoxic ODZ Seawater T=9.6°C, S=34.65			**Atm. Equilibrated Seawater T=28.0°C, S=34.72**		
Column	1a	1b	% Total	2a	2b	% Total
Hydrostatic Pressure	400 dbar	*0 dbar*		0 dbar	*400 dbar*	
Gas Tension	878.9 ±1.2	*831.2 ±1.2**	100	1013.3 ±0.2*	*1066.0 ±3.8*	100
fN_2	855.4 ±2.6	*808.7 ±2.6**	97.3	762.3 ±1.1*	*803.5 ±1.2*	75.2
fO_2	< 0.1	*< 0.1**	< 0.1	204.5 ±1.0*	*215.2 ±1.1*	20.2
fAr	9.9 ±0.5	*9.4 ±0.5**	1.1	9.1 ±0.5 *	*9.6 ±0.5*	0.9
fCO_2	1.4 ±0.2	*1.3 ±0.2**	0.2	0.3 ±0.2*	*0.3 ±0.2*	< 0.1
fTrace	< 0.2	*< 0.2**	< 0.1	< 0.2*	*< 0.2*	< 0.1
fH_2O	11.8 ±0.3	*11.7 ±0.3**	1.4	37.1 ±0.3*	*37.4 ±0.3*	3.7

2.3.1.2. Observing Temporal Changes of Gas Tension

Observations of gas tension are first made in the laboratory using a sealed pressure test vessel to understand how the new GTD responds to rapid in situ changes in hydrostatic pressure at constant temperature and dissolved gas concentrations. In practice, the test vessel slowly warmed as the room changed temperature and the dissolved oxygen concentration inside the test

tank decreased due to oxidation (microbial and chemical). We compensated for these relatively small and slow variations in gas tension during analysis. In the field, a Lagrangian float carried the new GTD which equilibrated to the gas tension of individual parcels of water which the float tracked over time. There are similarities between these two measurement approaches which influenced how we formulated the description of the sensor response below. Our intent is to process both data sets similarly. For both types of data sets, changes in temperature and dissolved gas concentrations in the water parcel or enclosed in the pressure test tank are assumed to vary slowly compared to the response time of the sensor to achieve equilibrium of the GTD. We do not use the GTD in a CTD-like profiling mode.

We start by considering the changes to the gas tension of a single water parcel with time (dGT^{sw}/dt). We decompose the changes into several independent components: those due to the temperature effect on solubility ($\partial GT^{sw}/\partial T$), the hydrostatic pressure effect on solubility ($\partial GT^{sw}/\partial P$), the water vapor partial pressure ($\partial pH_2O/\partial T$), and any internal sources or sinks (R):

$$\left(\frac{dGT^{sw}}{dt}\right) = \frac{\partial GT^{sw}}{\partial T}\frac{\partial T}{\partial t} + \frac{\partial GT^{sw}}{\partial P}\frac{\partial P}{\partial t} + \frac{\partial (pH_2O)}{\partial T}\frac{\partial T}{\partial t} + Q \tag{2.6}$$

The superscript *sw* indicates seawater. The temperature and hydrostatic pressure terms are a combination of the individual solubility changes to dissolved N_2, O_2, and Ar, scaled by their respective atmospheric mole fractions. For simplicity we separate the water vapor partial pressure contribution to the gas tension. We ignore the small changes in solubility due to salinity variations.

We linearize the dependencies of Equation 2.6 with the following substitutions: α (%/°C) for the temperature effect on gas tension, β (%/1000 dbar) for the hydrostatic pressure effect on gas tension, and γ (mbar/°C) for change in water vapor due to temperature, and scale the changes with respect to the initial gas tension of the seawater parcel GT_0^{sw}:

$$\alpha \equiv \frac{1}{GT_0^{sw}}\frac{\partial GT^{sw}}{\partial T}, \quad \beta \equiv \frac{1}{GT_0^{sw}}\frac{\partial GT^{sw}}{\partial P}, \quad \gamma \equiv \frac{\partial pH_2O}{\partial T}$$

This yielded a simplified linear expression for Equation 2.6:

$$\left(\frac{dGT^{sw}}{dt}\right) = GT_0^{sw}\left(\alpha\frac{\partial T}{\partial t} + \beta\frac{\partial P}{\partial t}\right) + \gamma\frac{\partial T}{\partial t} + Q \tag{2.7}$$

The above equation described the specific case where the sampled water parcel has no external exchange with the surrounding environment, such as in a laboratory setting.

Integrating Equation 2.7 with respect to time yielded a discrete expression for the water gas tension at time *t* (subscript t) with changes due to temperature, hydrostatic pressure, and biology:

$$GT_t^{sw} = GT_0^{sw} + GT_0^{sw}\big(\alpha(T_t - T_0) + \beta(P_t - P_0)\big) + \gamma(T_t - T_0) + Q(t - t_0) \quad (2.8)$$

Note that Equation 2.8 describes the actual gas tension in the water parcel, which responds instantaneously to changes in the driving forces *P*, *T*, and *Q*.

Now we discuss the response of the sensor, i.e. the GTD, to the change in gas tension of the water parcel surrounding the sensor. A change in the gas tension of the surrounding water parcel (Equation 2.6) creates a gas pressure differential across the GTD membrane between the dry and water-facing sides. This difference in pressure equilibrates with a characteristic response time τ. The sensor output (GT_t^{GTD}) is a low-pass filtered (i.e. smoothed) version of the water gas tension (GT_t^{sw}). Note the use of superscripts to differentiate between the gas tension in the water (*sw*) and the output from the GTD (*GTD*). We modeled the change in the GTD output (dGT^{GTD}/dt) as a mathematical convolution operation $(*)$ of the changing seawater gas tension (dGT^{sw}/dt) with the sensor response $\left(\frac{1}{\tau}e^{\frac{-t}{\tau}}\right)$:

$$\frac{dGT^{GTD}}{dt} = \frac{dGT^{sw}}{dt} * \frac{1}{\tau}e^{\frac{-t}{\tau}} \quad (2.9)$$

Importantly, the pressure measured by the barometer in the GTD is not the seawater gas tension until the GTD is fully equilibrated (i.e. $t > 5\tau$). In-situ seawater gas tension is obtained by deconvolving (i.e. reversing the convolution in Equation 2.9) the measured GTD time series with the sensor response. The response time of the GTD depends on both the flushing of the water-side boundary layer and the gas flux through the membrane, which is temperature dependent. Consequently, the response time for any particular deployment or experiment may vary based on the environment, the geometry of the GTD setup, and available power for pumping or flushing. As a result, we calculate a new optimal response time for each individual deployment or laboratory experiment. However, convolution/deconvolution of a time series requires that the response time be constant for the entire time series. For an analysis of how pumping affects the response of a GTD (not the same as the one analyzed here), please see McNeil et al [2006a].

The temperature dependence of the response time is related to the temperature dependence of the membrane permeability. Gas transport across a non-porous polymer, such as Teflon-AF,

occurs via a solution-diffusion process. The membrane permeability P_m is a function of the membrane solubility S_m and membrane diffusivity D_m [Pinnau & Toy 1996]:

$$P_m = S_m \times D_m \tag{2.10}$$

Previous characterization of Teflon-AF 1600 demonstrated that the permeation rates of light gases, such as N_2, O_2, and CO_2, increased with increasing temperatures and concentrations but were independent of pressure [Alentiev et al. 2002]. Additionally, permeability was inversely related to molecular size [Alentiev et al. 2002; Bernardo et al. 2009]. These properties indicate that permeability of Teflon-AF is diffusion-limited, and hence the temperature dependence (i.e., $\partial P_m/\partial T$) primarily controlled by the temperature dependence of D_m rather than S_m (i.e., $S_m \times \partial D_m/\partial T >> D_m \times \partial S_m/\partial T$).

Equilibration time for a diffusion-limited processes was calculated as a function of the membrane diffusivity (D_m), the membrane thickness (h), surface area (A), and the total sample volume of the GTD (V) using:

$$\tau(T) = \frac{hV}{D_m(T)A} \tag{2.11}$$

The thickness, surface area, and volume were constants independent of temperature. Thus, the response time is a function of temperature $\left(\tau(T)\right)$ and will be inversely related to the temperature-induced changes in membrane diffusivity.

Diffusion-dominated gas-permeation temperature dependence through Teflon-AF is typically empirically fit using an Arrhenius equation [Pinnau & Toy 1996; Alentiev et al. 2002]. We assumed a similar temperature-dependence of the response times:

$$\frac{1}{\tau(T)} = \frac{1}{\tau_0} e^{-\frac{E}{RT}} \tag{2.12}$$

The pre-exponential factor τ_0 (s^{-1}) and constant E (kJ mol^{-1}) are calculated from a linear fit to the plot of $\ln(1/\tau)$ against $1/T$ (Arrhenius plot).

Teflon-AF is eight-fold more permeable to water vapor than nitrogen [Bernardo et al. 2009]. Thus, we calculated the water vapor contribution as an instantaneous signal. Gas tension with the water vapor subtracted is referred to as dry gas tension. Substituting Equation 2.7 into Equation 2.9 and integrating with respect to time yielded an analytical solution of the GTD behavior to a change in the gas tension of the water parcel:

$$GT_t^{GTD} = GT_0^{GTD} + \left(GT_0^{sw}\left(\alpha(T_t - T_0) + \beta(P_t - P_0)\right) + Q(t - t_0)\right) * \frac{1}{\tau} e^{\frac{-t}{\tau}} + \gamma(T_t - T_0) \quad (2.13)$$

2.3.1.3. Modeling Gas Tension

We adapted Equation 2.13 by letting $GT_t^{GTD} = GT_t^{Model}$. We also assume that the GTD starts out in both thermal and gas tension equilibrium with the surrounding seawater, so that $GT_0^{GTD} = GT_0^{sw}$. The result is a step-response model that predicted the gas tension recorded by the GTD at time *t*. This model was applied to derive the best fits for the parameters α, β, τ, and Q, which were calculated using a global unconstrained minimization routine [Lagarias et al. 1998]. The algorithm trained the best-fit parameter values by minimizing the MSE between the measured time series (GT_t^{GTD}) and the model of the GTD $\left(GT_t^{Model}\right)$:

$$(\alpha, \beta, \tau, Q)_{Best} = \min\left(\frac{1}{n}\sum_{t=1}^{n}\left(GT_t^{GTD} - GT_t^{Model}\right)^2\right) \quad (2.14)$$

Using the best fit α, β, and Q, we can calculate a normalized gas tension (GT^{norm}) time series by removing the effects of temperature, hydrostatic pressure, biology, and water vapor:

$$GT_t^{norm} = GT_t^{GTD} - GT_0^{GTD}\alpha(T_t - T_0) - GT_0^{GTD}\beta(P_t - P_0) - Q(t - t_0) - \gamma(T_t - T_0) \quad (2.15)$$

Applying Equation 2.15 yielded an idealized isothermal, isobaric model of constant gas tension with an explicit solution for an individual re-equilibration:

$$GT_t^{Model} = GT_0^{norm} + (GT_0^{sw} - GT_0^{norm})e^{-\frac{t}{\tau}} \quad (2.16)$$

An example is shown in Figure 2.3. This idealized model allowed an independent check of the response time of the sensor by a regression fit of the data from the experiment to Equation 2.16. The result was multiple estimates of τ at different hydrostatic pressures to determine the pressure dependence of τ.

In addition to changing gas levels, profiling between surface and depth may also create a difference between the internal GTD temperature (T^{GTD}) and surrounding water temperature as measured by the float CTD (T^{CTD}). This difference exists because the barometer and the electronics pressure housing contain significant mass, much of which is not in direct contact with the surrounding water (Figure 2.1). The GTD thermal response time φ described the equilibration of T^{GTD} to T^{CTD}. We constructed a model to fit φ by first quantifying the changes of the GTD

temperature with respect to time (dT^{GTD}/dt) as a convolution of the change in temperature measured by float CTD (dT^{GTD}/dt) with a characteristic temperature equilibration $\left(\frac{1}{\varphi}e^{-\frac{t}{\varphi}}\right)$:

$$\frac{dT^{GTD}}{dt} = \frac{dT^{CTD}}{dt} * \frac{1}{\varphi}e^{-\frac{t}{\varphi}} \tag{2.17}$$

Equation 2.17 has an explicit solution of the same form as Equation 2.16. This resulted in a model of the GTD temperature (T^{Model}) at time *t*:

$$T_t^{Model} = T_0^{CTD} + (T_0^{GTD} - T_0^{CTD})\, e^{-\frac{t}{\varphi}} \tag{2.18}$$

The value for φ is calculated in a similar manner to the parameters in Equation 2.13 by minimizing the MSE between T_t^{GTD} and T_t^{Model} as followed in Equation 2.14.

The thermal response time introduced a lag between the internal GTD temperature (°C) and the surrounding water temperature as measured by the CTD. Starting with the ideal gas law, we relate the disequilibrium ΔT^{Dis} due to the lag between the CTD temperature and the GTD temperature to a disequilibrium ΔGT^{Dis} between the actual gas tension and the GTD reading:

$$\frac{GT_t^{GTD}}{(T_t^{CTD}+273.15)} = \frac{(GT_t^{GTD}+\Delta GT_t^{Dis})}{((T_t^{CTD}+273.15)+\Delta T_t^{Dis})} \tag{2.19}$$

This assumes both no net transfer of gas across membrane (constant *n*) and the volume of the GTD remains unchanged (constant *V*). Rearranging, we have an equation describing the gas tension disequilibrium as a function of the temperature disequilibrium:

$$\Delta GT_t^{Dis} = GT_t^{GTD}\frac{\Delta T_t^{Dis}}{(T_t^{CTD}+273.15)} \tag{2.20}$$

Since the temperature disequilibrium is a transient, its effect on the gas tension is also transient and dependent on the temperature equilibration timescale. So long as $\varphi \leq \tau$, we did not explicitly account for the transient when fitting the GTD observations, because the signal disappeared as the GTD reached gas tension equilibrium with the surrounding water. However, it is important to remain aware of this effect, as the specific configuration of the instrument on a platform may alter the thermal equilibration time.

The time series collected by the GTD required processing to arrive at a sample seawater gas tension. Initially, the water vapor is subtracted from the GTD time series. Then the dry GTD time series is deconvolved with the response time by inverting Equation 2.9. Next, the deconvolved time series is low-pass filtered. The filtered data is then averaged over each segment of the time

series that the GTD was held at the same isopycnal, which we labelled ‘drifts’. The result was a single measurement of the dissolved gas tension minus water vapor, referred to as dry gas tension, for each float drift.

2.3.2. Experimental Methods

2.3.2.1. Laboratory Methods

GTD performance, design limits, and membrane-properties were assessed in the laboratory with several experiments. In Experiment 1, two GTDs with Teflon-membranes (S/N 43 & 44) were placed in a large pressure test vessel (PTV) filled with freshwater at equilibrium with one standard atmosphere. Over 15 days the hydrostatic pressure was changed in increments of approximately 70 dbar up to a maximum of 300 dbar, with variability of ± 2.5 dbar. Each hydrostatic pressure was maintained for a minimum of 24 hours. Pumping was set at 50% cycle. Temperature, GTD barometric pressure, and hydrostatic pressure were recorded once per minute.

The collected time series were modeled using the model described by Equation 2.13. The effects of hydrostatic pressure, temperature, respiration on gas tension (via decreasing oxygen), along with the response times, were fit following Equation 2.14. Parameter standard errors are the diagonal of the covariance matrix (C), which is calculated following the equation $C = \sigma^2(J^T J)^{-1}$, where J is the Jacobian matrix. With the fitted model parameters, the gas tension time series were normalized following Equation 2.15. Each equilibration of the GTD, identified by discontinuities in the normalized time series, was fit using the simplified model in Equation 2.16 to investigate any effect of hydrostatic pressure on the response times of the GTD.

Another experiment assessed the operational hydrostatic pressure range of the Teflon membranes. Two Teflon-membranes and housings were placed in a PTV and the hydrostatic pressure slowly raised to 550 dbar. The membranes were held at 550 dbar for over 24 hours. This was followed by rapid cycling between ambient pressure (60 dbar) and 550 dbar in the PTV. The presence of water behind the membranes were tested for during the experiment using a syringe to evacuate the volume behind the dry-side of the membrane, which would indicate membrane failure or reverse osmosis.

Separately with Experiment 2, the Teflon-temperature dependence was assessed by measuring the equilibration time of the GTD from 5 – 30°C, a typical range for field measurements.

The GTDs were submerged in a containment vessel filled with atmospheric-equilibrated freshwater. The containment vessel is placed within a temperature-controlled water bath. Addition of degassed water (by boiling for > 10 minutes and cooling while sealed from the atmosphere) induced a step-change in the gas tension. Gas tension and temperature were recorded once every 30 seconds. The GTDs equilibrated for a minimum of five e-folding times, and the resulting curves fit to estimate the effect of temperature on response times.

2.3.2.2. Site Descriptions and Field Methods

Initial field-testing in seawater occurred off Shilshole, Seattle, Washington, in the Puget Sound April 16th – 20th 2014 aboard the UW/APL vessel *R/V Robertson*. Two UW/APL Gas Floats #77 and #78 (F77 & F78) were respectively equipped with pumped GTDs #44 and #43 (GTD#44 & GTD#43). First, the floats were attached to a stand and lowered by crane to set depths off the side of the ship. This was followed by a series of untethered calibration dives between the surface, 140 dbar, and 70 dbar. Discrete water samples were collected at 5 meter increments bracketing the calibration depths of the GTDs.

The two UW/APL Gas-Profiling Floats F77 and F78 equipped with pumped GTDs, along with a prototype un-pumped GTD-equipped Argo float (GTD-Argo), were deployed from the *R/V New Horizon* in the ETNP as part of the *NH1410* research cruise. In May 2014, the floats were placed in the ocean approximately 2 kilometers apart at 20.08°N 107.07°W for cross-calibration of the instrumentation, and subsequently drifted northwest over the course of the 15-day deployment.

During initial deployment, both floats performed a series of calibration profiles with concurrent CTD casts. Niskin bottles at the calibration pressures were collected for N_2:Ar measurements and Winkler titrations. The float profiles targeted predetermined isopycnals by adjusting their density to be neutrally buoyant. A profile consisted of an initial dive to a max density, followed by a series of drifts at decreasing densities in the water column. Each float drift lasted 2-3 hours, sufficient time for the GTD to fully equilibrate. Float 77 was recovered during initial deployment due to a malfunction and redeployed for four days at the end of *NH1410*.

2.3.2.3. Standard Reference Methods

Gas tension measurements by the GTD were validated against a gas tension estimate calculated from independent dissolved gas concentration measurements of N_2, O_2, and Ar. The SeaBird 43 and Anderaa optode dissolved oxygen data were calibrated using in situ Winkler titration measurements. N_2:Ar ratios were measured by the Isotope Biogeochemistry Group (School of Marine Science and Technology, University of Massachusetts-Dartmouth). Puget Sound N_2:Ar and O_2:Ar ratios were measured from discrete bottle samples in the lab at UMass-Dartmouth by Isotope-Ratio Mass Spectrometry [Charoenpong et al. 2014]. ETNP N_2:Ar ratios were sampled at sea via Quadrupole Mass Spectrometry.

ETNP background argon concentrations are provided by Clara Fuchsman, which were collected as an onshore-offshore transect from 18.39°N 104.99°W to 14.00°N 110.00° in the ETNP in 2012 as part of a separate project (Fuchsman et al 2017). Argon concentrations were measured by isotope dilution (Hamme and Emerson 2004b). Then, we developed and used a linear-mixing-model based on T-S analysis to interpolate the ETNP 2012 argon concentration data to our observations.

To derive an independent gas tension for validating the GTD in the OMZ, first the measured N_2:Ar ratios were multiplied by the interpolated background argon concentrations to calculate the nitrogen concentrations. Next the nitrogen and argon concentration were converted to partial pressures using Henry's Law including the literature hydrostatic pressure dependence of 14% 1000 $dbar^{-1}$ [Enns et al. 1964; Ludwig & MacDonald 2005]. Water vapor pressure was explicitly calculated assuming 100% saturation. The pCO_2 was taken from climatology (≈1.4 mbar in the ETNP OMZ) [Boyer et al. 2013]. Typical concentrations of the remaining trace gases contributions fall below the instrument noise level and thus are considered negligible.

2.4. RESULTS

2.4.1. Laboratory Characterization

In the laboratory, the two GTDs measured ±0.2 mbar of each other (Figure 2.2, note the timeseries are purposefully offset for clarity of presentation). Temperature varied between 20 – 22°C. Using Equation 2.14 best-fit values for $\tau, \alpha, \beta,$ and $Q,$ are shown in Table 2.2. The modeled

time series calculated using Equation 2.16 and the results in Table 2.2 compared with the collected time series have standard deviations of 1.87 and 1.25 mbar (≈0.2%) for GTD#43 and GTD#44, respectively (Figure 2.2). Note that the lab response times are smaller ($\tau \cong 20$ min) than the response time for the field deployments ($\tau \cong 36$ min) because the field-deployed GTD was pulse-pumped. Applying Equation 2.15 to normalize the gas tension time series, the response times calculated with Equation 2.16 range from 26.8 min to 48.8 min (Figure 2.3), independent of hydrostatic pressure. The response times for GTD#43 increased over time. The cause of the difference between the modeled and the individually-fit response times is currently unknown.

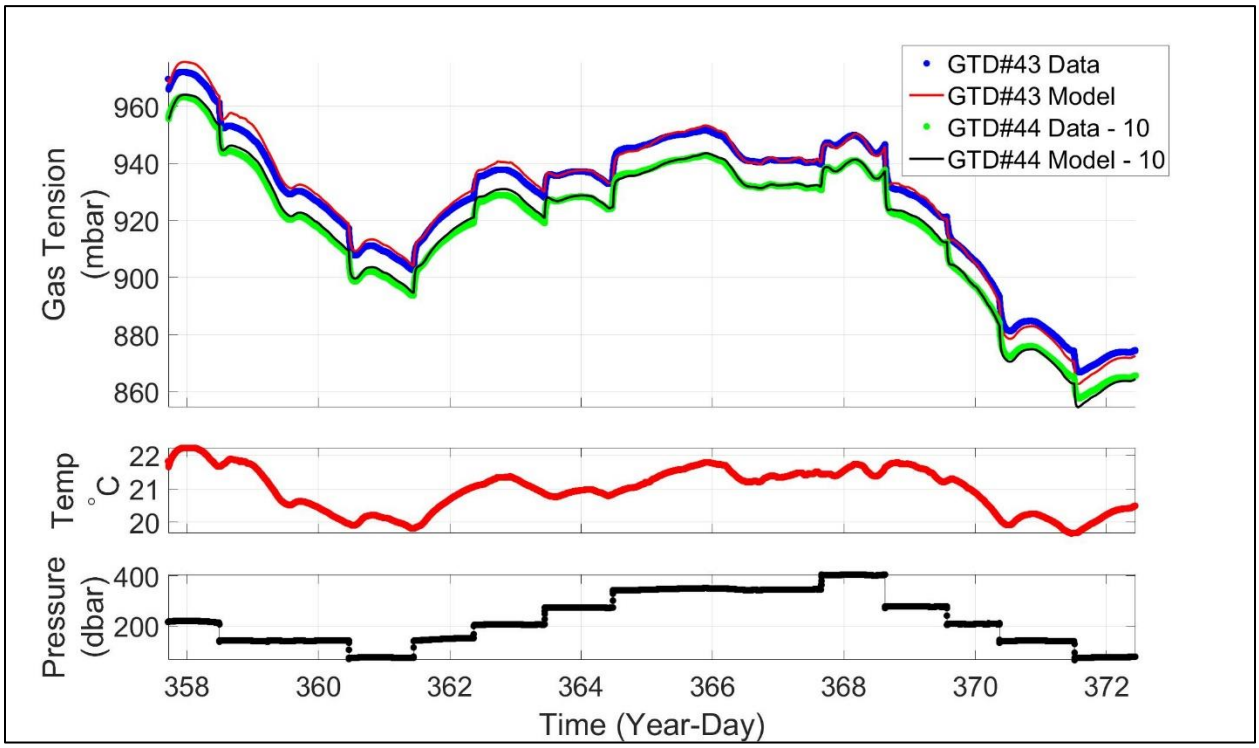

Figure 2.2. Results of lab experiment 1 - The model described by Equation 2.13 successfully recreates the observed gas tension time series to within ±1.87 (GTD#43) and ±1.25 mbar (GTD#44) using the best fit parameters (Table 2.2) calculated following Equation 2.14. Note the GTD#44 data and model is offset by 10 mbar for both time series to be visible.

Table 2.2. Lab experiment 1 - Model parameter best-fit values and standard errors trained on the laboratory gas tension time series from the first laboratory experiment. Data collected with 50% pumping. Response time τ is assumed independent of hydrostatic pressure and temperature.

Parameter ± SE	GTD#43	GTD#44
τ (min)	21.36 ± 0.30	20.22 ± 0.34
α (%/°C)	1.67 ± 0.03	1.63 ± 0.02
β (%/1000 dbar)	12.78 ± 0.2	12.98 ± 0.14
Q (mbar/min)	$-2.70*10^{-3} \pm 2.31*10^{-6}$	$-2.60*10^{-3} \pm 1.41*10^{-6}$
GT σ (mbar)	± 1.87	± 1.25

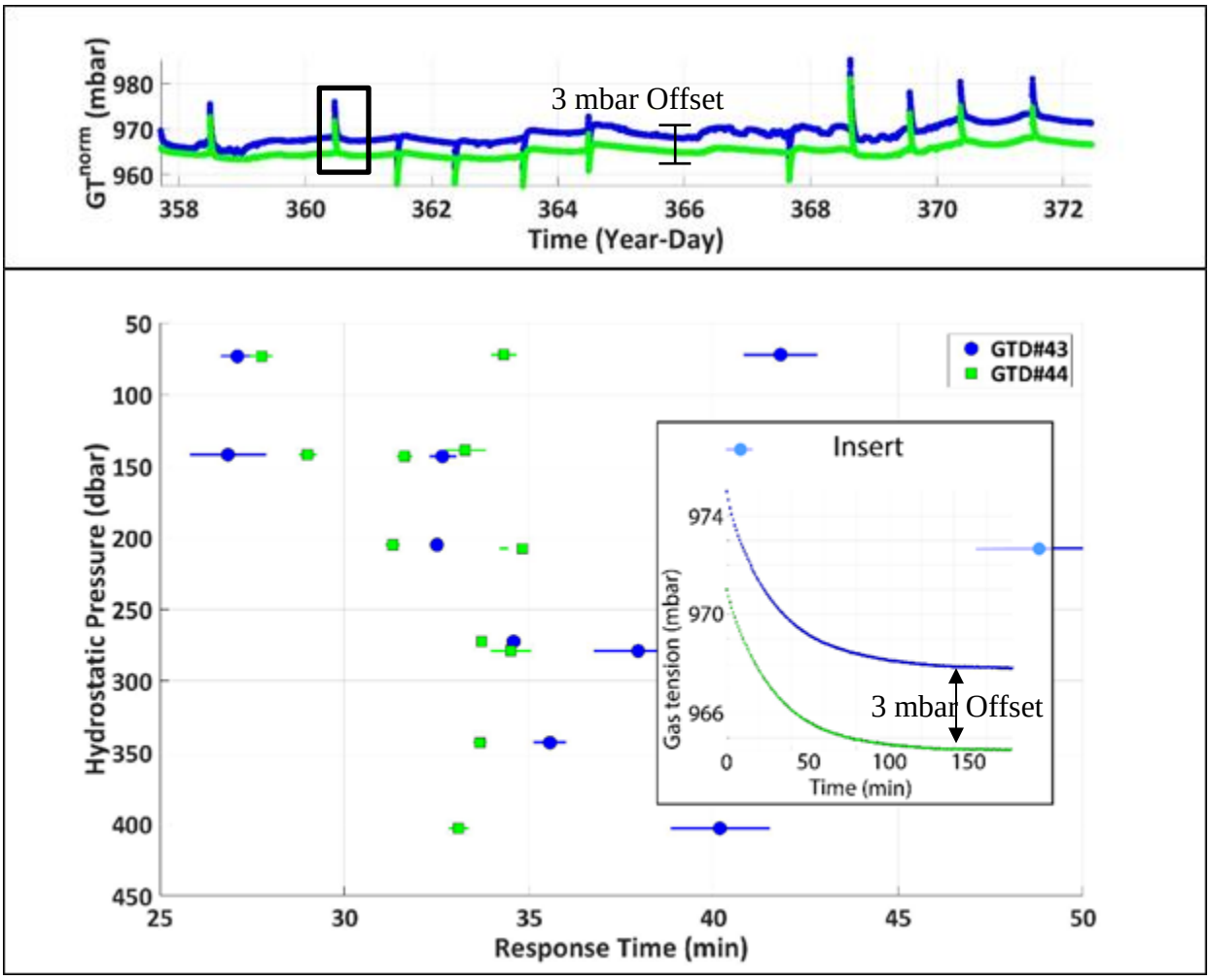

Figure 2.2. Results of lab experiment 1 - Top: The normalized gas tension time series corrects for the effects of temperature, hydrostatic pressure, and biology, using the best fit parameters from Table 2.2. Each discontinuity in the normalized gas tension time series occurs at a change in hydrostatic pressure, when the GTDs re-equilibrate. The highlighted box represents the insert below. A 3 mbar offset is applied to the GTD#44 time series to make the time series visible. Bottom: GTD#43 (blue circles) and GTD#44 (green squares) response times are independent of hydrostatic pressure, a significant advance over previous GTD versions. An individual response time is calculated by fitting a curve to a GTD equilibration (insert, curves offset by 3 mbar). Data collected with 50%-pumping. Response times for GTD#43 increased over time (print: color)

Response times for an atmospheric mixture of dissolved gases showed an inverse linear relationship with temperature (Figure 2.4), decreasing from 17.4 ± 1.8 min at 5.3°C to 13.0 ± 1.2

min at 29.9°C. Calculated exponential constant was 7.7 ± 2.2 kJ/mol. Literature comparisons were 4.6 (N_2) and 3.4 (O_2) kJ/mol for Teflon-AF 2400 [Alentiev et al. 2002].

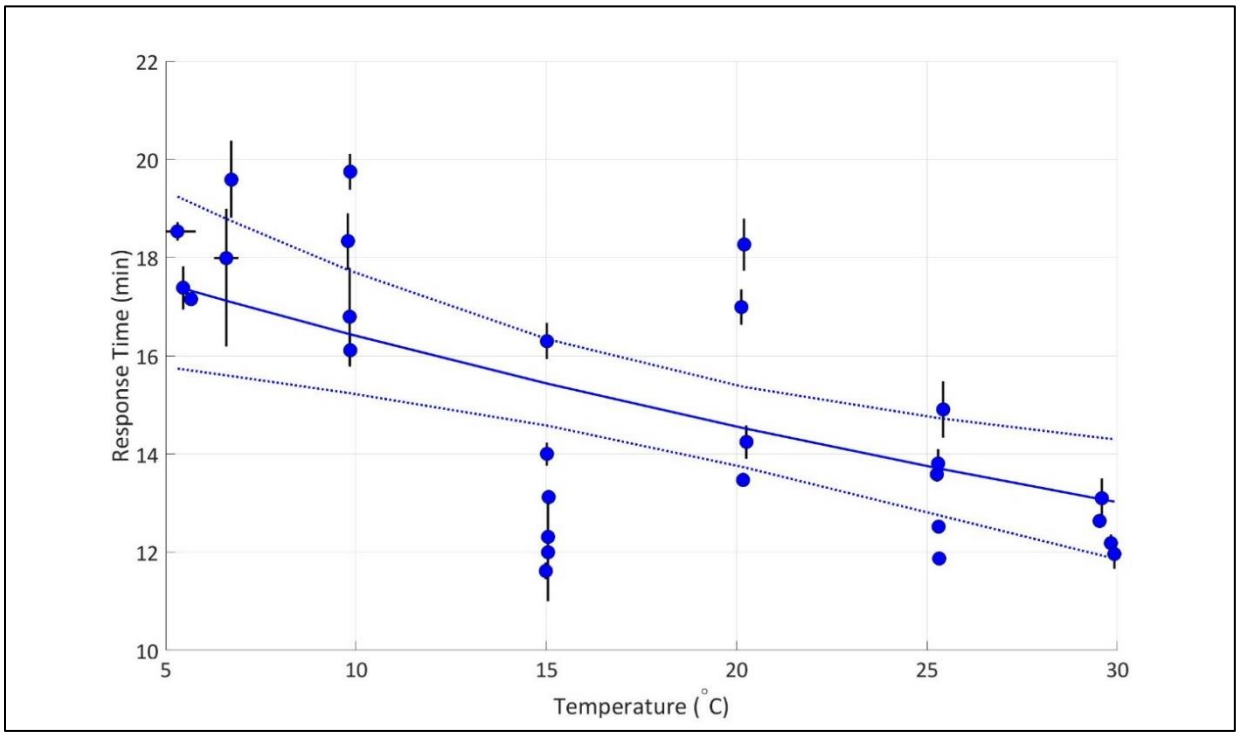

Figure 2.3. Results of lab experiment 2 - Continuously-pumped response times of the Teflon-membrane mounted in GTD#43 are inversely dependent on temperature. The dependence and 95% confidence intervals are fit following Equation 2.12. Note that the thermal response time for a pulse-pumped system will be larger.

2.4.2. Puget Sound

Gas tension was successfully recorded only by GTD#44 mounted on Float 77 (GTD#43 did not record properly) (Figure 2.5). Both GTDs successfully recorded internal temperatures. The seawater temperature ranged from 10.4°C at the surface to 8.0°C at 140 dbar. Salinity varied from 27.77 psu at the surface to 29.72 psu at 140 dbar. Thermal equilibration times (ϕ) were 21.4 ± 7.0 min and 28.2 ± 4.8 min for GTD43 and GTD44, respectively. Response times with pulse-pumping (10 %) averaged τ = 36 minutes, which is still larger than the thermal response time. Argon was calculated from the O_2:Ar and SBE43 oxygen concentrations. Estimated gas tension agrees, to within 2 – 4 mbar (0.2% - 0.4%), with the independent IRMS N_2:Ar and O_2:Ar gas tension (Figure 2.6).

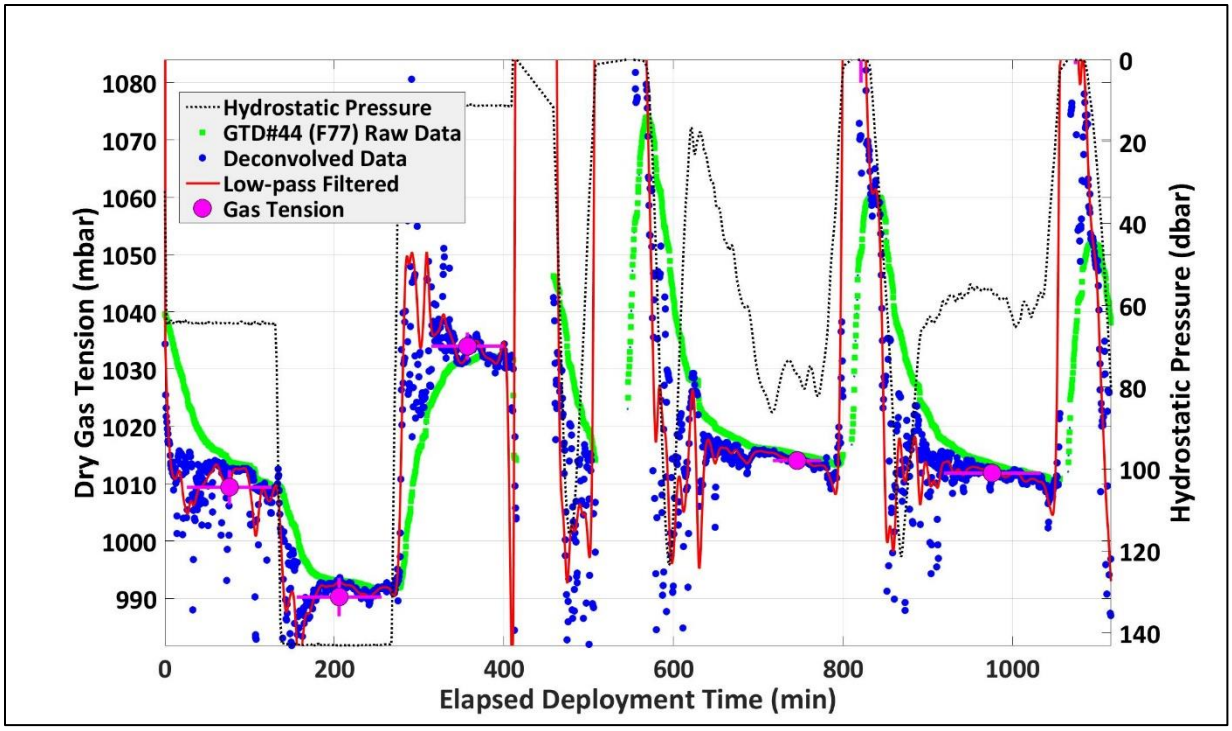

Figure 2.4. Successful measurements of gas tension in the Puget Sound by GTD#44 on Float 77. The procedure deriving the gas tension from the collected raw data is demonstrated. The raw data from GTD#44 on Float 77 (green squares) is deconvolved (blue circles) with a pulse-pumping response time τ = 36 minutes, and low-pass filtered (red line), which is averaged over a constant hydrostatic pressure (black lines) to arrive at the gas tension measurement (magneta circles). Floats were attached to the ship winch before the 500 minute mark and freely profiling after. (print: color)

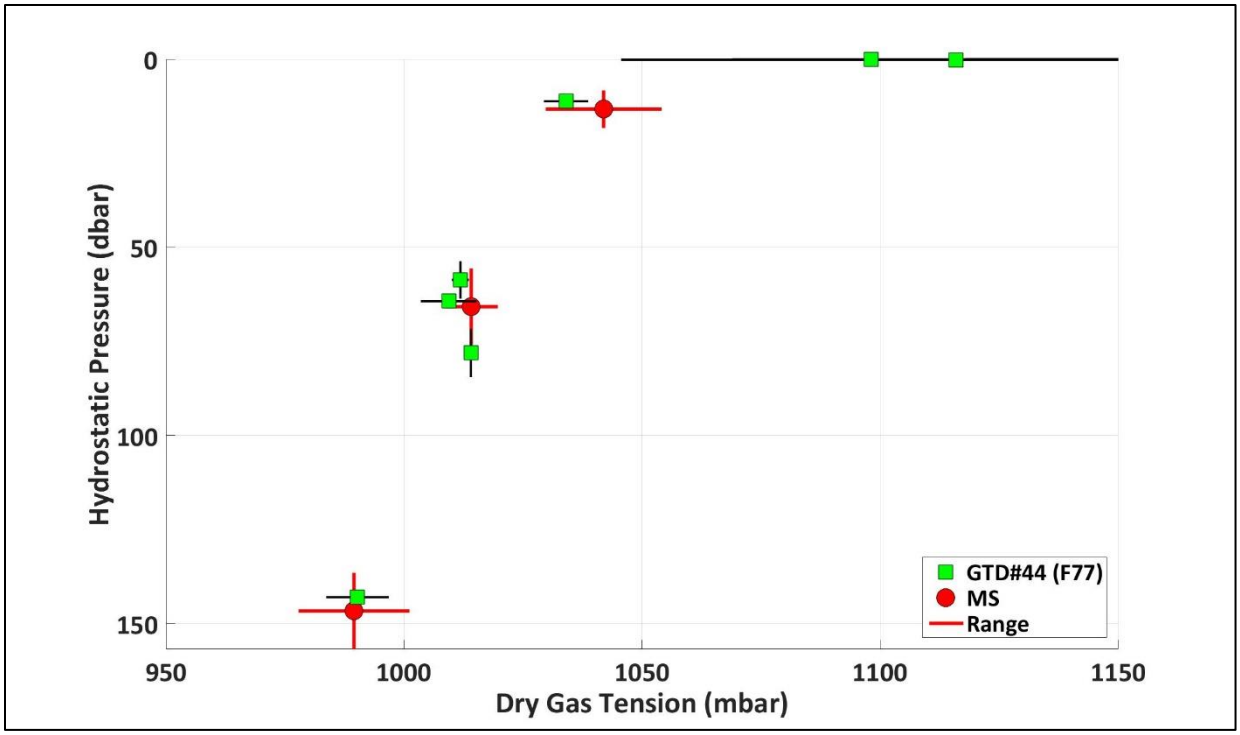

Figure 2.5. GTD#44 on Float 77 successfully measured gas tension throughout the water column in the Puget Sound, whether the sensor was tethered or freely drifting. The mass spectrometry (MS) data points show the target range of measured gas tension. The GTD agrees within 2 – 4 mbar (0.2 – 0.4%).

2.4.3. Eastern Tropical North Pacific

The oxycline, where oxygen rapidly decreases from saturation to anoxia, was located at approximately 50 – 70 dbar in the water column. Gas tension decreased from approximately atmospheric at the surface to a local minimum just below the oxycline, then a small local maximum, and then an absolute minimum of 836 mbar at 127 dbar (Figure 2.7). Below the absolute minimum the gas tension increases with depth. Both GTDs operated without displaying any behavior indicative of a blockage as occurred in the Puget Sound. The Argo float successfully equilibrated and measured gas tension twice during separate 12-hour drifts. The GTDs did not fully equilibrate at the surface due to the profiling schedule set for the floats.

Gas tension from Float 77 is approximately 7 mbar higher than gas tension from Float 78 throughout the anoxic portion of the water column without any dependence on hydrostatic pressure or temperature (Figure 2.7). Argo float measurements are approximately 3 mbar higher than the

Float 77 measurements. Measured gas tension agrees to within error with the calibration gas tension (Figure 2.8).

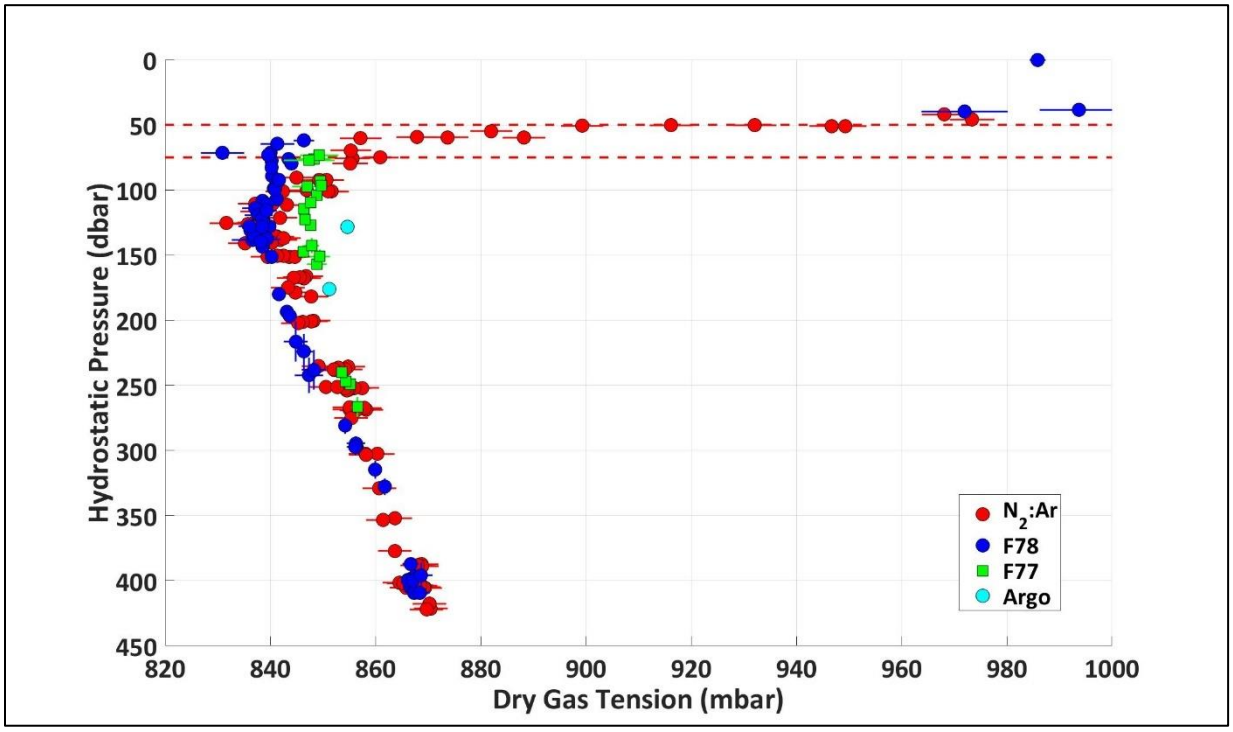

Figure 2.6. Gas tension within the anoxic portion of the water column was successfully measured to within ±3.13 mbar of the N_2:Ar-derived validation gas tension in the ETNP ODZ. The oxycline, located from approximately 50 – 70 dbar and identified with the two red lines, is where the oxygen concentrations decline from saturation to sub-micromolar (< 1 µM/kg) concentrations. The GTD on Float 77 measures approximately 7 mbar higher than Float 78 within the anoxic portion of the water column. The GTDs were pulse-pumped and floats freely-drifting. The Argo float is unpumped. (print: color)

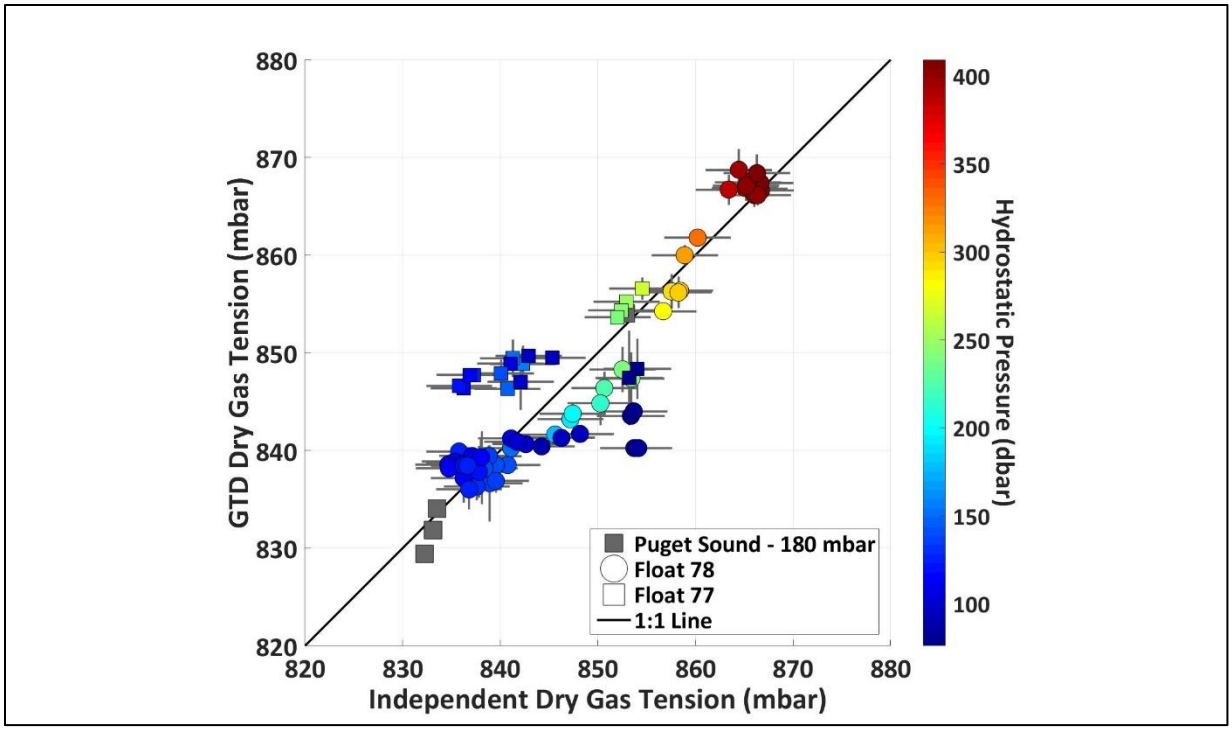

Figure 2.7. Validation that we successfully measured gas tension using the GTDs in the ETNP ODZ. The gas tension measured by the GTD (y-axis) generally agrees within error with the independent gas tension derived from the N2:Ar measurements (x-axis). Puget Sound (grey squares) are adjusted 180 mbar to fit on scale. Hydrostatic pressure of the measurements shown with a linear color scale. (print: color)

2.4.4. Sources of Error

Changes in temperature and hydrostatic pressure not only alter the gas tension in the water but may also affect how well the GTDs operate. Under the tightly controlled conditions of the laboratory PTV, GTD#43 and GTD#44 measure to within ±0.2 mbar of each other. Model characterization describes the GTD response to ±2.13 (GTD#43) and ±1.32 mbar (GTD#44).

In the Puget Sound and ETNP, uncertainty in determining the end-point equilibrated gas tension is affected by the background geophysical noise. The uncertainties following deconvolution and low-pass filtering, which are calculated by taking the standard deviation of the 15 minutes after full equilibration of the low-pass filtered data, average ± 1.29 mbar (0.15%) and ± 1.44 mbar (0.17%) for GTD#44 (Float 77) and GTD#43 (Float 78), respectively. Geophysical noise is comprised of physical processes, such as internal waves, which alter in-situ gas tension

and temperature faster than the GTD can equilibrate, introducing high-frequency variability. The high-frequency variability is further amplified by applying the deconvolution procedure.

Assessment of the accuracy of the GTD gas tension is influenced by how well we can independently determine the gas tension in the water column from the N_2:Ar and O_2 measurements. The N_2:Ar measurements themselves have a precision of 0.23‰ [Charoenpong et al. 2014]. Seabird and optode oxygen errors are ≈2 µM/kg with respect to Winkler titrations. However, the oxygen errors only contribute to uncertainty within the oxycline and surface; in the anoxic portion of the water column, oxygen is below 100 nM and its contribution to the total uncertainty is negligible [Tiano et al. 2014]. Interpolation of the argon concentrations measured by Fuchsman et al [2017] has an uncertainty of 0.03 µM/kg, which with solubility uncertainty of 0.13% results in an average *pAr* uncertainty of 0.03 mbar (0.26%) [Hamme & Emerson 2004]. Propagation of the argon uncertainty when calculating the nitrogen concentrations from N_2:Ar is the dominant source of the uncertainty in the final pN_2 of 3.15 mbar (0.31%). The total uncertainty amounts to 3.42 mbar (0.40%), of which 92% is attributed to uncertainty on pN_2, 7.8% to pO_2, and 0.2% to *pAr*. The final uncertainties are 15 – 30% the size of the signal we aim to resolve.

Final accuracy of the GTDs, assessed by comparison of the GTD gas tension with the independent gas tension calculated from the N_2:Ar measurements, are 0.6% (GTD#44; Float 77) and 0.4% (GTD#43; Float 78; refer to Figure 2.8). We take this as a conservative error estimate, since at this time cannot claim that the differences are due to a systematic bias rather than random error and uncertainty.

2.5. DISCUSSION

GTD#43 on Float 78 successfully measured gas tension in the ETNP ODZ to within 0.40%. This compares favorably with the error estimate of 0.7% on previous GTD versions [McNeil et al. 1995]. The cause of the 7-mbar offset of GTD#44 relative to GTD#43 cannot yet be determined. The two barometers measured less than 0.2 mbar difference in pre-and-post cruise calibrations. Additionally, the difference between the two deployed GTDs is constant throughout the water column, and shows no change with depth or temperature. However, this does suggest we successfully characterized the effects of changing temperature and hydrostatic pressure on the GTDs. Additionally, our final uncertainties are about 15-30% of the expected 10 - 20 mbar N_2

signal produced by denitrification in the ETNP, which is the primary motivation for this sensor development. Thus, these GTDs are sufficiently precise to separate a small 20 mbar signal from a large 850 mbar signal.

Our descriptive model estimates the Henry's Law pressure dependence as 12.8 ± 0.3% per 1000 dbar. This is lower than the limited literature estimates of 14% per 1000 dbar. Additionally, we fit a simple linear regression of gas tension vs hydrostatic pressure from the gas tension minimum to the maximum depth measured, spanning 300 dbar. The fit yielded a 13.2 ± 2.8% increase per 1000 dbar. This agrees with the literature values, but glosses over any non-hydrostatic pressure effects which alter gas tension in the OMZ [Klots 1961; Enns et al. 1964; Ludwig & Macdonald 2005].

The estimates of the hydrostatic pressure effect and equilibration times are complicated by confounding factors not explicitly controlled. In the lab, changes in hydrostatic pressure are altered using a secondary steel overflow tank with a bladder that forces water into or accepts water from the main tank. The water within the secondary tank was rapidly reduced via oxidation of the steel tank. Thus, changes in hydrostatic pressure create instantaneous jumps in dissolved oxygen that are not readily quantifiable. Biology and rust products may also alter flow of or physically coat the membrane from the water, impeding gas exchange and equilibration. This complicates and introduces error to the interpretation of the hydrostatic pressure effect on gas tension in the lab. It also adds variability when calculating the equilibration times from the individual curve fits, because equilibration is dependent on renewal of the water-side membrane boundary layer. Additionally, we suspect that these processes disproportionately affected GTD#43 in the PTV over GTD#44 because GTD#43 response times increased over time. We are unsure why GTD#43 was affected, but suspect its placement in the PTV relative to the overflow tank and pressurization bladder was important.

In the ETNP ODZ, active nitrogen loss processes such as denitrification and anammox actively alter the dissolved nitrogen levels [Gruber & Sarmiento 1997; Paulmier & Ruiz-Pino 2008; Chang et al. 2012]. Knowing the effect of hydrostatic pressure on gas solubility is necessary to accurately calculate the nitrogen concentrations from the gas tension measurements. Similarly, both the Anderaa Oxygen Optode and SBE43 oxygen sensor functionally measure the partial pressure of oxygen, not the concentration [Demas et al. 1999; Carlson 2002]. Although both oxygen sensors have confounding hydrostatic pressure effects, they are calibrated to the surface

solubility [Uchida et al. 2008; McNeil & D'Asaro 2014]. This led us to utilize the literature value of 14% 1000 $dbar^{-1}$ for our calculations. Consequently, we aim to further refine the hydrostatic pressure effect on gas tension by future experimentation utilizing the new GTD.

Gas tension sampling was not flawless. There was an apparent internal blockage in GTD#44 during field testing in the Puget Sound. While the source of the blockage is not yet certain, we suspect condensation of water vapor on internal piping due to rapid profiling because the floats were tethered to the ship winch. This should not be an issue when the floats profile autonomously by adjusting their buoyancy, since it results in a much slower ascent and descent rates. Indeed, we observed no blockages in the ETNP. Additionally, membrane diffusion coefficients change by ≈28.5% over the operational temperature range of the GTD. However, the response of $\tau(T)$ is linear and is simple to adjust needed response times based on water temperature.

2.6. CONCLUSIONS

The new Teflon-membrane GTD offers a compact, stable method for in-situ determination of dissolved gases. It eliminates, or at the least minimizes, many of the complications of the previous PDMS-membrane version: the response time is independent of hydrostatic pressure, there is no apparent reverse-osmosis, and it functions uniformly throughout operational water depths. We demonstrate that two GTDs successfully measured to within an error of 0.4% and 0.6% the gas tension in the ETNP ODZ. Additionally, we showed that a GTD can equilibrate and measure gas tension on an Argo-float. Using previously published methods for determining dissolved nitrogen from measured gas tension, the new GTD opens up the possibility for in-situ investigation of denitrification within pelagic ODZs [McNeil et al. 2005; McNeil et al. 2006a]. An additional advantage to this version of the float-mounted GTD is it is significantly more compact than the previous PDMS-version. Further reduction in response time should be possible using a pressure sensor with a very small internal volume. A faster response time should also reduce the uncertainty due to geophysical noise.

We envision a variety of future applications for our new GTD. Its compact size and low-power makes it an ideal candidate to be incorporated onto biogeochemical-Argo-floats for long term in-situ studies of denitrification in ODZs, air-sea gas exchange, and net community

production in the surface ocean. Continuing improvements in shrinking the size and response time are also targeted at future incorporation onto CTDs as part of the standard instrument package. Our goal is to make gas tension measurements and dissolved-N_2 gas a regularly collected parameter, alongside T, S, and O_2.

Chapter 3. A NEW METHOD FOR MEASURING BIOGENIC-N_2 IN OXYGEN DEFICIENT ZONES FROM GAS TENSION

Andrew Reed[a,b,*], Craig McNeil[b], Mark Altabet[c], Eric D'Asaro[b], Annie Bourbonnais[c]

[a]School of Oceanography, University of Washington, 1503 NE Boat Street, Box 357940, Seattle, WA 98195, USA

[b]Applied Physics Laboratory, University of Washington, 1013 NE 40th Street, Seattle, WA 98105, USA

[c]School for Marine Science and Technology, University of Massachusetts Dartmouth, 706 Rodney French Blvd, New Bedford, MA 02744, USA

3.1. INTRODUCTION

Oxygen Deficient Zones (ODZs), regions of the ocean where oxygen drops to sub-micromolar concentrations, are important environments for the global nitrogen cycle as an oceanic sink of biologically-available nitrogen-species [Paulmier & Ruis-Pino 2008]. In the absence of oxygen, a diverse group of microbes including eukaryotes, bacteria, and archaea, utilize nitrate (NO_3^-) as the electron receptor to respire organic matter [Brandes et al 2007]. The step-wise reduction of NO_3^- to N_2 to respire organic carbon is known of denitrification. Additionally, anammox, the oxidation of ammonia (NH_4^+) coupled to nitrite reduction (NO_2^-), is used by certain archaea to fix carbon in ODZs [Devol 2003; Thamdrup et al 2006]. These processes result in the biologically-mediated production of N_2 gas, known as biogenic N_2, within the ODZ's water column.

The source waters for the Eastern Tropical North Pacific (ETNP) ODZ is principally comprised of modified 13°C Thermostad water and identifiable as a subsurface salinity maximum north of 10°N [Sloyan et al. 2003; Fiedler and Talley 2004]. This water mass forms as high-salinity surface waters in western tropical pacific, is transported eastward within the northern subsurface countercurrent (NSCC), and turns northward east of 100°W [Tsuchiya & Talley 1996; Kessler

2006]. During transit, there are strong diapycnal fluxes between the 13°C water and the deeper, fresher, underlying North Pacific Intermediate Water. Another defining characteristic of the 13°C water in the eastern tropical Pacific is that it cannot be aged using standard tracer approaches, which indicates sluggish ventilation [Warner et al 1996]. Consequently, the source waters of the ODZ are significantly modified by the time they reach the ETNP.

Biogenic-N_2 gas within the ETNP ODZ accumulates as a small signal atop a significantly larger background dissolved-N_2 gas (abiotic) signal (up to 20 µM/kg biogenic-N_2 vs ≈500 µM/kg abiotic-N_2) [Bourbonnais et al., 2015]. The abiotic-N_2, analogous to preformed nutrients, is initially set by air-sea gas exchange. Bubble injection processes during water mass formation and subsequent mixing and warming of the ODZ source waters after formation results in departures from equilibrium (i.e. physically-induced supersaturations) when the source waters arrive in the ODZ region. Figure 3.1 give a schematic of the expected N_2 saturations both inside and outside the ODZ. Consequently, measured N_2-supersaturations are a combination of abiotic and biogenic-N_2 contributions. Of the supersaturated N_2, approximately ⅓ – ½ may be biogenic in origin [Chang et al., 2010]. Thus, accurate assessment of the biogenic-N_2 requires either knowledge of the N_2 concentrations in the ODZ source waters or a proxy for the abiotic supersaturated N_2, in either the ODZ or the source waters, such as the Ar saturation.

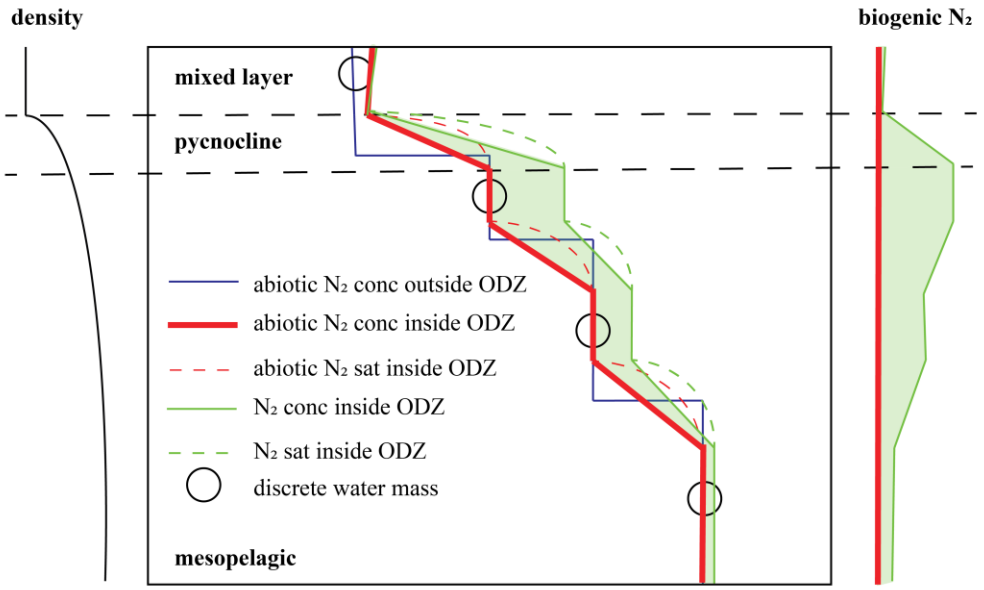

Figure 3.1. Schematic of the mixing between discrete water masses and the relative contributions of abiotic and biogenic-N_2 in the ETNP ODZ. Initial N_2 concentrations (black lines), set by air-sea gas exchange in the water masses where their isopycnals outcrop, mix with each other to yield an abiotic-N_2 concentration line (red line). Non-linearity of solubility leads to apparent supersaturations of the abiotic N_2 when mixing. Once in the ODZ, biogenic-N_2 is produced and accumulates on top of the abiotic-N_2 signal.

Two approaches to measuring biogenic-N_2 are commonly used. The first approach is nutrients-based and calculates the difference between the observed DIN (DIN = $[NO_3^-]$ + $[NO_2^-]$ + $[NH_4^+]$) within the ODZ (N_{ODZ}) and the DIN expected:

$$N_{2,bio} = \left(N_{exp} - N_{ODZ}\right) \times 0.5 \qquad (3.1)$$

This loss of DIN is assumed to be converted to N_2 gas by denitrification and annamox processes. The nutrients-based method averages denitrification rates over time and space; however, it is dependent on a constant Redfield remineralization ratio of organic matter in the ODZ. Consequently, it potentially ignores other sources of nitrogen in the ODZ, particularly where the ODZ contacts sediments, and therefore may introduce uncertainty in the estimates [Lam et al 2008; Lam & Kuypers 2011].

The second approach involves dissolved gases, rather than nutrients, using the ratio of nitrogen-to-oxygen (N_2:Ar) in seawater measured by mass spectrometry [Devol 2006; Chang et al

2010, 2012]. This method offers the advantage of directly measuring the dissolved gases in the water column with precisions exceeding 0.03% [Groffman et al 2006; Charoenpong et al. 2014]. However, successfully determining biogenic-N_2 from total measured N2 requires some means to separate the biologically produced N_2 from N_2 that originated from physical processes, such as air-sea gas exchange and mixing. For this we use argon (Ar), which is inert and therefore oceanic Ar distributions are subject only to physical processes. Since mass spectrometry easily and precisely measures N_2:Ar ratios, we compare measured N_2:Ar within the ODZ $(N_2{:}\,Ar)_{ODZ}$ with a N_2:Ar profile sampled from outside the ODZ $(N_2{:}\,Ar)_{abiotic}$ to provide information on the biogenic-N_2 as:

$$[N_2]_{bio} = \left[\frac{(N_2{:}Ar)_{ODZ}}{(N_2{:}Ar)_{eq}} - \frac{(N_2{:}Ar)_{abiotic}}{(N_2{:}Ar)_{eq}}\right] * [N_2]_{eq} \qquad (3.2)$$

where both values are normalized by the ratio $(N_2{:}\,Ar)_{eq}$ defined for seawater in equilibrium with the atmosphere.

The goal of this study is to demonstrate a third, and new, method for measuring biogenic-N_2 in ODZs that uses gas tension measurements. Gas tension, measured by a gas tension device (GTD), along with concurrent sampling of dissolved O_2, temperature, and salinity, have previously been used to measure N_2 in the upper 100 m of the water column with an accuracy of ±0.7% [McNeil et al 2006a]. Time series of GTD-derived N_2 were used to calculate net community production, estimate air-sea gas exchange rates, study the importance of bubbles on mixed layer gas supersaturations, and estimate denitrification in the Baltic Sea [McNeil et al 1995; McNeil et al 2006b; McNeil & D'Asaro 2007; D'Asaro & McNeil 2007; Löffler et al 2014]. Recent improvements to the sensors extend the GTD's operational range to 1000 meters [Reed et al. – in press]. This development makes it possible to sample the gas tension to an accuracy of ±0.6% within open ocean ODZ core waters, located at depths of 100-1000m.

Below, we first outline how to calculate N_2 from gas tension measurements. Then, we examine how different assumptions for dissolved Ar levels affect the calculation of dissolved N_2 from both the gas tension and N_2:Ar measurements. Then, based on T-S analysis of the observations we show how to develop and apply a conservative linear-mixing model that provides significantly improved estimates of Ar and N_2 supersaturations in the ODZ associated with physical processes. Lastly, we show how to calculate biogenic-N_2 from the gas tension derived N_2

and compare this estimate with similarly calculated values from both N_2:Ar ratios measured by mass spectrometry measurements and from dissolved inorganic nitrogen.

3.2. METHODS & SAMPLING PROCEDURES

3.2.1. N_2 from Gas Tension

Our approach does not directly measure dissolved N_2. Rather, GTDs measure the gas tension of seawater, which is the sum of the partial pressures of all the gases dissolved in seawater [McNeil et al 1995]. In a GTD a semipermeable membrane is used to equilibrate a small volume of gas trapped behind the membrane with the gases dissolved in the surrounding water. When the GTD's gas volume is equilibrated with the seawater sample, a barometer in the GTD measures gas tension [Reed et al. – in press]. The partial pressure of N_2 (P_{N_2}) is calculated by subtracting the partial pressures of the other major dissolved gases (argon - P_{Ar}, water vapor - P_{H_2O}, carbon dioxide - P_{CO_2}, and trace gases - P_{Trace}) from the gas tension (GT):

$$P_{N_2} = GT - P_{O_2} - P_{Ar} - P_{H_2O} - P_{CO_2} - P_{Trace} \quad (3.3)$$

N_2 dissolved in seawater is determined by the equilibrium between the partial pressure and the dissolved concentration [C_{N_2}]. This relationship is expressed by:

$$[C_{N_2}] = P_{N_2} * Sol_{N_2}(T, S, P_H) \quad (3.4)$$

where $Sol_{N_2}(T, S, P_H)$ is the Henry's Law solubility for N_2 at a given temperature *T*, salinity *S*, and hydrostatic pressure P_H. Holding concentrations constant, the partial pressure of N_2 (and argon) increases by approximately 14%/1000 dbar [Ludwig & MacDonald 2005]. See Reed et al. [in press] for a more detailed discussion of the hydrostatic pressure dependence.

Following Equation 3.4, to use gas tension for N_2-measurements we need to know the partial pressures of other major dissolved gases. After N_2, O_2 is the second most common dissolved gas in seawater. Oxygen is directly measured by numerous different methods (SeaBird 43 oxygen sensors, Anderaa oxygen optodes, Winkler titrations) with maximum accuracy of 0.1% (±0.3 µM/kg) and a precision of ±0.15 µM/kg [Langdon 2010]. However, within ODZs oxygen decreases to less than 1 µM/kg [Tiano et al. 2014] which is below the detection limits of these methods. Consequently, we assume these waters are anoxic. Water vapor pressure (pH_2O) is assumed to be 100% saturated [Reed et al. – in press] for gas tension calculations because the

membrane on the GTD is highly permeably to water vapor [Bernardo et al. 2009]. Carbon dioxide partial pressure is taken from climatology as pCO_2 = 1.4 mbar [Boyer et al. 2013]. The remaining trace gases are less than 0.01% of gas tension and their contribution to gas tension is smaller than the sampling error in gas tension [Reed et al. – in press].

3.2.2. Argon Assumptions

After oxygen and water vapor, most significant remaining gas of seawater gas tension that is not our desired measurement of N_2 is argon. It is a biologically inert gas with no internal sources or sinks in the ocean, and concentrations are set by air-sea gas exchange where waters equilibrate with the atmosphere at isopycnals outcrops when the water masses were formed. Measuring absolute argon concentrations in the absence of O_2 using mass spectrometry requires an analytically challenging technique called isotope dilution [Hamme & Emerson 2004b]. Consequently, Ar concentrations are typically derived from concurrent sampling of N_2:Ar and O_2:Ar ratios with supporting absolute oxygen concentrations from Winkler titrations. However, the absence of oxygen in the ODZ necessitates making assumptions about the background argon concentrations because we cannot calculate Ar from [O_2] and O_2:Ar.

Instead, we apply four different assumptions to estimate the concentration and partial pressure of argon. **Assumption 1** set argon as 100% saturated throughout the water column. **Assumption 2** follows the methodology of McNeil et al [2005] by setting the argon saturation as equal to the N_2 saturation. This then allows us to calculate the partial pressure of N_2 as:

$$pN_2 = \frac{GT - pH_2O - pO_2}{\left(1 + \frac{1 - \chi_{N_2} - \chi_{O_2} - \chi_{CO_2}}{\chi_{N_2}}\right)} \tag{3.5}$$

This assumption seems to some extent inconsistent or at worst case contradictory when applied to estimate biogenic-N_2, since we expect N_2 saturations to exceed argon saturations due to biological production of N_2, but as a previously established method for gas tension-N_2 derivations we evaluate it anyways.

Assumption 3 utilizes the concurrent N_2:Ar from mass spectrometry and gas tension measurements from the GTD to estimate the argon:

$$pAr = \frac{(GT - pH_2O - pCO_2) * \frac{Sol_{N_2}}{(N_2:Ar)}}{Sol_{Ar} + \frac{Sol_{N_2}}{(N_2:Ar)}} \quad (3.6)$$

The full derivation of Equation 3.6 is shown in Appendix A.

Assumption 4 utilizes an independent argon concentration dataset collected by Fuchsman et al [2017] during a different cruise in 2012 in the ETNP ODZ using the isotope dilution method for absolute [Ar] measurments. However, we need to determine the 2012 argon concentrations which correspond to our measurements. To do this, we develop and apply a linear mixing model based on T-S analysis. Starting with our observations, we fit a series of linear regressions to our T-S observations in the ODZ. The intersections of our T-S regressions coincides with an unique water-mass end-member. Next, the 2012 argon concentrations with the most similar T and S profiles to our observations are fit by linear regression against density to the density of the water-mass end-members we identified in our dataset. This yields argon concentrations for our different water masses. Finally, the argon concentrations in our water-masses are linearly combined with each other to yield a "mixing curve" of argon concentrations for the range of T-S we observed in 2014 in the ODZ.

3.2.3. Biogenic-N2

Ultimately, we are interested in determining the biogenic-N_2 concentration. However, the total dissolved N_2 in the ODZ is a combination of biogenic-N_2 gas and the dissolved-N_2 which originates from physical process (abiotic N_2):

$$[N_2]_{total} = [N_2]_{bio} + [N_2]_{abiotic} \quad (3.7)$$

Thus, successfully determining biogenic-N_2 requires removing the abiotic-N_2 from the total measured N_2.

3.2.3.1. From Gas Tension

Our gas tension method measures the total dissolved N_2 in the ODZ. Consequently, we need a method for determining the abiotic-N_2. Our solution is to assume that the abiotic-N_2 saturation is equal to the argon saturation and that all biogenic-N_2 is locally produced. Since the argon and nitrogen solubility curves are similar over the oceanic ranges of temperature and salinity, the argon saturation should reflect the effects of warming and mixing inducing abiotic-N_2

supersaturations. We determine our argon saturations from the argon concentrations and T-S calculated with our mixing model. With the nitrogen solubility and the argon saturation, we calculate the biogenic-N_2 as:

$$[N_2]_{bio} = [N_2]_{total} - Sol_{N_2}(T,S,P) * Ar_{sat}(\%) \quad (3.8)$$

3.2.3.2. From Nutrients

Derivation of the biogenic-N_2 from DIN observations is ultimately dependent upon the reference values (N_{exp}) against which the measured DIN is compared. Most previous studies have estimated N_{exp} using a stoichiometric relationship based on the Redfield remineralization ratio of DIN to phosphate of organic matter for the given region of the ocean (see Groffman et al. (2006) for discussion on the different remineralization ratios that have been utilized). We chose to utilize the method from Chang et al (2012), which derived an empirical fit of the phosphate vs. DIN relationship from WOCE observations approximately in the source waters of the ODZ:

$$[N_{exp}] = m \times [PO_4^{3-}] + b \quad (3.9)$$

The constants m and b in the above equation vary based on density. From Chang et al (2012), we use the values $m = 14.3, b = -2.2$ and $m = 13.0, b = 1.8$ for the density intervals $\sigma_\theta =$ surface $- 26.4$ and $26.4 - 27.2$, which respectively cover the range of densities we observed.

3.2.3.3. From N_2:Ar

Similar to the nutrients-based approach described in Section 3.2.3.2, calculation of biogenic-N_2 from N_2:Ar observations following Equation 3.2 depends on knowing the N_2:Ar values of the source waters. Since we lack observations outside the ETNP ODZ, we again follow Chang et al (2012), who empirically-fitted an equation to a N_2:Ar vs σ_θ profile they collected outside the ODZ in the ETNP to obtain the relationship:

$$(N_2 : Ar)_{abiotic} = 0.998 + 2.31 \times 10^{-8} e^{0.49\sigma_\theta} \quad (3.10)$$

Note that we use slightly different nomenclature than Chang et al (2012), whom label their $(N_2 : Ar)_{abiotic}$ as $(N_2 : Ar)_{back}$. This approach assumes constant abiotic ratios along isopycnals.

A second approach we take to deriving the biogenic-N_2 from our N_2:Ar_{ODZ} is to use the argon concentrations calculated following argon **Assumption 4**. Using the argon concentrations calculated for our observations with our mixing model, we can calculate the total dissolved N_2

from the $(N_2{:}\,Ar)_{ODZ}$. Then, the biogenic-N_2 is calculated with the same abiotic-N_2 as the gas-tension approach:

$$[N_2]_{bio} = (N_2{:}\,Ar)_{ODZ} \times [Ar] - Sol_{N_2}(T,S,P) \times Ar_{sat}(\%) \qquad (3.11)$$

3.2.4. Field & Sample Locations

Measurement of dissolved N_2 concentrations in the ETNP ODZ occurred in May - June 2014 as part of the *NH1410* research cruise investigating nitrogen-cycle processes aboard the *R/V New Horizon*. Measurements were made using two UW/APL Gas-Profiling Floats (F77 & F78), variants of the Lagrangian float [D'Asaro 2004] with the ability to accurately target and follow isopycnals. Each float was equipped with a GTD, a SBE43 oxygen sensor, an Aanderaa oxygen optode, a package of T, S, and P sensors, and other sensors not discussed here. The floats were deployed approximately two kilometers apart at 20.08°N and 107.07°W. Float 77 was recovered after 1.5 days and redeployed 9 days later near Float 78 for 4 days. Only data from the second deployment of float 77 is used here. Float 78 drifted northwest over the course of the 15-day deployment (Figure 3.2).

During deployment, the floats performed a series of vertical profiles targeting isopycnals at predetermined depths. Each profile consists of an initial dive to maximum density, followed by a series of drifts at decreasing densities in the water column lasting 2 – 3 hours to fully equilibrate the GTD. Niskin bottles for dissolved gas analysis were collected at similar pressures, densities, and locations to the float sampling. N_2:Ar measurements were performed on ship utilizing a Quadrupole Mass Spectrometer. CTD and float oxygen (SBE43 & Anderaa optode) were intercompared and calibrated by Winkler-titrations [Langdon 2010] to form a final oxygen product. After calibration, the mean difference with Winklers was 0.2 µM/kg with a standard deviation of 1.5±0.2 µM/kg .

Argon concentration data was collected on a prior cruise to the ETNP in 2012. Our analysis of the float GTD data following argon assumption 4 uses this data set. Note that the argon data were collected 3° - 4° south of the float locations as an onshore-offshore transect from 18.39°N 104.99°W to 14.00°N 110.00°W (Figure 3.2). We assume these data are representative of the source waters for and upstream from where our measurements are located.

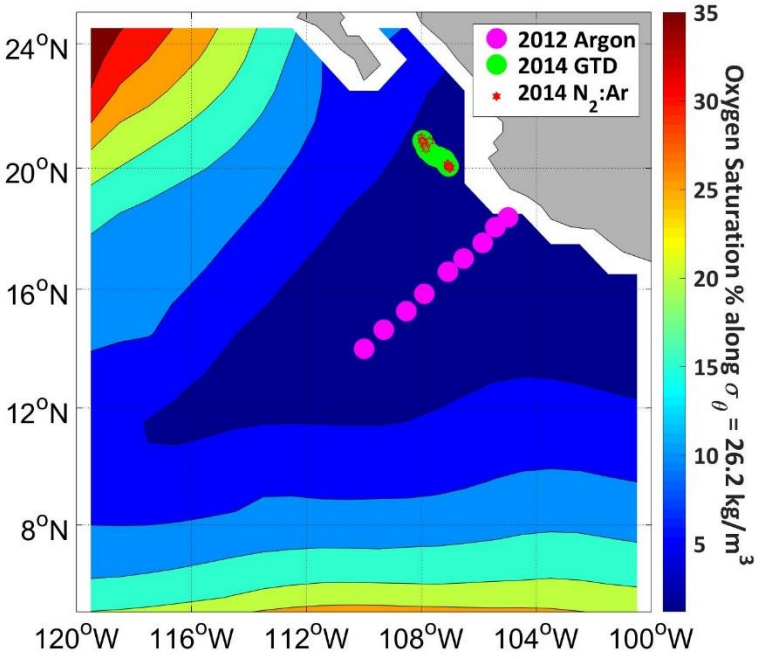

Figure 3.2. Map of the Float GTD gas tension measurements in 2014 (green dots), N2:Ar measurements from discrete Niskin bottles, and the argon measurements made by Fuchsman et al [2017] in 2012. Also plotted is the oxygen saturations along the σθ=26.2 kg/m3 isopycnal.

3.3. RESULTS

3.3.1. Water Properties

Careful analysis of the conservative water properties of potential temperature and salinity is important to develop a model of the physical mixing within the ODZ and parse the physical supersaturation from the biogenic-supersaturation of N_2. We start by presenting the vertical profiles of T, S, and O_2, since this is the way ODZs have been analyzed in the past (Figure 3.3). We then utilize the T – S relationships to develop the mixing model and compute the argon saturations at the densities of our data (Figure 3.4).

The ETNP water column is temperature stratified, with the thermocline at 30 – 70 m depth coinciding with the pycnocline (Figure 3.3). The surface mixed-layer reaches approximately 25 m depth. The oxycline, the region where the O_2 rapidly declines from saturation to below 1 µM/kg, is located at approximately 50 – 70 m. Measurements with a STOX sensor confirms the oxygen within the ODZ core drops below 100 nM [Tiano et al 2014]. Salinity profiles reveal significant

structure, with a salinity minimum (34.48) at 45 m just above the oxycline, and a subpycnocline salinity maximum (34.82) at 130 m.

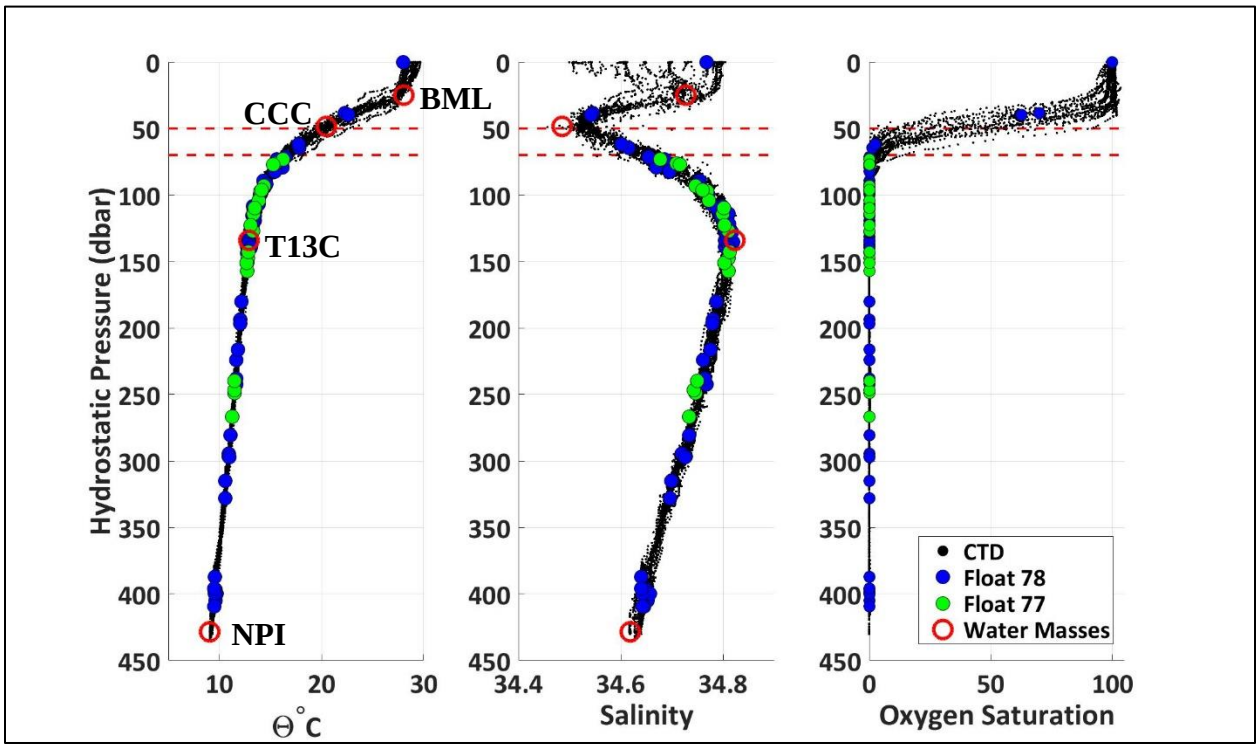

Figure 3.3. Vertical profiles of water properties in the ETNP ODZ collected by the floats, showing potential temperature (left), salinity (middle), and oxygen saturation (right). Three distinct water masses are labelled: North Pacific Intermediate Water (NPIW), 13°C Thermostad water (T13C), California Coastal Current (CCC). The final label is the bottom of the mixed layer (BML). The float 77/78 measurements are those associated with the equilibrated gas tension measurements.

Temperature-salinity analysis shows three unique water masses (Figure 3.4). One of the water masses (T13°C) is the salinity maximum with a potential temperature of 13°C with a potential density of 1026.28 kg/m^3. The salinity maximum is modified 13°C thermostad waters originating in the western tropical Pacific and transported north from the equator in the Northern Subsurface Countercurrent [Fiedler & Talley 2006; Stramma et al 2010].

The 13°C water mixes linearly with the fresher and colder North Pacific Intermediate Water (NPIW) below it and a warmer and fresher water mass, which is likely California Coastal Current (CCC) water. NPIW forms in the northwestern Pacific and Sea of Okhotsk [Fiedler &

Talley 2006]. The CCC originates in the subarctic north pacific, transporting low-salinity waters in the upper-thermocline equatorward [Castro et al 2001]. The bottom of the surface mixed layer is denoted as WM1.

Argon saturations, calculated using assumption 4 (discussed below), range from near equilibrium at the surface and NPIW to nearly 106% at the oxycline/thermocline around 75 dbar (Figure 3.4). The CCC and T13C water masses sampled by our floats during 2014 are slightly warmer than the equivalent T-S for the argon concentrations measured in 2012. Before applying the linear mixing model, we incorporate this warming and its effect on saturations on the water mass end-members. The argon saturations for the float measurements are interpolated from the mixing lines.

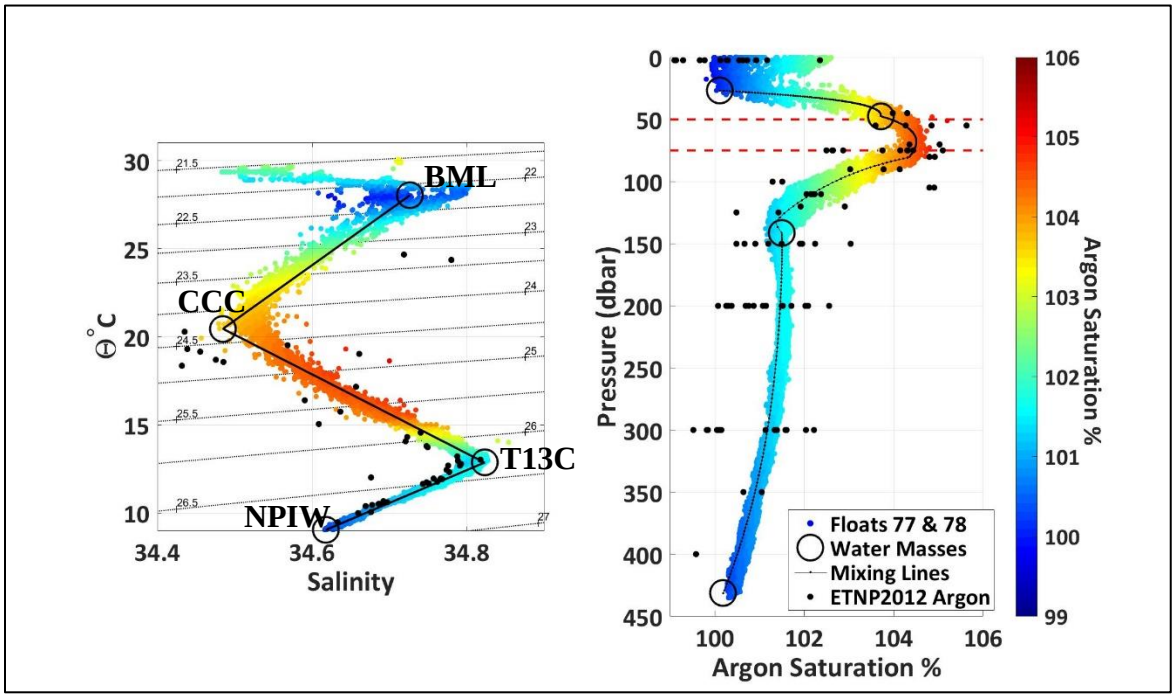

Figure 3.4. Water mass analysis and dissolved argon saturations showing (left) T-S analysis with linear mixing lining between the four end-members and the equivalent vertical profile (right). The ETNP 2012 Argon is the measured argon concentrations in the ODZ from 2012 [Fuchsman et al 2017]. Float observations are the T-S-P from their onboard CTDs and the argon saturation interpolated from the mixing lines.

3.3.2. Argon Sensitivity Analysis

Following Equations 3.3 and 3.8, the biogenic-N_2 calculated from gas tension is affected by the dissolved argon and associated argon saturations. We tested the sensitivity of the gas tension method to each of the argon assumptions listed in Section 2.2, along with calculating the mixing lines based on our T-S analysis. Results are shown in Figure 3.5. Argon saturations varied by 4 – 8% between assumptions. In comparison, the N_2 saturations vary by only 0.015% (Float 78) and 0.012% (Float 77). Thus, significant variation of the argon saturation calculated following Assumption 1 – 4 results in comparatively little variation in calculated N_2 saturation.

Biogenic-N_2 is significantly affected by the estimated abiotic-N_2 saturation, which we define as equal to the argon saturation. The biogenic-N_2 may be qualitatively inferred as the difference between the calculated N_2 saturations and the mixing lines (Figure 3.5). Assumption 1, which *a priori* defines 100% saturation at all measurements, is relatively unaffected by mixing. Assumptions 2 and 3 both calculate either zero or negative biogenic-N_2. Assumption 4, which relies on the independent argon profiles, produces the most realistic values, with positive but varying biogenic-N_2.

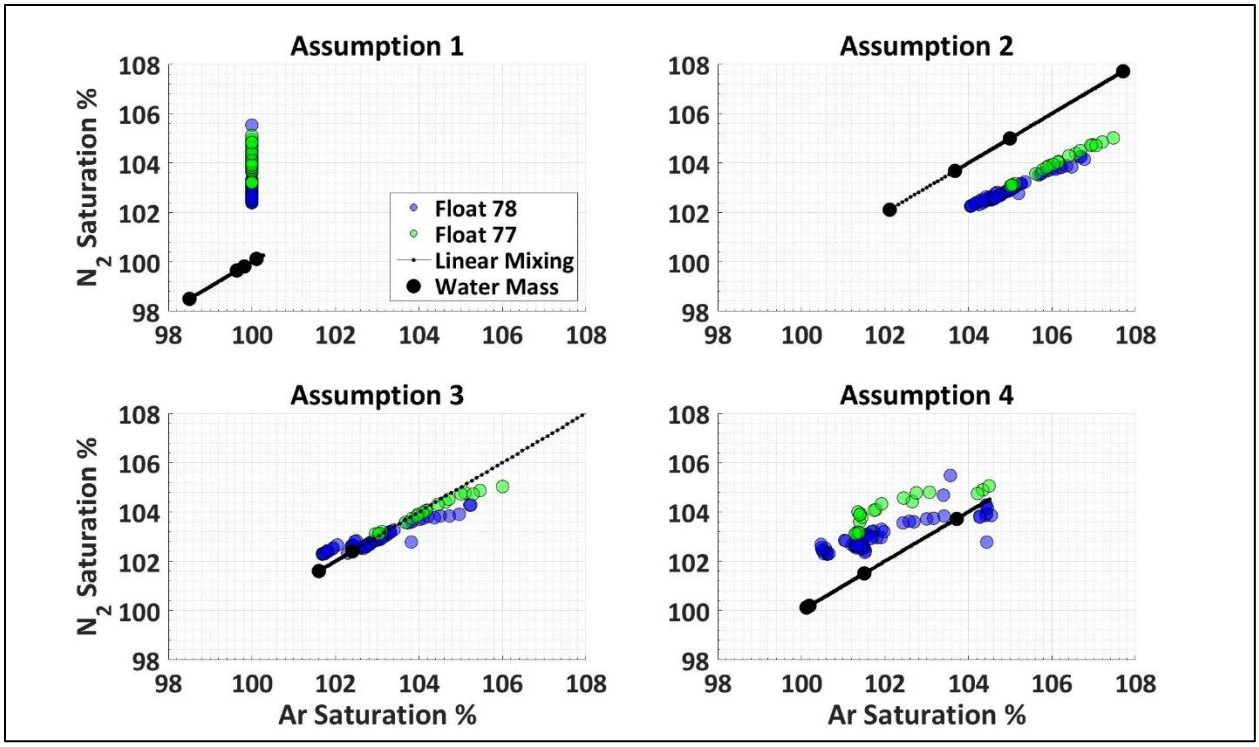

Figure 3.5. Comparison of the argon saturations and calculated N_2 saturations for the four different argon assumptions outlined in Section 2.2. The mixing lines represent the abiotic-N_2. Nitrogen saturations above the mixing lines indicate biogenic-N_2.

We thus chose to use Assumption 4 for biogenic-N_2 calculations. The abiotic-N_2 saturations calculated from linear mixing peak within the oxycline/thermocline region of the water column (Figure 3.6). It is also here that the expected abiotic-N_2 is approximately equal to the observed N_2 saturation. Deeper, in the remainder of the ODZ, the abiotic-N_2 saturation is smaller than the observed N_2 saturation.

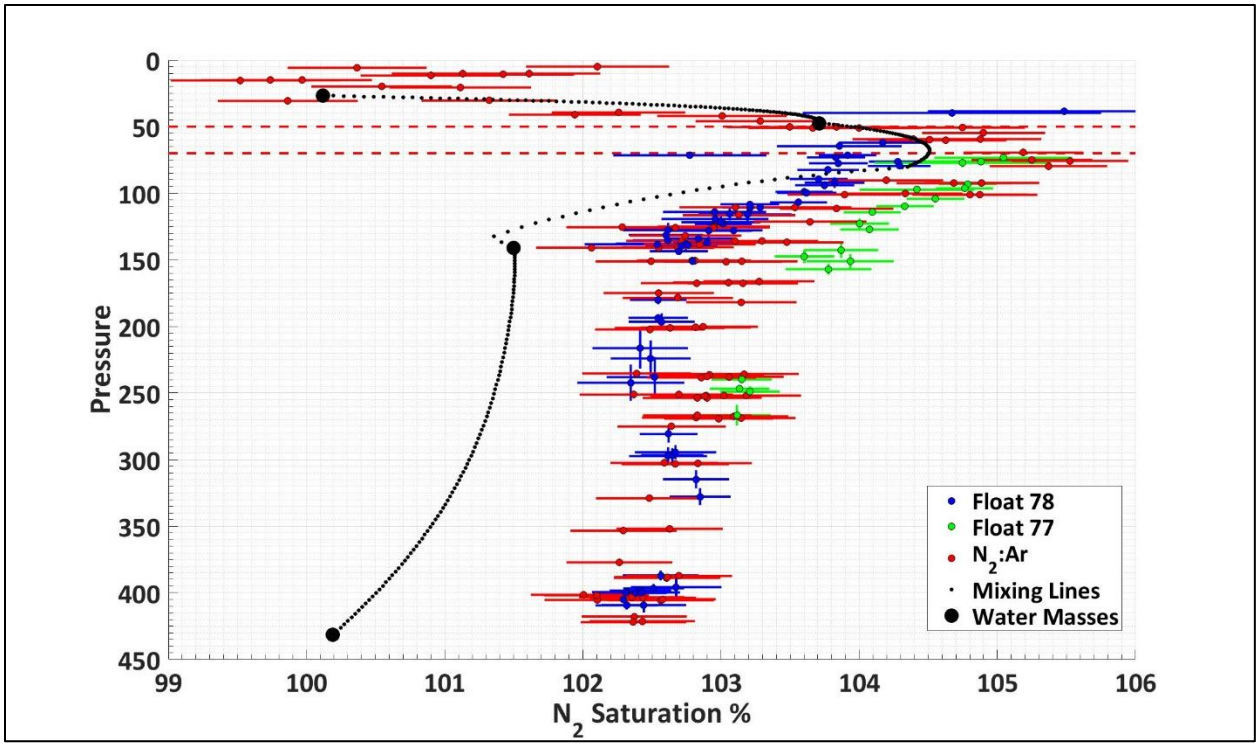

Figure 3.6. Vertical profile of the N_2 saturations calculated from the Float GTDs (green & blue) and the N_2:Ar_{ODZ}, along with the linear mixing lines between water mass end-members using Assumption #4. Biogenic-N_2 is the difference between the calculated N_2 and the mixing lines, which represent the abiotic-N_2. Red dashed lines indicate location of the top and bottom of the oxycline.

3.3.3. Biogenic-N_2

The biogenic-N_2 concentrations at the peak located at ≈130 meters depth are 11.33 ± 1.75 µM/kg (F77), 6.40 ± 2.07 µM/kg (F78), 6.55 ± 2.05 µM/kg (N_2:Ar), and 5.26 ± 1.22 µM/kg (Nutrients). This depth coincides with the 13°C Thermostad water mass along the σ_θ = 26.2 kg/m^3 isopycnal. The largest biogenic-N_2 values measured are 12.57 ± 1.72 µM/kg (F77; σ_θ = 26.2), 11.17 ± 2.17 µM/kg (F78; σ_θ = 26.6), 10.03 ± 2.40 µM/kg (N_2:Ar; σ_θ = 26.6), and 10.08 ± 1.22 µM/kg (Nutrients; σ_θ = 26.6). The N_2:Ar biogenic-N_2 is not significantly different from zero at the surface. The float-GTDs did not fully equilibrate at the surface, so the GTD data is excluded at the surface. Positive biogenic-N_2 is calculated throughout the ODZ.

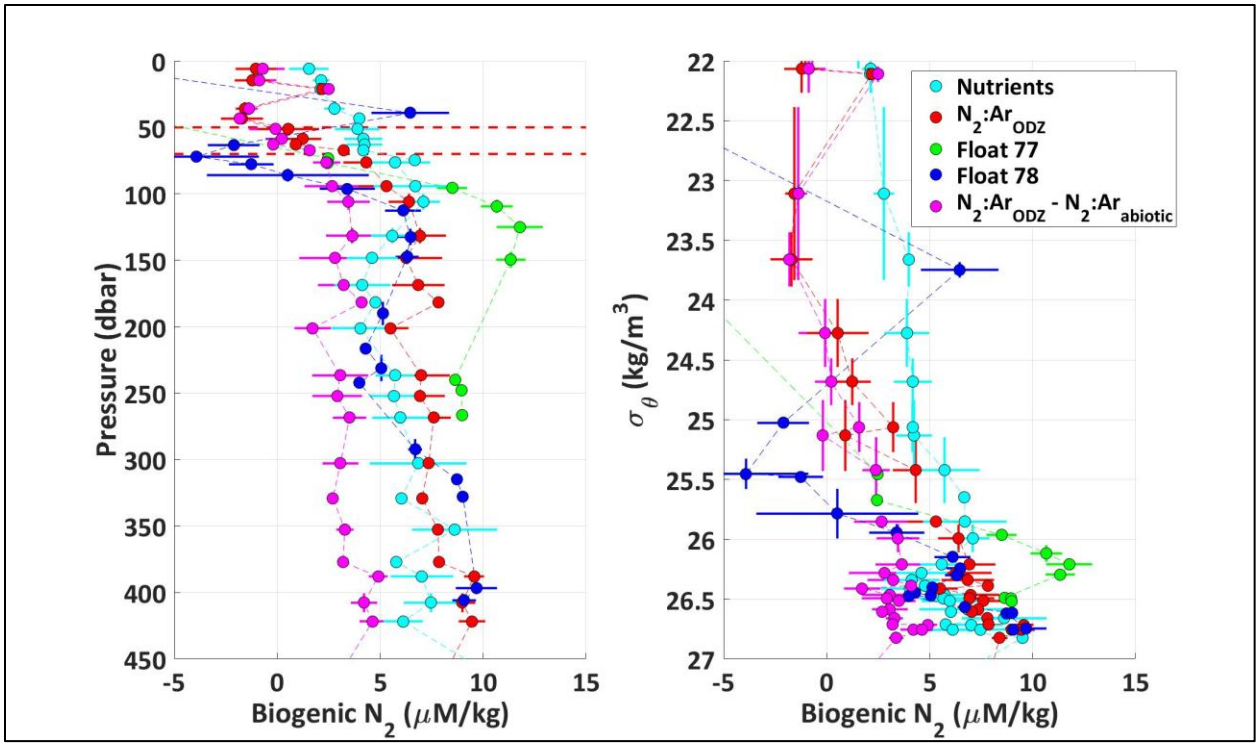

Figure 3.7. Depth binned biogenic N_2 for the ETNP ODZ in 2014 calculated using four different methods: (1) DIN (cyan), using 2014 shipboard data and Equations 3.1 & 3.9; (2) Float 77/78 (green/blue), using gas tension measured on the float and Assumption #4 with Equation 3.11; (3) N_2:Ar_{ODZ} (red), using 2014 shipboard mass spectrometry data N_2:Ar_{ODZ} and Equation 3.11, and (4) N_2:Ar_{ODZ} – N_2:$Ar_{abiotic}$ (magenta), using Chang et al's (2012) empirical fit to density N_2:$Ar_{abiotic}$ and our 2014 shipboard measured N_2:Ar_{ODZ}. Red dashed lines indicate the top and bottom of the oxycline.

3.3.4. Sources of Errors

Sources of uncertainty in the calculated N_2 concentrations from Floats 77 and 78 are due to uncertainty in the gas tension measurement, the argon interpolation, and oxygen measurement. Gas tension measurement uncertainties average ±1.29 mbar (0.15%) and ±1.44 mbar (0.17%) for GTD#44 (Float 77) and GTD#43 (Float 78), respectively [Reed et al. – in press]. Uncertainty of the argon concentration interpolation is 0.03 µM/kg, which combined with the solubility uncertainty of 0.13% results in an average *pAr* uncertainty of ±0.03 mbar (0.26%) [Hamme & Emerson 2004]. Oxygen uncertainties are ≈2 µM/kg for the SeaBird 43 and Aanderaa optode measurements with respect to Winkler titrations. However, in the anoxic portion of the water

column, oxygen is below 100 nM [Tiano et al. 2014]. Thus, we consider oxygen to be zero within the ODZ and thus a negligible contribution to overall uncertainty. These combine to yield average uncertainties of ±1.1 µM/kg (0.26%) and ±1.3 µM/kg (0.36%) of the total N_2 concentrations from Float 77 and Float 78.

Uncertainty with respect to the N_2:Ar-derived N_2 concentrations is principally dependent on the uncertainty in the background argon concentrations of 0.03 µM/kg. Propagating the argon uncertainty yields an average uncertainty of ±1.78 µM/kg (0.37%) on the total N_2 concentrations calculated from the N_2:Ar. The uncertainty on the N_2:$Ar_{abiotic}$ values from Chang et al (2012) were not included in our error analysis.

We find that the N_2 calculated from the Float 77 gas tension is, on average, 1 µM/kg larger compared to the N_2:Ar values, whereas the N_2 calculated from Float 78 is not significantly different from the N_2:Ar nitrogen. The elevated Float 77 N_2 reflects a 7 mbar higher gas tension measured by Float 77 relative to Float 78, which is constant with respect to pressure, density, and temperature, with the cause not yet identified [Chapter 2]. The agreement of Float 78 biogenic-N_2 with the N_2:Ar and DIN-derived biogenic-N_2 suggests Float 77 is incorrect.

3.4. DISCUSSION

Biogenic-N_2 calculated from Float 78 gas tension in the ODZ agrees, to within error, with the biogenic-N_2 derived from the measurements of N_2:Ar and from the DIN. This agreement is subject to the caveat that the gas tension and N_2:Ar methods use the same argon concentrations. The traditional and simplest approach has been to assume 100% argon saturations [Groffman et al 2006]. This assumption does not significantly affect the N_2 concentrations derived from the gas tension, since typical variations of argon saturation (±5%) are less than 0.1% of the total gas tension signal [Ito et al. 2011; Reed et al. – in press]. However, assuming 100% saturation with the N_2:Ar measurements underestimates N_2 by up to 4% compared with the argon concentrations we use. This 4% difference is equivalent to ≈19 µM/kg, a concentration difference larger than the size of our biogenic-N_2 signal.

Gas tension measurements are susceptible to apparent supersaturations due to water mass mixing and warming because of the non-linearity of the N_2, oxygen, and argon gas solubilities [Hamme & Emerson 2004]. The agreement between our gas tension and N_2:Ar biogenic-N_2 with

the DIN-derived biogenic-N_2 supports our approach to calculating argon and choice of abiotic-N_2, since the DIN-approach is an independent estimate with different assumptions. Our T-S mixing approach offers a technique for a physically-consistent method for estimating the argon profile from the sparse ocean argon datasets and a refinement for estimating the abiotic-N_2 profile in the ODZ, rather than straight interpolation on density.

Note that, however, absolute accuracy is improved in determining biogenic-N_2 if the same gas tension sensor is used measure the gas tension both inside the ODZ and in the sources waters. This allows direct comparison of gas tension profiles, such that common errors are removed when differencing.

In their study of the ETNP ODZ, Chang et al. [2012] measured a peak biogenic-N_2 of 6.89 ± 0.89 (σ_θ=26.5, 20.5°N, 106.5°W) and 5.4 ± 0.95 µM/kg (σ_θ=26.5, 21.5°N, 109.5°W). In comparison, our peak biogenic-N_2 values are 12.57 ± 1.72 (F77, σ_θ=26.2), 11.17 ± 1.49 (F78, σ_θ=26.6), 10.03 ± 1.79 µM/kg (N_2:Ar, σ_θ=26.6), and 10.08 ± 1.22 (Nutrients, σ_θ=26.6). This difference of a factor of ≈2 is not a calculation error. The difference is due to different methods of removing the abiotic-N_2. Our new method uses Equation 3.10 and Assumption #4, which implicitly assumes N_2:$Ar_{abiotic}$ = 1. Chang et al [2012] method uses Equations 3.2 and 3.10 plus their measured N_2:$Ar_{abiotic}$. If we apply Chang et al's [2012] measured N_2:$Ar_{abiotic}$, rather than assuming N_2:$Ar_{abiotic}$ = 1, we compute a peak biogenic-N_2 concentration of 5.35 ± 1.47 µM/kg (N_2:Ar, σ_θ=26.6) and 6.35 ± 1.48 µM/kg (F78, σ_θ=26.6) that agrees with their estimate. This supports the conclusion that differences are due to assumptions about the abiotic-N_2. Interestingly, Chang et al. [2012] cite differing abiotic-N_2:Ar values as the reason for why their 2012 results disagree with a previous study in the ETNP ODZ by Devol et al [2006]. Thus, different observed biogenic-N_2 between studies may be the result of choice of abiotic-N_2 proxy, and not differing absolute measurements. However, Chang et al [2012] also found that their N_2:Ar-derived biogenic-N_2 agreed with their nutrient-derived biogenic-N_2. This would support the conclusion that the difference between our results reflect real environmental variability, due to either geographic, seasonal differences.

3.5. SUMMARY

We have demonstrated a new method for accurately determining the biogenic-N_2 concentrations in the ODZ using in-situ gas tension measurements made by a GTD. This approach offers several unique advantages. First, it is comparatively insensitive to the assumption of the argon saturation. Second, it uses in-situ measurements. Third, it offers the ability for long-term autonomous monitoring. We also describe a geophysically-consistent method based on T-S analysis for interpolating sparse oceanic argon data collections to obtain the argon concentrations associated with our measurements. Applying this analysis offers a fourth advantage since it improved estimates of N_2 from N_2:Ar measurements and of biogenic- N_2 by constraining the abiotic-N_2 signal. However, consideration must be made when estimating the abiotic-N_2 contribution, as the selected method can affect the final biogenic-N_2 estimate by nearly a factor of two. Further collection of both argon concentrations and N_2:Ar ratios in the source waters of ODZs should refine estimates of biogenic-N_2 and reconcile the differences between different methods of estimating the abiotic-N_2 signal.

Chapter 4. EFFECT OF HYDROSTATIC PRESSURE ON PARTIAL PRESSURES OF N_2, O_2, AND AIR DISSOLVED IN WATER

Andrew Reed[a,b,*], Craig McNeil[b]

[a]School of Oceanography, University of Washington, 1503 NE Boat Street, Box 357940, Seattle, WA 98195, USA

[b]Applied Physics Laboratory, University of Washington, 1013 NE 40th Street, Seattle, WA 98105, USA

4.1. INTRODUCTION

Observations of dissolved nitrogen, oxygen, and argon are important for studying the large-to-small scale biogeochemical and physical processes that characterize the dynamic ocean. At the surface ocean, dissolved gas concentrations are used to study productivity (McNeil et al 2006), wind and bubble effects on air-sea gas exchange (McNeil & D'Asaro 2007), and sea-ice formation and melting (Hamme & Emerson 2002). Once transported away from the surface, subsequent changes in concentrations provide insight into water mass formation (Nicholson et al 2010), the nitrogen cycle (Chang et al 2012; Hamme & Emerson 2013), and the age of the water since it was last in communication with the atmosphere (Mecking et al 2006).

Accurate and precise measurements of dissolved N_2, O_2, and Ar are important for studying these processes. Aanderaa luminescence-quenching optode and SeaBird 43 amperometric sensors can sample oxygen in-situ to within 2% of saturation. Nitrogen may be determined in-situ to an

accuracy of ±0.4% utilizing the gas tension method (Reed et al – in prep). In oceanographic literature, dissolved gases are typically reported in concentrations of moles of gas per kilogram seawater, i.e. the number of moles of solute dissolved per unit mass of solvent. However, both the SeaBird 43 and Anderaa optode functionally measure the partial pressure of oxygen (Demas et al. 1999; Carlson 2002). Similarly, the gas tension method to sample dissolved N_2 measures the sum of the partial pressures of all the dissolved gases (gas tension) in water (McNeil et al 1995). Henry's Law relates the measured partial pressure of a dissolved gas *i* to its concentration as:

$$P_i = \frac{[C_i]}{S_i(T,S)} \tag{4.1}$$

where P_i is the partial pressure, C_i is the concentration of the gas in solution, and S_i is the solubility of the gas at the sampled temperature T and salinity S. The solubility of nitrogen and oxygen are exceptionally well characterized, with accuracy of 0.13% (Garcia and Gordon 1992; Hamme & Emerson 2004).

The solubilities of N_2 and O_2 were determined at one-wet atmosphere of pressure. However, Klotz (1961) noted that it is important to consider the equilibration of dissolved gasses between the parcel of water at depth and at the surface, and not a bubble at the same depth, as implied by an unmodified Henry's Law relationship. Enns (1965) experimentally tested the effect of hydrostatic pressure on the equilibrium partial pressure of dissolved gases, observing an increase of 13% for He, 16% for CO_2, and 14% of N_2, O_2, and Ar at a hydrostatic pressure of 100 atm in freshwater.

The purpose of our study is to empirically evaluate the change of in-situ gas fugacities of N_2 and O_2 as a function of hydrostatic pressure. Independently, each gas is dissolved in both freshwater and artificial seawater and cycled through a series of hydrostatic pressure changes using a pressure-test vessel (ptv) in the laboratory. Time series of gas tension, oxygen, and hydrostatic pressure are collected to calculate the percent change per 1000 dbar and to estimate the molar volume for each tested gas. Additionally, we reprocess a previously collected laboratory time series of gas tension in air-equilibrated freshwater and hydrostatic pressure to compare with our single-gas results.

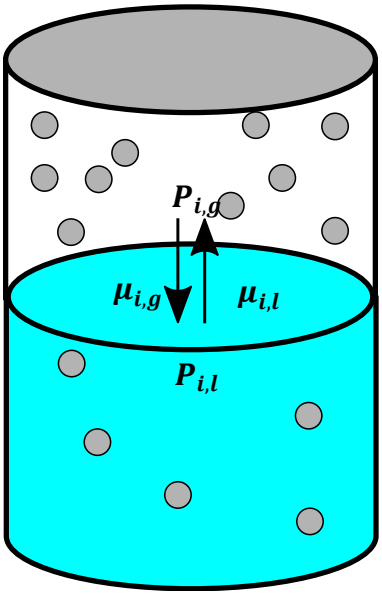

Figure 4.1. Partitioning of a single gas between a dissolved phase (Pi,l) and gas phase (Pi,g) based on the equilibrium between the chemical potentials of the dissolved (μi,l) and gas (μi,g) phases.

4.2. METHODS

4.2.1. Theory

Changes in the partial pressure of a dissolved gas as a function of hydrostatic pressure implies a change in the chemical equilibrium, which describes the partitioning of a gas between its dissolved and vapor phase (Ludwig & MacDonald 2005; Patankar 2016). We examine the underlying thermodynamic mechanism by which we expect these changes to occur and to generate a prediction of how we expect the partial pressures of different gases to change as a function of hydrostatic pressure. We start by considering a single gas (i) in a closed system, which partitions between a vapor phase and a dissolved phase in water (Figure 4.1). At equilibrium, the chemical potential (μ) of the dissolved component (l) is equal to that of the vapor phase (g) (Wilhelm et al 1977):

$$\mu_{i.l} = \mu_{i,g} \tag{4.2}$$

We first treat the chemical potential of the dissolved and gas components separately. Then we combine the results to get a theoretical description of how the fugacity of a gas should change for a closed system as a function of hydrostatic pressure. This provides a framework for analyzing our experimental results.

4.2.1.1. Chemical Potential of the Gas Component

First, we recall that the chemical potential is define as the Gibbs Free Energy of a chemical system (Stumm & Morgan 1996):

$$G = \mu(T, P) \tag{4.3}$$

Next, we follow convention and define the chemical potential of gas i at 1 atmosphere of pressure to be (Ludwig & MacDonald 2005):

$$\mu_{i,g}(T, P = 1\text{atm}) = \mu^0_{i,g}(T) \tag{4.4}$$

And that, for an isothermal closed system, i.e. *T* and *n* are constant, the change in the Gibbs Free Energy is described by (Stumm & Morgan 1996):

$$\left(\frac{\partial G}{\partial P}\right)_{T,n} = V_i \tag{4.5}$$

The constant V_i is the partial molar volume (mL/mol) of the gas. We can replace the Gibbs free energy term with the definition of the chemical potential of the system and assume the gas behaves close to ideally (Wilhelm et al 1977; Ludwig & MacDonald 2005; Patankar 2016):

$$\left(\frac{\partial \mu_i}{\partial P}\right)_{T,n} = V_i = \frac{nRT}{P} \tag{4.6}$$

We can integrate Equation 4.6 with respect to a standard pressure $P^0 = 1$ atm:

$$\mu_{i,g}(P) - \mu_{i,g}(P = 1\text{atm}) = nRT \ln\left(\frac{P}{P^0}\right) \tag{4.7}$$

$$\mu_{i,g}(P) = \mu^0_{i,g} + nRT \ln(P) \tag{4.8}$$

This gives us a description of the chemical potential of the gas phase of *i* as a function of hydrostatic pressure. In practice, we do not deal with an ideal gas. Instead, we can substitute the fugacity f_i of the gas in place of the partial pressure (Wilhelm et al 1977; Ludwig & MacDonald 2005; Patankar 2016):

$$\mu_{i,g}(P) = \mu^0_{i,g} + nRT \ln(f_i) \tag{4.9}$$

4.2.1.2. Chemical Potential of the Dissolved Component

Now, we consider the other half of Equation 4.2, the component of the gas dissolved in water. Similar arguments are followed as those above, except instead of working with an ideal gas,

we are concerned with the dissolved concentration c_i (Wilhelm et al 1977; Ludwig & MacDonald 2005; Patankar 2016):

$$\mu_{i,l}(T,P) = \mu^*_{i,l}(T,P) + RT\ln(c_i) \tag{4.10}$$

We replace the theoretical concentration c_i with the functional activity a_i:

$$\mu_{i,l}(T,P) = \mu^*_{i,l}(T,P) + RT\ln(a_i) \tag{4.11}$$

Differentiation of this equation with respect to pressure yields the partial molar volume V_i:

$$\frac{\partial \mu_{i,l}(T,P)}{\partial P} = V_i \tag{4.12}$$

4.2.1.3. Full Derivation of the Hydrostatic Pressure Effect

Consequently, we can describe the chemical equilibrium between the gas and dissolved phases of i by substituting Equations 4.10 and 4.12 into Equation 4.2:

$$\mu^0_{i,g}(T) + RT\ln(f_i) = \mu^*_{i,l}(T) + RT\ln(a_i) \tag{4.13}$$

The change in this equilibrium as a function of hydrostatic pressure is:

$$\frac{\partial\left(\mu^0_{i,g} + RT\ln(f_i)\right)}{\partial P} = \frac{\partial\left(\mu^*_{i,l} + RT\ln(a_i)\right)}{\partial P} = V_i \tag{4.14}$$

$$\frac{\partial(\ln(f_i))}{\partial P} = \frac{V_i}{RT} \tag{4.15}$$

Subsequent integration yields the change the gas fugacity f_i as a function of the hydrostatic pressure:

$$\frac{\partial(\ln(f_i))}{\partial P} = \frac{V_i}{RT} \tag{4.16}$$

$$\ln(f_i) = \ln(f_i^0) + \frac{V_i \Delta P}{RT} \tag{4.17}$$

$$f_i(P) = f_i^0 e^{\frac{V_i * \Delta P}{RT}} \tag{4.18}$$

Equation 4.18 is known to the physical chemistry community (Ludwig & MacDonald 2005; Patankar 2016).

4.2.1.4. Relation to Henry's Law Solubility

We now revisit Equation 4.1 with our understanding of how hydrostatic pressure affects the in-situ gas fugacity, substituting our $f_i(P)$ for P_i:

$$f_i(P) = \frac{[C_i]}{Sol_i(T,S)} \tag{4.19}$$

However, whenever $P > 1$ atm, we know that the gas fugacity increases by a factor of $e^{\frac{V_i * \Delta P}{RT}}$. Consequently, we have two choices to restore the equality (which is really an expression for the chemical equilibrium). Either the concentration $[C_i]$ increases in proportion with the gas fugacity as a function of pressure, or the solubility $Sol_i(T,S)$ decreases proportionally with hydrostatic pressure. The correct choice is the latter, since concentrations are (in the absence of any sources or sinks) conservative (Ludwig & MacDonald 2005). Thus, we rewrite Equation 4.19 to incorporate this new solubility dependence:

$$f_i(P) = \frac{[C_i]}{Sol_i(T,S,P)} \tag{4.20}$$

Next, we examine if this alteration to the solubility function is physically realistic. The solubility is the reciprocal of the Henry's constant, which is defined as (Ludwig & MacDonald 2005; Patankar 2016):

$$H_i(T,S,P) = \frac{f_i}{a_i} \tag{4.21}$$

Now, we must consider whether $\mu^*_{i,l}(T,P) = \mu^*_{i,l}(T, P = 1atm)$. If this equality is true, we get a Henry's constant of:

$$H_i(T,S,P) = e^{\frac{\mu^*_{i,l}(T) - \mu^0_{i,g}(T)}{RT}} \tag{4.22}$$

This formulation implies that the Henry's constant is not dependent on pressure. The implication of this is that, if f_i increases with pressure but H_i is constant, then the activity must increase as well with pressure (Ludwig & MacDonald 2005). This contradicts the definition of activity as the effective concentration. However, if we let the entire pressure effect be included in the term $\mu^*_{i,l}(T,P)$, we get the following for Henry's constant (Patankar 2016):

$$H_i(T,S,P) = e^{\frac{\mu^*_{i,l}(T,P) - \mu^0_{i,g}(T)}{RT}} \tag{4.23}$$

This can be further simplified to get:

$$H_i(T,S,P) = H_i(T,S,P = 1)e^{\frac{V_i(P-1)}{RT}} \tag{4.24}$$

In the above equation, $H_i(T,S,P = 1)$ is the Henry's constant as normally defined. With this equation, we now have a description of Henry's constant that changes as a function of hydrostatic

pressure by a factor equal to the gas fugacity. This allows us to preserve the conservative property of concentrations/activities while reconciling with the increase in fugacity with increasing hydrostatic pressure.

4.2.2. Experimental Setup

Successfully investigating the hydrostatic pressure effects requires us to solve three key problems: (1) replacement of the dissolved gases in water with a single dissolved gas; (2) ability of isolate the system and change the hydrostatic pressure; (3) measure the partial pressure of the dissolved gas. Our solution to solve these three challenges is shown in Figure 4.2.

Gas exchange is performed in a plastic external water reservoir with dimensions of 30.48 cm width by 30.48 cm length by 45.72 cm height for a total volume of 37.85 liters. A one-way airlock through the lid allows for a slight overpressure of the equilibrating gas with respect to the external atmosphere. Gas exchange with the water is achieved by bubbling using a balsa wood air stone which is connected to the gas source and submerged in the water. A bilge-pump draws from the bottom of the reservoir and pushes the water into the ptv. The water return is located at the top of the of the reservoir and positioned to maximize mixing within the reservoir. Two 1500 psi-rated, ½-inch O.D. two-way valves are used to open or isolate the pressurized components from the external reservoir.

We placed a plastic containment vessel inside of the ptv that seals against the tank bulkhead. This is to separate the gas-equilibrated water within the containment vessel from the water used to pressure the tank, which his fed from the municipal water supply and rapidly reduced by the ptv itself. Pressure is communicated from the ptv through the base of the containment vessel via a rubber bladder. Our instrumentation packages are suspended in the containment vessel from a threaded metal rod connected to the bulkhead. IE-55 connectors allow power and communications through the bulkhead between a computer and power source to the instruments. A Heise PTE-1 pressure gauge is directly connected to the ptv. The ptv pressure is controlled externally by manipulating an analog pressure gauge with pressure amplifier.

In-situ sampling of the dissolved gas fugacity is achieved using a gas tension device (GTD). The GTD works by measuring the barometric pressure of a small sample volume of air separated from the water by a gas-permeable membrane resting on a rigid permeable support. The barometer

used is a Paroscientific Digiquartz Pressure transducer (0-30 psia) barometer with manufacturer's stated accuracy of 0.01% and precision of 0.0001%.

Functionally, the GTD measures the gas tension of water, which is the sum of all the dissolved gas fugacities:

$$GT = fN_2 + fO_2 + fAr + fH_2O + f_{Trace} \quad (4.25)$$

Teflon-AF is differentially permeable to the dissolved gases: water vapor is the most permeable, followed by O_2, Ar, and lastly N_2 (Alentiev et al. 2002; Bernardo et al. 2009). We assume that, for all measurements made with the GTD, water vapor is 100% saturated.

We concurrently measure gas tension using a GTD, oxygen using an Anderaa optode, temperature, and hydrostatic pressure with a Heise PTE-1 pressure gauge. Gas tension and oxygen are sampled once every 30 seconds and hydrostatic pressure once a minute. The GTD is continuously flushed by an SBE 5T pump.

In addition, we reprocess a time series collected in the laboratory during the initial design and testing phase of the GTD instruments (Reed et al 2018 – in press). In the air experiment, we placed two GTDs (S/N 43 & 44) into a larger ptv filled with freshwater at equilibrium with one standard atmosphere. Hydrostatic pressure was changed in increments of ≈100 psi (70 dbar) up to a maximum of 500 psi (340 dbar), with each pressure maintained for a minimum of 24 hours. Temperature, pressure, and gas tension were recorded once per minute. The GTDs were flushed on a 50% cycle.

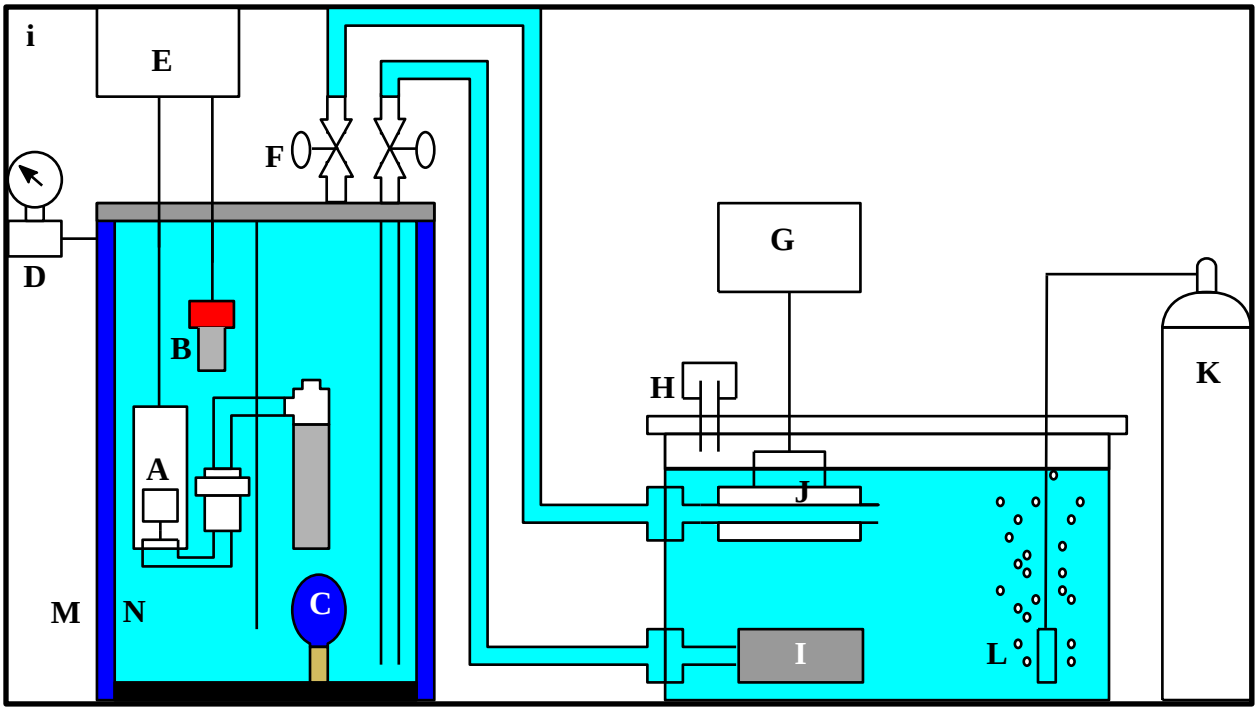

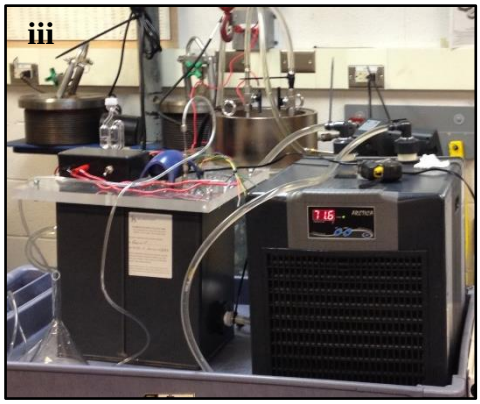

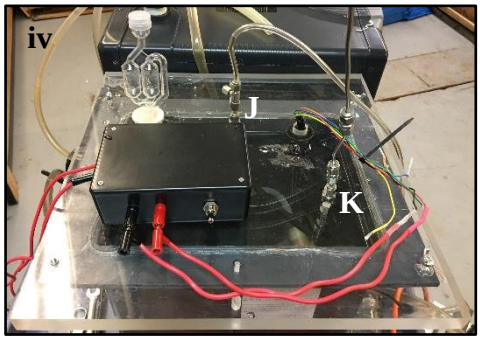

Figure 4.2. (i) Schematic of the Henry's Law hydrostatic pressure setup. A: GTD; B. Aanderaa oxygen optode; C: Pressure bladder; D: Heise pressure gauge; E: Computer; F: Two-way valves; G: Vacuum pump; H: Air-lock; I: Bilge pump; J: Gas exchanger, K: Gas source; L: Balsa-wood bubbler; M: Pressure test vessel; N: Containment vessel. (ii) The GTD and optode suspended within the containment vessel. (iii) The gas exchange vessel connected to the ptv (behind it). The water lines were run through a cooler that we did not use. (iv) Top of the gas exchange vessel showing where the lines for the gas input and vacuum lines penetrated the lid, along with a deck box to isolate the bilge pump power supply.

4.2.3. Experimental Procedure

Gas exchange was achieved by bubbling industrial grade N_2 or O_2 (99.97% pure) in fresh water in the reservoir for a minimum of 8 hours at a gas flow rate of ≈2 psi. Water is circulated between the reservoir and test tank. After gas exchange, the gas flow is shut-off and the system allowed to circulate for 30 minutes to eliminate microbubbles. The two-way-valves are then sealed and the pressure tank is isolated from the external reservoir. Next, the system is pressurized in approximately 100 psi (≈70 dbar) steps from atmospheric pressure up to 800 psi (≈550 dbar), and then repeated with decreasing 100 psi steps back to atmospheric pressure. Finally, we perform a series of changes between atmospheric and 800 psi. After each change of pressure, we let the GTD equilibrate for a minimum of 6 response times (90 minutes total for N_2, 30 minutes total for O_2).

Time series for the N_2 and O_2 are first corrected for changes in temperature and any internal sources or sinks of gas (such as respiration for O_2) using a least-square-minimization fitting procedure described in Reed et al. (2018). Next, the corrected gas tension is adjusted to 25°C, which is the temperature that molar volumes are typically reported. Then, the T=25°C adjusted gas tension at each hydrostatic pressure level is fit to determine the equilibrated gas tension GT_{eq}:

$$GT(t) = GT_{eq} + \Delta GT\left(e^{-\frac{t}{\tau}}\right) \tag{4.26}$$

With the measurements of GT_{eq} at each equilibration following a change in hydrostatic pressure, we linearize Equation 4.26, substituting our fitted $GT_{eq}(P) = f_i(P)$, to get:

$$\ln\left(GT_{eq}(P)\right) = \ln\left(GT_{eq}^{0}\right) + \left(\frac{V_i}{RT}\right)\Delta P \tag{4.27}$$

We thus plot the $\ln\left(GT_{eq}(P)\right)_{T=25°C}$ as a function of the measured hydrostatic pressure. The slope of the line is used to calculate the molar volume of the gas, which can be compared with literature values.

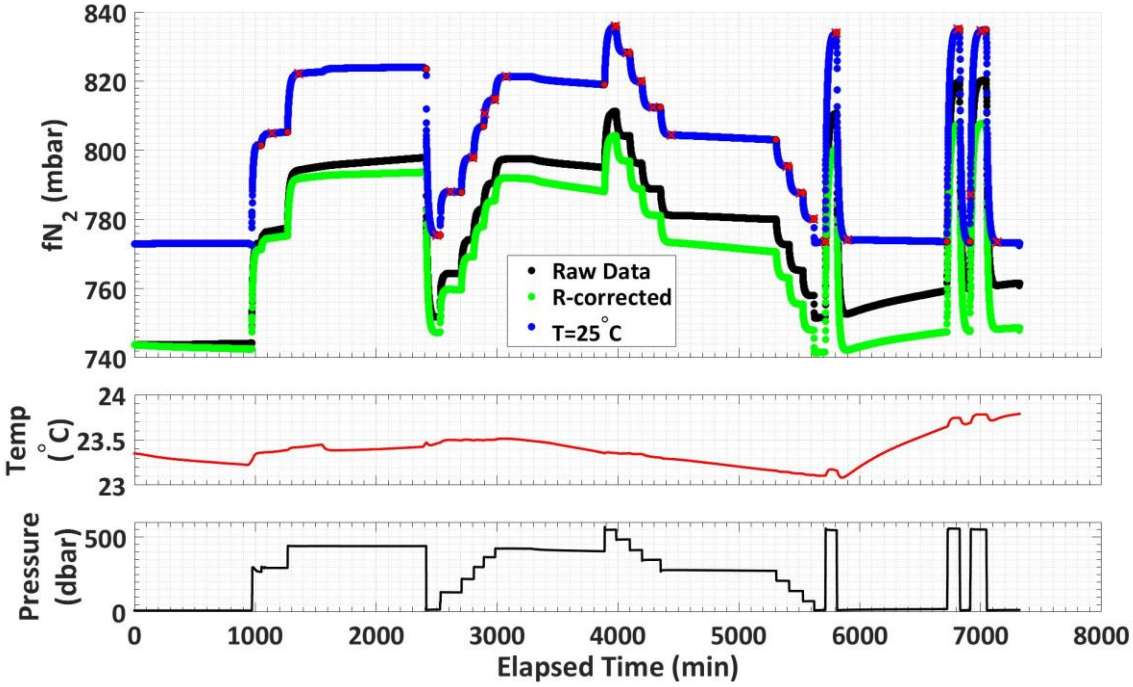

Figure 4.3. (Top) We collected our N_2-data as a single continuous time series within a sealed pressure chamber. The raw data (black) are first corrected for any drift due to loss/gains of N_2 from plastic adsorption/desorption (green), and then adjusted to T=25°C (blue). The red dots and x's mark the start and end of the sections fit with Equation 4.26. (Middle) The water temperature varied by less than 1°C over the course of the experiment with changes driven by warming/cooling of the ambient lab temperature. (Bottom) The hydrostatic pressure time series which we manipulated to change the gas tension.

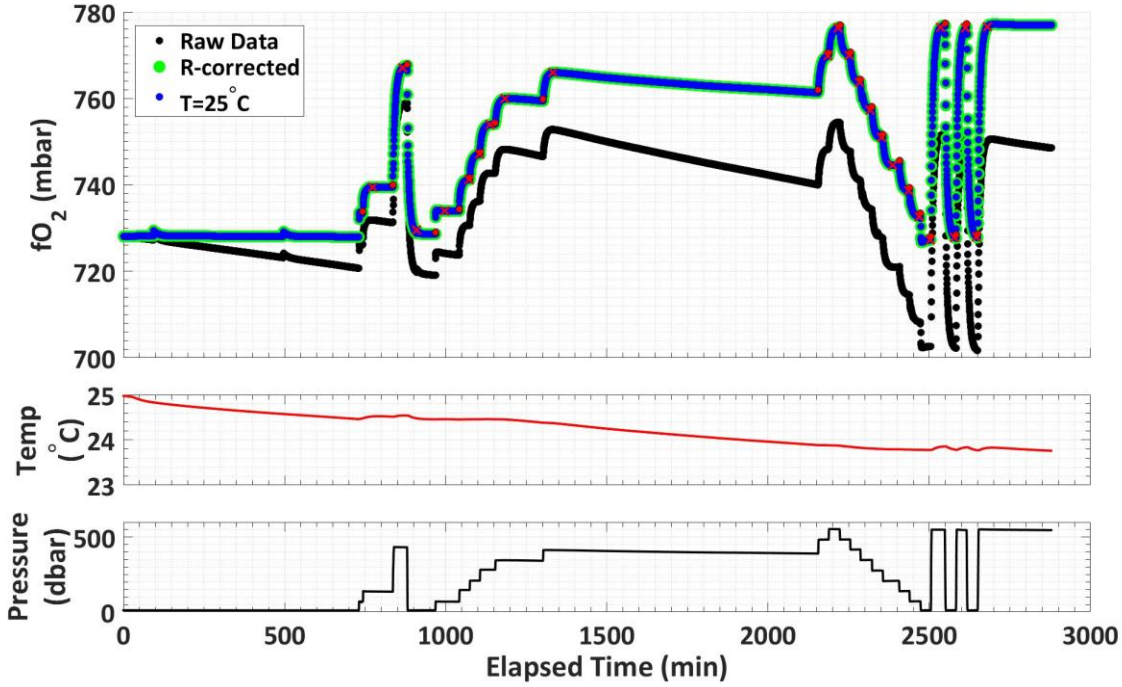

Figure 4.4. (Top) We collected our O_2-data as a single continuous time series within a sealed pressure chamber. The raw data (black) are corrected for any loss/gains of O_2 due to plastic adsorption/desorption and respiration/oxidation (green), and then adjusted to T=25°C (blue). The red dots and x's mark the start and end of the sections fit with Equation 4.26. The corrected-time series is masked by the 25°C normalized time series since the O_2 time series begins close to 25°C. (Middle) The water temperature decreased nearly linearly by 1.2°C over the course of the experiment with changes driven by warming/cooling of the ambient lab temperature. (Bottom) The hydrostatic pressure time series which we manipulated to change the gas tension.

4.3. RESULTS

We collected 22 and 23 equilibrated gas tension measurements for N_2 and O_2, respectively. We calculate partial molar volumes of 35.12 ± 0.27 mL/mol for N_2 and 29.87 ± 0.35 mL/mol for O_2. The molar volumes for N_2 and O_2 are 6.4% higher and 6.7% lower, respectively, than many reported literature values, which are typically 31 ± 2 mL/mol N_2 and 32 ± 2 mL/mol O_2 (Bignell 1984; Kennen & Pollack 1990; Ludwig & MacDonald 2005). However, our N_2 partial molar volume does agree with Moore et al (1982) and Zhou and Battino (2001), who respectively measured a V_{N_2} = 35.7 ± 0.4 mL/mol and 33.1 ± 1.6 mL/mol. With our partial molar volumes, we

calculate a 15.53 ± 0.12% per 100 atm increase of N_2-fugacity and 12.99 ± 0.14% per 100 atm increase of O_2 fugacity, compared with the 14% per 100 atm observed by Enns (1965).

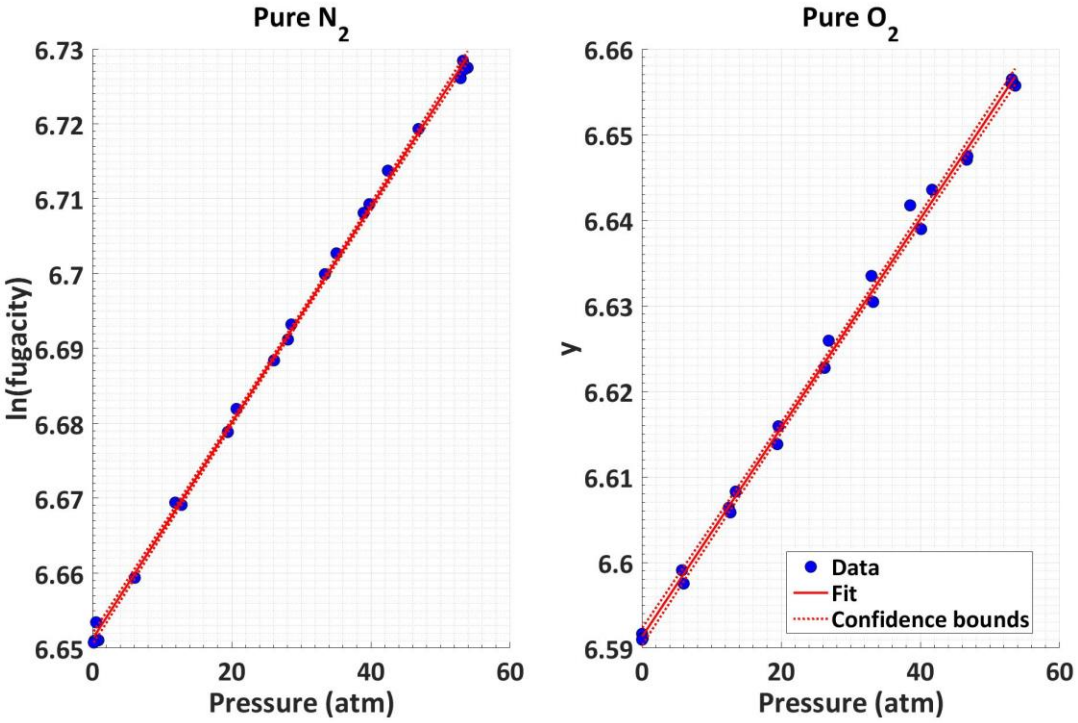

Figure 4.5. Change of N_2 (left) and O_2 (right) fugacities as a function of hydrostatic pressure. Data are fit following Equation 4.27. The partial molar volumes of the gases are calculated from the slope of the fit.

With the reprocessed air data, we had 11 samples from GTD#43 and 11 samples from GTD#44. The two GTDs measured within ±0.2 mbar of each other. We calculate partial molar volumes of 31.74 ± 1.30 mL/mol from GTD#43 and 31.75 ± 1.27 mL/mol from GTD#44. Linear combination of our calculated partial molar volumes for N_2 and O_2, weighted by their respective mole fractions, yields an estimate for air of 33.68 ± 0.47 mL/mol. This is not significantly different than our air values, which gives us further confidence in the comparability of our measurements. Thus, for a standard seawater parcel that equilibrated with the atmosphere and subsequently subducted, we would expect an increase of 13.86% (13.27% – 14.45%) of measured gas tension per 100 atm of hydrostatic pressure. This falls within the 14% per 100 atm we expected based on literature for an atmospheric mixture of gases (N_2 + O_2 + Ar).

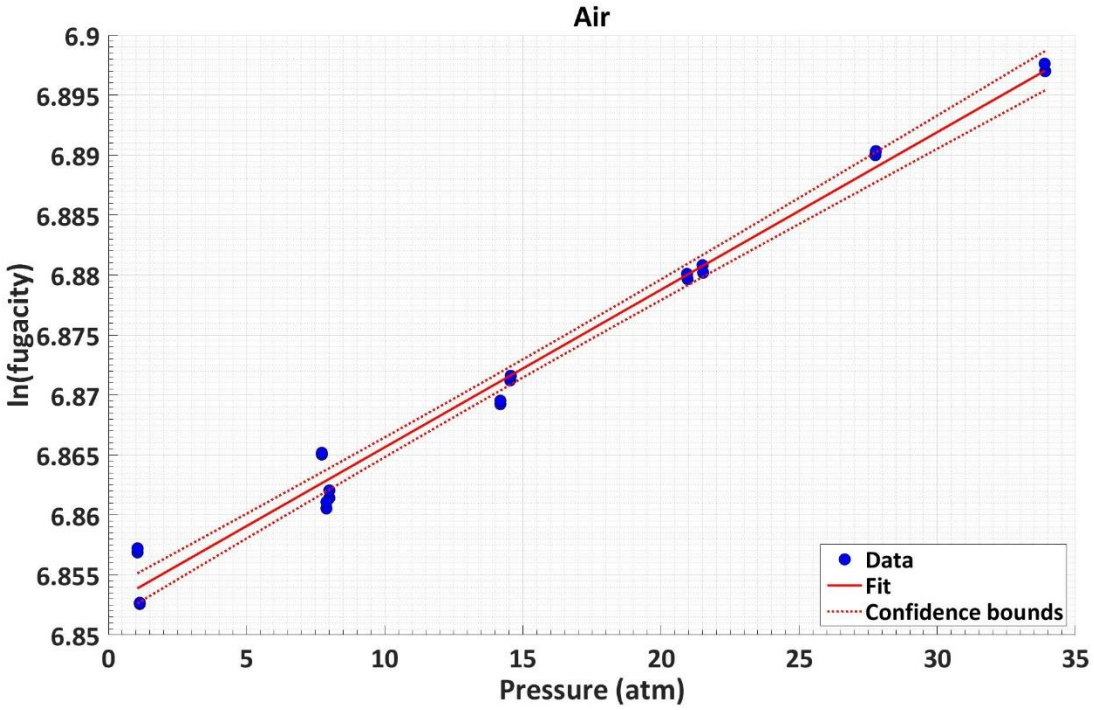

Figure 4.6. The change in the gas tension for an atmospheric mixture of gases (N_2 + O_2 + Ar). Data is fit following Equation 4.27. The partial molar volume of the air mixture is calculated from the slope of the fit.

4.4. DISCUSSION

Our determination of the partial molar volumes and hydrostatic pressure effect is dependent on how well we can measure the in-situ gas tension and control our independent variables. First, the GTD-gas tension approach can measure the in-situ gas tension to within 0.4-0.6% for a variety of conditions and applications (during hurricanes, in anoxic waters, on moored profilers) (D'Asaro & McNeil 2007; Reed et al-in prep; Emerson et al 2002). This gives us confidence in the accuracy of our measurements. Another source of potential error is our correction for temperature. The fitting procedure utilized to model and correct for changes in temperature and concentration can reproduce observed gas tension to within 0.22% (Reed et al 2018). A further potential complication is gas desorption/adsorption from the plastic components of our experimental setup may have contributed to changing gas levels during the experiment, since the derivation of the partial molar volumes and hydrostatic pressure effect are for closed systems. Changes in the calculated dissolved concentrations of corrected-N_2 and O_2 are less than ± 1 umol/kg (< 0.2%) over the time series.

The partial molar volumes of N_2 and O_2 are temperature-dependent (Zhou and Battino 2001). However, previous study on the temperature-effect found that V_{N_2} and V_{O_2} changed less than 1 mL/mol over the temperature range of 0 - 25°C (Bignell 1984). Similarly, the molar volumes of N_2 and O_2 have also been shown to be nearly independent of hydrostatic pressure (Shock et al 1989). Considering our temperatures varied by < 1°C over the course of the experiment, we can conservatively estimate that temperature variability contributed 0.2% uncertainty to our calculated partial molar volumes, and that our linear fit as a function of pressure is valid.

We did not examine the hydrostatic pressure effect or the partial molar volumes of the gases in seawater. To our knowledge, no prior studies focusing on these topics are in the literature. The effect of dissolved salts on gas solubility is often based on the Setschenow equation, which has a temperature dependence (Valderrama 2016). Additionally, the solubility of common dissolved ions in water increases with increasing pressure (Millero 1982). Changes to the salt solubility could be expected to alter the salting-out effect on gas solubility; this implies that the hydrostatic pressure correction would need to be altered to account for the addition of salt to the system. This is an avenue for further exploration by repeating our experiments in seawater.

The first investigations into the hydrostatic pressure effect was to understand how deep-swimming species of fish regulated their swim bladders (Enns 1965). We are concerned with how gas-sensing instrumentation may be affected by increasing hydrostatic pressure. For example, the GTD practically takes a small volume of air with it to depth (ref). We deployed two gas-sensing floats in the Eastern Tropical North Pacific (ETNP) Oxygen Minimum Zone (OMZs) to investigate denitrification, which is the microbial-mediated step-wise reduction of NO3- to N_2 in order to respire organic matter due to the lack of oxygen (Brandes et al 2006). We measured N_2 partial pressures of 857 mbar at 400 dbar pressure. Applying an unmodified Henry's Law, we calculate a total 548 uM/kg of N_2. In comparison, we can apply our results here and derive 516 µM/kg. After removing the background N_2 following Reed et al (in prep), our denitrification estimates are 40 µM/kg vs. 8 µM/kg of N_2. This exercise was to highlight possibly erroneous interpretations when this correction is not applied.

4.5. CONCLUSIONS

Knowing how the fugacities and Henry's solubility of N_2 and O_2 change as a function of hydrostatic pressure is important to understand in-situ conditions experienced by gas-sensing instrumentation, many of which functionally measure the partial pressures of dissolved gases. Our experiments refine estimates of the hydrostatic pressure effect and partial molar volumes of N_2, O_2, and air in equilibrium with freshwater. We also demonstrate how the effect of hydrostatic pressure can alter conclusions drawn from in-situ dissolved-gas sensors. In the future we aim to expand our analysis to incorporate argon and measurements of the hydrostatic pressure effect in seawater.

REFERENCES

1. Alentiev, A.Y., Shantarovich, V.P., Merkel, T.C., Bondar, V.I., Freeman, B.D., Yampolskii, Y.P. 2002. Gas and Vapor Sorption, Permeation, and Diffusion in Glassy Amorphous Teflon AF1600. *Macromolecules, 35: 9513-9522.* doi:10.1021/ma020494f
2. Amante, C., and B. Eakins (2009), Etopo1 1 arc-minute global relief model: Procedures, data sources and analysis, *Tech. Rep. NDSDIS NGDC-24*, NOAA.
3. Aoki, S., S. Rintoul, S. Ushio, S. Watanabe, and N.L.Bindoff (2005), Freshening of the adèlie land bottom water near 140°E, *Geophysical Research Letters*, *32*: *L23601*. doi:10.1029/2005GL024246.
4. Battino, R., T.R. Rettich, T. Tominaga. 1984. The Solubility of Nitrogen and Air in Liquids. *Journal of Physical & Chemical Reference Data 13: 563*. doi:10.1063/1.555713
5. Bernardo, P., Drioli, E., Golemme, G. 2009. Membrane Gas Separation: A Review/State of the Art. *Industrial Engineering Chemical Research 48: 4638-4663.* doi:10.1021/ie8019032
6. Bignell, N. 1984. Partial Molar Volumes of Atmospheric Gases. *Journal of Physical Chemistry 88: 5409-5412*
7. Bindoff, N. L., M. A. Rosenberg, and M. J. Warner (2000), On the circulation and water masses over the antarctic continental slope and rise between 80 and 150°E, *Deep Sea Research II*, *47*: *2299–2326*. doi:10.1016/S0967-0645(00)00038-2.
8. Boyer, T.P., Antonov, J.I., Baranova, O.K., Coleman, C., Garcia, H.E., Grodsky, A., Johnson, D.R., Locarnini, R.A., Mishonov, A.V., O'Brien, T.D., Paver, C.R., Reagan, J.R., Seidov, D., Smolyar, I.V., Zweng, M.M. 2013. World Ocean Database 2013, NOAA Atlas NESDIS 72, S. Levitus, Ed., A. Mishonov, Technical Ed.; Silver Spring, MD, 209 pp., doi:10.7289/V5NZ85MT
9. Bragg, H.M., Johnston, M.W. 2016. Total dissolved gas and water temperature in the lower Columbia River, Oregon and Washington, water year 2015. U.S. Geological Survey Open-File Report 2015-1212, 26p., doi:10.3133/ofr20151212
10. Brandes, J.A., Devol, A.H., Deutsch, C. 2007. New Developments in the Marine Nitrogen Cycle. *Chemical Reviews 107*: 577-589. doi:10.1021/cr050377t
11. Bourbonnais, A., M.A. Altabet, C.N. Charoenpong, J. Larkum, H. Hu, H.W. Bange, and L. Stramma. 2015. N-loss isotope effects in the Peru oxygen minimum zone studied using a

mesoscale eddy as a natural tracer experiment. *Global Biogeochemical Cycles, 29*: *793-811.* doi:10.1002/2014GB005001

12. Bullister, J. L. (2011), Atmospheric cfc-11, cfc-12, cfc-112, ccl4 and sf6 histories. Fine, R. A. (2011), Observations of cfcs and sf_6 as ocean tracers, *Annual Review of Marine Science*, *3*: *173–195*. doi:10.1146/annurev.marine.010908.163933.
13. Carlson, J. 2002. Development of an Optimized Dissolved Oxygen Sensor for Oceanographic Profiling. *International Ocean Systems 6(5)*: *20-21*
14. Castro, C.G., F.P. Chavez, and C.A. Collins. 2001. Role of the California Undercurrent in the export of denitrified waters from the eastern tropical North Pacific. *Global Biogeochemical Cycles 15(4)*: *819-830*
15. Chang, B.X., A.H. Devol, and S.R. Emerson. 2012. Fixed nitrogen loss from the eastern tropical North Pacific and Arabian Sea oxygen deficient zones determined from measurements of N_2:Ar. *Global Biogeochemical Cycles 26(3): GB3030*
16. Charoenpong, C., Bristow, L.A., Altabet, M.A. 2014. A continuous flow isotope ratio mass spectrometry method for high precision determination of dissolved gas ratios and isotopic composition. *Limnology & Oceanography: Methods 12: 323-337.* doi:10.4319/lom.2014.12.323
17. D'Aoust, B.G., White, R., Seibold, H. 1975. Direct measurement of total dissolved gas pressure. *Undersea Biomedical Research 2(2): 141-149*
18. D'Asaro, E., McNeil, C.M. 2007. Air-sea gas exchange at extreme wind speeds measured by autonomous oceanographic floats. *Journal of Marine Systems 66: 92-109.* doi:10.1016/j.jmarsys.2006.06.007
19. Devol, A.H. 2003. Solution to a marine mystery. Nature 422: 575-576
20. Devol, A.H., A.G. Uhlenhopp, S.W.A. Naqvi, J.A. Brandes, D.A. Jayakumar, H. Naik, S. Gaurin, L.A. Codispoti, and T. Yoshinari. 2006. Denitrification rates and excess nitrogen gas concentrations in the Arabian Sea oxygen deficient zone. *Deep Sea Research I 53: 1533-1547.* doi:10.1016/j.dsr.2006.07.005
21. Demas, J.N., DeGraff, B.A., Coleman, P.B. 1999. Oxygen Sensors based on luminescence quenching. *Analytical Chemistry 71: 793A-800A.*
22. Emerson, S., C. Stump, D. Wilbur, and P. Quay. 1999. Accurate measurement of O_2, N_2, and Ar gases in water and the solubility of N_2. *Marine Chemistry 64*: *336-347*

23. Emerson, S., C. Stump, B. Johnson, and D.M. Karl. 2002. In situ determination of oxygen and nitrogen dynamics in the upper ocean. *Deep Sea Research I, 49(5):* 941-952. doi: 10.1016/S0967-0637(02)00004-3
24. Emerson, S., Bushinsky, S. 2016. The role of bubbles during air-sea gas exchange. *Journal of Geophysical Research: Oceans 121:* 4360-4376. doi:10.1002/2016JC011744
25. Enns, T., P.F. Scholander, E.D. Bradstreet. 1964. Effect of Hydrostatic Pressure on Gases Dissolved in Water. *J. Phys. Chem. 69(2),* 389 – 391
26. Fickeisen, D.H., Schneider, M.J., Montgomery, J.C. 1975. A Comparative Evaluation of the Weiss Saturometer. *Trans. American Fisheries Soc. 104(4), 816-820*
27. Fiedler, P., and L.D. Talley. 2006. Hydrography of the eastern tropical Pacific: A review. *Progress in Oceanography 69: 143-180.* doi:10.1016/j.pocean.2006.03.008
28. Fuchsman, C.A., Devol, A.H., Casciotti, K.L., Buchwald, C., Chang, B.X., Horak, R.E.A. 2017. An N isotopic mass balance of the Eastern Tropical North Pacific oxygen deficient zone. *DSR II: Topical Studies in Oceanography*, doi:10.1016/j.dsr2.2017.12.013
29. Fukamachi, Y., M. Wakatsuchi, K. Taira, S. Kitagawa, S. Ushio, A. Takahashi, K. Oikawa, T. Furukawa, H. Yoritaka, and T. Yamanouchi (2000), Seasonal variability of bottom water properties off adèlie land, antarctica, *Journal of Geophysical Research*, *105*(C3), 6531–6540, doi:10.1029/1999JC900292.
30. Garcia, H.E., and L.I. Gordon. 1992. Oxygen solubility in seawater: Better fitting equations. *Limnol. Oceanogr. 37(6),* 1307-1312. doi: 10.4319/lo.1992.37.6.1307
31. Gehrie, E., Archer, D., Emerson, S., Stump, C., Henning, C. 2006. Subsurface ocean argon disequilibrium reveals the equatorial Pacific shadow zone. *Geophysical Research Letters 33: L18608*. doi:10.1029/2006GL026935
32. Gill, A. E. (1973), Circulation and bottom water production in the weddell sea, *Deep Sea Research*, *20*, 111–140, doi:10.1016/0011-7471(73)90048-X.
33. Groffman, P.M., Altabet, M.A., Böhlke, J.K., Butterback-Bahl, K., David, M.B., Firestone, M.K., Giblin, A.E., Kana, T.M., Nielsen, L.P., Voytek, M.A. 2006. Methods for Measuring Denitrification: Diverse Approaches to a Difficult Problem. *Ecol. Appl. 16(6), 2091-2122.* doi: 10.1890/1051-0761(2006)016[2091:MFMDDA]2.0.CO;2
34. Gruber, N., Sarmiento, J.L. 1997. Global patterns of marine nitrogen fixation and denitrification. *Global Biogeochem. Cycles 11(2), 235-266.* doi:10.1029/97GB00077

35. Hales, B., Chipman, D., Takahashi, T. 2004. High-frequency measurement of partial pressure and total concentration of carbon dioxide in seawater using microporous hydrophobic membrane contactors. *Limnol. Oceaongr. Methods 2, 356-364.*
36. Hall, T. M., T. W. N. Haine, M. Holzer, D. A. LaBel, F. Terenzi, and D. W. Waugh (2007), Ventilation rates estimated from tracers in the presence of mixing, *Journal of Physical Oceanography*, *37*, 2599–2611, doi:10.1175/2006JPO3471.1.
37. Hamme, R.C., Emerson, S.R. 2004a. The solubility of neon, nitrogen, and argon in distilled water and seawater. *Deep-Sea Res. I 51, 1517-1528.* doi:10.1016/j.dsr.2004.06.009
38. Hamme, R.C., Emerson, S.R. 2004b. Measurement of dissolved neon by isotope dilution using a quadrupole mas spectrometer. *Mar. Chem. 91, 53-64.* doi:10.1016/j.marchem.2004.05.001
39. Hamme, R.C., Berry, J.E., Klymak, J.M., Denman, K.L. 2015. In situ O_2 and N_2 measurements detect deep-water renewal dynamics in seasonally-anoxic Saanich Inlet. *Cont. Shelf Res. 106, 107-117.* doi:10.1016/j.csr.2015.06.012
40. Hamme, R.C., Severinghaus, J.P. 2007. Trace gas disequilibria during deep-water formation. *Deep-Sea Research I 54(6): 939-950.*
41. Ito, T., Deutsch, C. 2006. Understanding the saturation state of argon in the thermocline: The role of air-sea gas exchange and diapycnal mixing. *Global Biogeochemical Cycles 20: GB3019.* doi:10.1029/2005GB002655
42. Ito, T., Hamme, R.C., Emerson, S. 2011. Temporal and spatial variability of noble gas tracers in the North Pacific. *Journal of Geophysical Research 116*: *C08039.* doi:10.1029/2010JC006828
43. Jacobs, S. (2006), Observations of change in the southern ocean, *Philosophical Transactions of the Royal Society A*, *364*, 1657–1681, doi:10.1098/rsta.2006.1794.
44. Jacobs, S. S., A. F. Amos, and P. M. Bruchhausen (1970), Ross sea oceanography and antarctic bottom water formation, *Deep Sea Research*, *17*, 935–962, doi:10.1016/0011 7471(70)90046-X.
45. Jacobs, S. S., C. F. Giulivi, and P. A. Mele (2002), Freshening of the ross sea during the late 20th-century, *Science*, *297*, 386–389, doi:10.1126/science.1069574.
46. Kennan, R.P., and G.L. Pollack. 1990. Pressure dependence of the solubility of nitrogen, argon, krypton, and xenon in water. *J. Chem. Phys. 93*, 2724

47. Kern, S. (2009), Wintertime antarctic coastal polynya area: 1992-2008, *Geophysical Research Letters*, *36*, L14501, doi:10.1029/2009GL038062.
48. Klots, C.E. 1961. Effect of Hydrostatic Pressure upon the solubility of gases. *Limnology & Oceaongraphy 6(3):* 365-366. doi:10.4319/lo.l1961.6.3.0365
49. Lagarias, J.C., Reeds, J.A., Wright, M.H., Wright, P.E. 1998. Convergence Properties of the Nelder-Mead Simplex Method in Low Dimensions. *SIAM J. of Optimization 9(1):* 112-147. doi:10.1137/S1052623496303470
50. Langdon, C. 2010. Determination of dissolved oxygen in seawater by Winkler titration using the amperometric technique. *The GOSHIP Repeat Hydrography Manual: a Collection of Expert Reports and Guidelines, edited by: Hood, EM, Sabine, CL, and Sloyan, BM*.
51. Löffler, A., Schneider, B., Schmidt, M., Nausch, G. 2011. Estimation of denitrification in Baltic Sea deep water from gas tension measurements. *Marine Chemistry 125:* 91-100. doi:10.1016/j.marchem.2011.02.006
52. Ludwig, H., Macdonald, A.G. 2005. The significance of the activity of dissolved oxygen, and other gases, enhanced by high hydrostatic pressure. *Computational Biochemistry & Physiology Part A 140*: 387-395. doi:10.1016/j.cbpb.2005.02.001
53. Manning, A.H., Solomon, D.K., Sheldon, A.L. 2003. Application of a total dissolved gas pressure probe in ground water studies. *Ground Water 41(4): 440-448*. doi:10.1111/j.1745-6584.2003.tb02378.x
54. McNeil, C.L., Johnson, B.D., Farmer, D.M. 1995. *In-situ* measurement of dissolved nitrogen and oxygen in the ocean. Deep-Sea Res. I 42(5): 819-826. doi:10.1016/0967-0637(95)97829-W
55. McNeil, C., Katz, D., Wanninkhof, R., Johnson, B. 2005. Continuous shipboard sampling of gas tension, oxygen, and nitrogen. *Deep-Sea Research I 52: 1767-1785.* doi:10.1016/j.dsr.2005.04.003
56. McNeil, C., D'Asaro, E., Johnson, B., Horn, M. 2006a. A Gas Tension Device with Response Times of Minutes. *Journal of Atmospheric & Oceanic Technology 23*: *1539-1558.* doi:10.1175/JTECH1974.1
57. McNeil, C.L., D.R. Katz, B. Ward, W.R. McGillis, and B.D. Johnson. 2006b. A method to estimate net community metabolism from profiles of dissolved O_2 and N_2. *Hydrobiologia 571:181-190.* doi:10.1007/s10750-006-0236-7

58. McNeil, C.L., and E.A. D'Asaro. 2007. Parameterization of air-sea gas fluxes at extreme wind speeds. *Journal of Marine Systems, 66: 110-121.* doi:10.1016/j.jmarsys.2006.05.013
59. McNeil, C.L, D'Asaro, E.A. 2014. A calibration equation for oxygen optodes based on physical properties of the sensing foil. *Limnology & Oceanography: Methods, 12: 139-154.* doi:10.4319/lom.2014.12.139
60. Mecking, S., M.J. Warner, and J.L. Bullister. 2006. Temporal changes in pCFC-12 ages and AOU along two hydrographic sections in the eastern subtropical North Pacific. *Deep Sea Research I 53(1): 169-187*
61. Millero, F. 1982. The effect of pressure on the solubility of minerals in water and seawater. *Geochimica et Cosmochimica Acta 46: 11-22.* doi: 0016-7037/82/010011-12
62. Moore, J.C., R. Battino, T.R. Rettich, Y.P. Handa, and E. Wilhelm. 1982. Partial Molar Volumes of "Gases" at Infinite Dilution in Water at 298.15K. *Journal of Chemical Engineering Data 27: 22-24*
63. Morris, M. Y., M. M. Hall, L. C. S. Laurent, and N. G. Hogg (2001), Abyssal mixing in the brazil basin, *Journal of Physical Oceanography, 31: 3331–3348.* doi:10.1175/15200485(2001)031¡3331:AMITBB¿2.0.CO;2.
64. Nicholson, D., S. Emerson, N. Caillon, J. Jouzel, and R.C. Hamme. 2010. Constraining ventilation during deepwater formation using deep ocean measurements of the dissolved gas ratios 40Ar/36Ar, N2/Ar, and Kr/Ar. *Journal of Geophysical Research: Oceans, 115(11).* doi:10.1029/2010JC006152
65. Orsi, A., G. Johnson, and J. Bullister (1999), Circulation, mixing, and production of antarctic bottom water, *Progress in Oceanography 43*: 55–109.
66. Orsi, A. H., W. M. Smethie Jr., and J. L. Bullister (2002), On the total input of Antarctic waters to the deep ocean: A preliminary estimate from chlorofluorocarbon measurements, *Journal of Geophysical Research, 107*: *C83122*. doi:10.1029/2001JC000976.
67. Paulmier, A., Ruiz-Pino, D. 2008. Oxygen minimum zone (OMZs) in the modern ocean. *Progress in Oceanography 80: 113-128.* doi:10.1016/j.pocean.2008.08.001
68. Patankar, N.A. 2016. Thermodynamics of Trapping Gases for Underwater Superhydrophobicity. *Langmuir 32: 7023 – 7028*
69. Pinnau, I., Toy, L.G. 1996. Gas and vapor transport properties of amorphous perfluorinated copolymer membranes based on 2,2-bistrifluoromethlyl-4,5-difluoro-1,3-

diioxole/tetrafluoroethylene. *Journal of Membrane Science 109: 125-133.* doi:10.1016/0376-7388(95)00193-X

70. Purkey, S. G., and G. C. Johnson (2010), Warming of global abyssal and deep southern ocean waters between the 1990s and 2000s: Contributions to global heat and sea level rise budgets, *Journal of Climate, 23*: *6336–6351*. doi:10.1175/2010JCLI3682.1.
71. Purkey, S. G., and G. C. Johnson (2012), Global contraction of antarctic bottom water between the 1980s and 2000s, *Journal of Climate, 25: 5830–5844*. doi:10.1175/JCLI-D11-00612.1.
72. Rivaro, P., S. Massolo, A. Bergamasco, P. Castagno, and G. Budillon (2010), Chemical evidence of the changes of the antarctic bottom water ventilation in the western ross sea between 1997 and 2003, *Deep Sea Research I, 57*: *639–652*. doi:10.1016/j.dsr.2010.03.005.
73. Roemmich, D. (1983), Optimal estimation of hydrographic station data and derived fields, *Journal of Physical Oceanography, 13*: *1544–1549.*
74. Shimada, K., S. Aoki, K. I. Ohshima, and S. R. Rintoul (2012), Influence of ross sea bottom water changes on the warming and freshening of the antarctic bottom water in the australian-antarctic basin, *Ocean Science, 8*: *419–432*. doi:10.5194/os-8-419-2012.
75. Shock, E.L., H.C. Helgeson, D.A. Sverjensky. 1989. Calculation of the thermodynamic and transport properties of aqueous species at high pressures and temperatures: Standard partial molal properties of inorganic neutral species. *Geochimica et Cosmochimica Acta 53: 2157-2183*
76. Smethie Jr., W. M., and R. A. Fine (2001), Rates of north atlantic deep water formation calculated from chlorofluorocarbon inventories, *Deep-Sea Research I, 48*: *189–215*. doi: 10.1016/S0967-0637(00)00048-0.
77. Stramma, L., Johnson, G.C., Firing, E., Schmidtko, S. 2010. Eastern Pacific oxygen minimum zones: Supply paths and multidecadal changes. *Journal of Geophysical Research 115: C09011*. doi:10.1029/2009JC005976
78. Stumm, M., and J.J. Morgan. *Aquatic Chemistry: Chemical Equilibria and Rates in Natural Waters (3rd Ed).* John Wiley & Sons, Inc. 1996
79. Swift, J. H., and A. H. Orsi (2012), 64 days of hydrography and storms: Rvib *Nathaniel B. Palmer's* 2011 s04p cruise, *Oceanography, 25: 54–55*.

80. Takahashi, T., Feely, R.A., Weiss, R.F., Wanninkhof, R.H., Chipman, D.W., Sutherland, S.C., Takahashi, T.T. 1997. Global air-sea flux of CO_2: An estimate based on measurements of sea-air pCO_2 difference. *PNAS, 94(16): 8292-8299.*
81. Tamura, T., K. I. Ohshima, and S. Nihashi (2008), Mapping of sea ice production for antarctic coastal polynyas, *Geophysical Research Letters*, *35*: *L07606*. doi: 10.1029/2009GL038062.
82. Thamdrup, B., Dalsgaard, T., Jensen, M.M., Ulloa, O., Farías, L., Escribano, R. 2006. Anaerobic ammonium oxidation in the oxygen-deficient waters off northern Chile. *Limnology & Oceanography 51(5): 2145-2156.*
83. Tiano, L., Garcia-Robledo, E., Dalsgaard, T., Devol, A.H., Ward, B.B., Ulloa, O., Canfield, D.E., Revsbech, N.P. 2014. Oxygen distribution and aerobic respiration in the north and south eastern tropical Pacific oxygen minimum zones. *Deep-Sea Research I 94: 173-183.* doi:10.1016/j.dsr.2014.10.001
84. Tiepel, E.W., and K.E. Gubbins. 1972. Partial Molal Volumes of Gases Dissolved in Electrolyte Solutions. *Journal of Physical Chemistry 76(21): 3044-3049*
85. Uchida, H., Kawano, T., Kaneko, I., Fukasawa, M. 2008. In Situ Calibration of Optode-Based Oxygen Sensors. *Journal of Atmospheric & Oceanic Technology 25: 2271-2281*. doi:10.1175/2008JTECHO549.1
86. Valderrama, J.O., R.A. Campusano, and L.A. Forero. 2016. A new generalized Henry-Setschenow equation for predicting the solubility of air gases (oxygen, nitrogen and argon) in seawater and saline solutions. *Journal of Molecular Liquids 222: 1218-1227*. doi: 10.1016/j.molliq.2016.07.110
87. Warner, M., and R. Weiss (1985), Solubilities of chlorofluorocarbons 11 and 12 in water and seawater, *Deep Sea Research Part A. Oceanographic Research Papers*, *32*: *1485 –1497*. doi:10.1016/0198-0149(85)90099-8.
88. Warner, M.J., Bullister, J.L., Wisegarver, D.P., ammon, R.H., Weiss, R.F. 1996. Basin-wide distributions of chlorofluorocarbons CFC-11 and CFC-12 in the North Pacific: 1985-1989. *Journal of Geophysical Research 101(C9): 20525-20542*
89. Wilhelm, E., R. Battino, and R.J. Wilcock. 1977. Low-Pressure Solubility of Gases in Liquid Water. *Chemical Reviews 77(2): 219-262*. doi: 10.1021/cr60306a003

90. Whitworth, T. (2002), Two modes of bottom water in the australian-antarctic basin, *Geophysical Research Letters*, *29*: *1073*. doi:10.1029/2001GL014282.
91. Williams, G., N. Bindoff, S. Marsland, and S. Rintoul (2008), Formation and export of dense shelf water from the adèlie depression, east antarctica, *Journal of Geophysical Research*, *113: C04039*. doi:10.1029/2007JC004346.
92. Williams, G., S.Aoki, S. Jacobs, S. Rintoul, T. Tamura, and N. Bindoff (2010), Antarctic bottom water form the adèlie and george v land coast, east antarctica (140-149°E). *Journal of Geophysical Research*, *115*: *C04027*. doi:10.1029/2009JC005812.
93. Williams, G. D., and N. L. Bindoff (2003), Wintertime oceanography of the adèlie depression, *Deep Sea Research II*, *50*: *1373–1392*. doi:10.1016/S0967-0645(03)00074-2.
94. Zhou, T. and R. Battino. 2001. Partial Molar Volumes of 13 Gases in Water at 298.15K and 303.15K. *Journal of Chemical Engineering Data 46*: *331-332*

APPENDIX A

We can calculate an estimate of the dissolved argon concentration by utilizing our concurrent measurements of gas tension and N_2:Ar. First, we start with the definitions of our two different measurements:

$$GT = P_{N_2} + P_{O_2} + P_{Ar} + P_{CO_2} + P_{H_2O} + P_{Trace} \quad \text{(A1)}$$

$$(N_2{:}\,Ar) = \left(\frac{[N_2]}{[Ar]}\right) \quad \text{(A2)}$$

From the equations above, we have two unknowns: the concentrations/partial pressures of N_2 and argon. The water vapor partial pressure is explicitly calculated as a function of T & S and P_{CO_2} = 1.4 mbar following climatology. Additionally, we assume that $P_{O_2} = 0$ and that P_{Trace} is negligible. With these assumptions, we can rearrange both Equation (A1) and (A2) to solve for the unknown N_2 as follows:

$$P_{N_2} = GT - P_{Ar} - P_{H_2O} - P_{CO_2} \quad \text{(A3)}$$

$$P_{N_2} = (N_2{:}\,Ar) * \frac{[Ar]}{Sol_{N_2}(T,S)} \quad \text{(A4)}$$

Now we can set Equations (A3) and (A4) equal to each other and rearrange to yield an expression for the argon concentration:

$$\left(\frac{[N_2]}{[Ar]}\right) * \frac{[Ar]}{Sol_{N_2}(T,S)} = GT - P_{Ar} - P_{H_2O} - P_{CO_2} \quad \text{(A5)}$$

$$[Ar] = \left(GT - P_{Ar} - P_{H_2O} - P_{CO_2}\right) * \frac{Sol_{N_2}(T,S)}{(N_2{:}Ar)} \quad \text{(A6)}$$

Next, we substitute $[Ar] = P_{Ar} * Sol_{Ar}(T,S)$ and solve for P_{Ar}:

$$pAr * Sol_{Ar}(T,S) = (GT - pAr - pH_2O - pCO_2) * \frac{Sol_{N_2}(T,S)}{(N_2{:}Ar)} \quad \text{(A7)}$$

$$pAr * Sol_{Ar}(T,S) + pAr * \frac{Sol_{N_2}(T,S)}{(N_2{:}Ar)} = (GT - pH_2O - pCO_2) * \frac{Sol_{N_2}(T,S)}{(N_2{:}Ar)} \quad \text{(A8)}$$

$$pAr\left(Sol_{Ar} + \frac{Sol_{N_2}(T,S)}{(N_2{:}Ar)}\right) = (GT - pH_2O - pCO_2) * \frac{Sol_{N_2}(T,S)}{(N_2{:}Ar)} \quad \text{(A9)}$$

$$pAr = \frac{(GT - pH_2O - pCO_2) * \frac{Sol_{N_2}(T,S)}{(N_2{:}Ar)}}{Sol_{Ar} + \frac{Sol_{N_2}(T,S)}{(N_2{:}Ar)}} \quad \text{(A10)}$$

VITA

[Andrew Reed is a native of Lancaster, Pennsylvania. He graduated Summa Cum Laude in 2010 from Gettysburg College with his B.S. in Environmental Science. While an undergraduate, he participated in a National Science Foundation Research Experience for Undergraduates at the Texas A&M Marine Science Labs in Galveston, Texas, which inspired him to pursue his graduate studies in Oceanography at the University of Washington.]